TECHNISCHE UNIVERSITÄT WIEN

AUTOMATION & CONTROL INSTITUTE
INSTITUT FÜR AUTOMATISIERUNGS- & REGELUNGSTECHNIK

Modeling and Control of Fluid Velocity in a Confined Vortex

DIPLOMA THESIS

Conducted in partial fulfillment of the requirements for the degree of a

Diplom-Ingenieur (Dipl.-Ing.)

supervised by

Andreas Steinböck
Luca Gasparini

submitted at the

TU Wien
Faculty of Electrical Engineering and Information Technology
Automation and Control Institute

by
Ivan Wuketich
Matriculation number 01429849

Vienna, June 2025

Complex Dynamical Systems Group
A-1040 Wien, Gußhausstr. 27–29, Internet: https://www.acin.tuwien.ac.at

Preamble

I want to first of all thank my supervisor Luca Gasparini and professor Andreas Steinböck for the crucial support and guidance, as well as all ACIN staff members that helped me. Additionally, I need to thank my family and friends for their unwavering support for the duration of this thesis.

Vienna, June 2025

Abstract

Vortices in fluid streams are common and there is still enough research to be done in the area of control of such occurrences. Therefore, a watertight cylindrical setup is manufactured to create a vortex, which is mainly characterized by a tangential velocity component. Many parts are printed with an ordinary 3D printer and the two lids are transparent to observe the vortex.
A gear pump is used for pumping the water into the setup, where a tangential inlet and outlet redirect the flow in the required direction. To measure the velocity of the vortex, a specially developed sensor that is based on a light barrier can detect changes in light intensity at four points along the radius. The frequency of these changes is proportional to the flow rate and thus the rotational speed of the paddles that rotate with the vortex. These measured velocities are calibrated with Computational Fluid Dynamics (CFD) simulations of the same system. Based on these calibrated measurements and the Navier-Stokes equations in cylindrical coordinates, a mathematical model of the vortex is derived and fitted to the measurements with correction factors. Furthermore, a cascade controller is designed for the test rig. The inner loop consists of the pump and an Integral (I) controller. The outer loop is responsible for controlling the strength of the vortex with a Proportional-Integral (PI) controller.
The data shows that the velocity of the vortex is approximately proportional to the flow rate of the pump. Moreover, the resulting velocity profile, which is nonlinear with respect to the radius, demonstrates that this system is not a rigid body vortex. Validation of the fitted model with other flow rates based on the measured tangential velocity confirms the accuracy of the model for the vortex. In addition, the cascade controller allows the vortex to reach a given setpoint.

Kurzzusammenfassung

Wirbel sind weit verbreitet und es besteht noch reichlich Forschungsbedarf hinsichtlich ihrer Regelung. Daher wird ein wasserdichter zylindrischer Aufbau hergestellt, welcher einen Wirbel erzeugt, der hauptsächlich durch eine tangentiale Geschwindigkeitskomponente charakterisiert wird. Die meisten Teile werden mit einem herkömmlichen 3D-Drucker gefertigt und die beiden Deckel sind durchsichtig, um den Wirbel sichtbar zu machen.
Eine Zahnradpumpe pumpt das Wasser in den Aufbau, wo ein tangentialer Einlass und Auslass den Wasserstrom in die gewünschte Richtung leiten. Zur Messung der Wirbelgeschwindigkeit erfasst ein speziell entwickelter Sensor, der auf einer Lichtschranke basiert, Intensitätsänderungen an vier Punkten in radialer Richtung. Die Frequenz dieser Änderungen sind proportional zur Durchflussrate und werden durch Paddel (halbkugelförmig), die sich mit dem Wirbel bewegen, verursacht. Diese gemessenen Geschwindigkeiten wurden mit Strömungssimulationen desselben Systems kalibriert. Basierend auf diesen kalibrierten Messungen und den Navier-Stokes-Gleichungen in Zylinderkoordinaten wird ein Modell abgeleitet und mit Korrekturfaktoren an die Messungen angepasst. Für den Betrieb des Aufbaus wurde eine Kaskadenregelung entworfen. Der innere Regelkreis besteht aus der Pumpe und einem Integralregler. Weiters regelt ein Proportional-Integral-Regler die Stärke des Wirbels im äußeren Regelkreis.
Die gemessenen Daten zeigen, dass die Geschwindigkeit des Wirbels ungefähr proportional zur Durchflussrate der Pumpe ist. Das resultierende nichtlineare Geschwindigkeitsprofil zeigt zudem, dass es sich bei diesem System nicht um einen Starrkörper-Wirbel handelt. Die Modellvalidierung mit anderen Durchflussraten zeigt die Genauigkeit des angepassten Modells zur Beschreibung der Tangentialgeschwindigkeit des Wirbels. Zusätzlich ermöglicht die Kaskadenregelung, dass der Wirbel einen vorgegebenen Sollwert erreichen kann.

Contents

1 Introduction **1**
- 1.1 Motivation . . . 1
- 1.2 Literature Review . . . 1
- 1.3 Goals of This Thesis . . . 4
- 1.4 Contribution of This Thesis . . . 4
- 1.5 Structure of This Thesis . . . 5

2 Vortex Test Rig **6**
- 2.1 Generating a Vortex . . . 6
- 2.2 Dimensioning the Cylinder . . . 7
  - 2.2.1 Inlet and Outlet . . . 7
  - 2.2.2 Cylinder Lid and Pressure in the Cylinder . . . 12
  - 2.2.3 Bolts . . . 16
  - 2.2.4 Boundary Layer Thickness . . . 19
- 2.3 Printing a Watertight Cylinder . . . 22
  - 2.3.1 Flat Gasket for the Lid . . . 22
  - 2.3.2 Watertightness and Printing . . . 23
- 2.4 Water Tank . . . 24
- 2.5 Final Setup . . . 24
  - 2.5.1 Hardware . . . 24
  - 2.5.2 Software . . . 25
  - 2.5.3 Power Supply . . . 26
  - 2.5.4 Cylinder and Other Components . . . 26
  - 2.5.5 Sensors and Actuator . . . 27

3 Sensors and Actuators **28**
- 3.1 Sensors for Detecting the Vortex Velocities . . . 28
  - 3.1.1 Working Principle of the Sensor . . . 30
  - 3.1.2 Sensor Housing . . . 32
  - 3.1.3 Paddles for Flow Velocity Measurements . . . 32
  - 3.1.4 Circuit Design for Transimpedance Amplifier . . . 34
  - 3.1.5 LED Lighting for Light Barrier . . . 39
- 3.2 Hall Sensor for Measuring the Flow Rate . . . 41
- 3.3 Actuator . . . 43

4 Calibration with CFD Data **45**
- 4.1 CFD Software . . . 45
- 4.2 Calibration . . . 48

5 Control-Oriented Vortex Model **51**
5.1 Navier-Stokes Equations 51
5.2 Boundary Conditions 53
5.3 Initial Conditions 53
5.4 Solving the PDE 54
5.5 Fitted Model 58
5.6 Model Validation 60
5.7 Pressure Model 61
5.8 Dynamic Model 63

6 Controller for the Vortex **64**
6.1 Cascade Control 64
6.2 Pump Control 65
6.3 Controlling the Vortex 68
6.3.1 Feedforward Controller 69
6.3.2 Closed-Loop Control 71

7 Summary and Outlook **74**
7.1 Summary 74
7.2 Outlook 75

List of Figures

1.1 PIV arrangement with the laser at the side and the camera looking down on the flow domain from above [7]. 2
1.2 Vortex flow control unit with one inlet and outlet [10]. 3
1.3 Arrangement of splitter plate and cylinder [18]. 4

2.1 Test stand with labeled components. 6
2.2 Basic idea for a setup to create a vortex, consisting of all the main components. 7
2.3 Cylinder for vortex generation designed in SolidWorks. 9
2.4 Cutaway view of cylinder for vortex generation in SolidWorks. 10
2.5 Cutaway of hose barb fitting for the outlet designed in SolidWorks. . . . 10
2.6 Hose barb connection designed in SolidWorks. 11
2.7 Water tank with lid and connected hoses. The right hose is coming from the cylinder, while the left connects the tank with the pump. 11
2.8 Two points for calculating the pressure. The sensor is the hall sensor for measuring flow rate. 12
2.9 The bolts that hold the two lids, the gray gasket and the white cylinder. This combination allows for a visible vortex. 16
2.10 Forces acting on the flange gasket [28]. The thin crosshatch layer is the gasket and above is the acrylic lid. 17
2.11 Drawing of the arrangement regarding the two infinite disks for the Bödewadt boundary layer [33]. The bottom disk rotates and the top is stationary. 20
2.12 Left image with two perimeters and right with five, created in PrusaSlicer. 23
2.13 Dspace MicroLabBox with connected analog inputs and outputs. The only digital input, which is the hall sensor for measuring flow rate, is also connected. 25
2.14 Final setup filled up with water, with the light sensor on the side. The black paddles (hemispherical-cups) in the cylinder are responsible for velocity measurements. The water tank, hall sensor and pump are behind the cylinder. To protect the surrounding equipment against water, acrylic sheets are mounted on the sides. 26

3.1 Complete velocity sensor with the light barrier and paddles. 28
3.2 Velocity sensors consisting of the four light barriers. 29

3.3 Working principle of the light barrier with the cylinder, the side wall, the two lids, and one paddle depicted in the figure. In the left image, light is being blocked by the paddle and in the right image not. Below are the corresponding different voltage levels of the transimpedance amplifier. . . 29
3.4 Graph with time between two minima clearly labeled. 30
3.5 Voltage over time of the light barrier at a very low velocity. The single voltage drop caused by the paddle is clearly visible. 31
3.6 Voltage over time of the light barrier at higher speeds. 31
3.7 Velocity sensor housing from the side showing the position of the screws for adjusting the height. 32
3.8 The four paddles for each radius with the shaft and bearings in the center. 33
3.9 Sectional view of an arm and a paddle. The arm has a partially hollow structure. 33
3.10 Four transimpedance amplifier circuits, each with two photodiodes and one operational amplifier. The thin side walls reduce unwanted light. 34
3.11 Transimpedance amplifier circuit to amplify small currents coming from the two photodiodes. The MAX1044 switched-capacitor voltage converter that inverts the supply voltage for the TL071 is also shown. 35
3.12 Operational amplifier with dual-supply configuration. 36
3.13 Voltage over time of the light barrier for the innermost paddle at a flow rate of 4 L/min. 37
3.14 The rectangular aperture mask for creating a strip of light with a 2.5 mm opening. 38
3.15 The rectangular aperture mask inserted into the front part. Its height can be adjusted with bolts that are inserted in the labeled areas. 38
3.16 Light barrier with lights turned on. Visible are the projected light strips. 39
3.17 The LED lighting circuit. 39
3.18 Cover for light barrier against ambient light. 40
3.19 Measured velocity at the outermost paddle for a flow rate of 13 L/min. . 40
3.20 Hall sensor signal, after the voltage has been converted into a digital signal. 41
3.21 Pump and hall sensor. 42
3.22 ESCON motor driver for the gear pump. 43

4.1 Cylinder for 3D simulations. 45
4.2 Tetrahedral mesh for the cylinder. 46
4.3 Graph of the flow velocity as a function of the flow rate from the CFD data. 47
4.4 Graph of the flow velocity and flow rate, comparing CFD data, physical measurements and calibrated measurements for the outermost paddle (first paddle). 48
4.5 Graph of the flow velocity and flow rate, comparing CFD data, physical measurements and calibrated measurements for the second paddle. 49
4.6 Graph of the flow velocity and flow rate, comparing CFD data, physical measurements and calibrated measurements for the third paddle. 49
4.7 Graph of the flow velocity and flow rate, comparing CFD data, physical measurements and calibrated measurements for the fourth paddle. 50

5.1 Vortex velocities and flow rate from the test stand. 57
5.2 Graph of the model, calibrated measurements and CFD data for the tangential velocity at 13 L/min. 57
5.3 Graph of the fitted model, calibrated measurements and CFD data for the tangential velocity at 13 L/min and a height of 0.03 m. 58
5.4 Graphs of the fitted model and measurements from 9 to 12 L/min at a height of 0.03 m. 60
5.5 Graphs of the fitted model and measurements from 5 to 8 L/min at a height of 0.03 m. 61
5.6 Graph of the derived pressure model at a flow rate of 13 L/min at a height of 0.03 m without the pressure constant p_c. 62

6.1 Cascade control circuit with the pump and vortex. 64
6.2 Pump control circuit with integral controller. 65
6.3 Open-loop step response of the pump and estimated transfer function. . . 66
6.4 Bode plot of the open-loop transfer function $C_I(s)\,G_P(s)$ of the pump. . . 67
6.5 Measured closed-loop step response of the pump. 68
6.6 Basic feedforward control of the vortex. 69
6.7 Open-loop step response of the vortex and estimated transfer function. . . 69
6.8 Measured open-loop step response of the vortex. 70
6.9 Basic vortex control circuit. 71
6.10 Bode plot of the open-loop transfer function $C_{PI}(s)\,G_V(s)$ of the vortex. . 72
6.11 Measured closed-loop step response of the vortex for the velocity at the outermost paddle. 73

List of Tables

2.1 Parameters of the head loss equation. 13
2.2 Parameters for forces acting on the flange gasket. 17
2.3 Parameters in Figure 2.11. 21
2.4 Boundary layer thickness at low angular velocities. 21

3.1 Position of the four paddles (hemispherical-cups) along the radius. 34

4.1 Numerical values of the parameters [49]. 47

5.1 Numerical values of the parameters for the boundary conditions. 53
5.2 Numerical values of the coefficients of the flow rate function. 57
5.3 Numerical values of the coefficients of the flow rate function $B_f(Q)$. . . . 59
5.4 Numerical values of the coefficients of the flow rate function. 63

6.1 Control circuit symbols part one for Figure 6.1. 64
6.2 Control circuit symbols part two for Figure 6.1. 65

1 Introduction

This chapter introduces the thesis and addresses the motivation. Additionally, the state of the art regarding vortex control, applications, analysis of the flow, and flow modeling is discussed. Also the main goals of this thesis are briefly outlined. In the end, the contribution of this thesis and the structure are mentioned.

1.1 Motivation

Vortices are an essential part of many fluid flow patterns and there still is enough research to be done in this scientific area. Moreover, there are different types of vortices with very specific characteristics. Gaining a better understanding of their structure and possibilities to influence them is an additional motivation of this work.

1.2 Literature Review

Many different areas of research regarding vortices exist. This section takes a brief look at what type of technologies and approaches exist for controlling and changing these, as well as analyzing, modeling, and harnessing energy from vortices.
As discussed in different papers, vortex generators have been built that aim to use the energy from vortices to produce electricity. These systems have a conical or cylindrical container without a lid, which is put to use for making vortices [1]. One example is a vortex power plant that uses waste water from a fish farm to produce electricity with a water turbine that is powered by the vortex [2]. For this specific case, Computational Fluid Dynamics (CFD) simulations for the vortex were carried out. There are also other approaches for power plants, with the aim of generating electricity with vortices [3]. Furthermore, there is also research in the area of electricity generation from vortex-induced vibrations in train tunnels [4].
For studying and visualizing the flow in vortices, different methods are applied. One of them is adding black sesame seeds to water [5]. These seeds move with the flowing water and due to their distinct color the vortex can be visualized.
Another method widely applied for analyzing different types of flow, including vortices, is Particle Image Velocimetry (PIV) [6]. This method requires the addition of special small particles that have a similar density to the medium they are placed in. A laser is necessary to illuminate these small objects in water. The flow is then filmed with a camera and the footage later analyzed with a computer [7]. An entire vector field of the velocities is generated after the recorded videos are processed. This allows to look at a flow in detail but also generates large amounts of data. Figure 1.1 shows a simplified PIV

arrangement. The laser illuminates the particles in the flow domain from the side and the camera is filming from above.

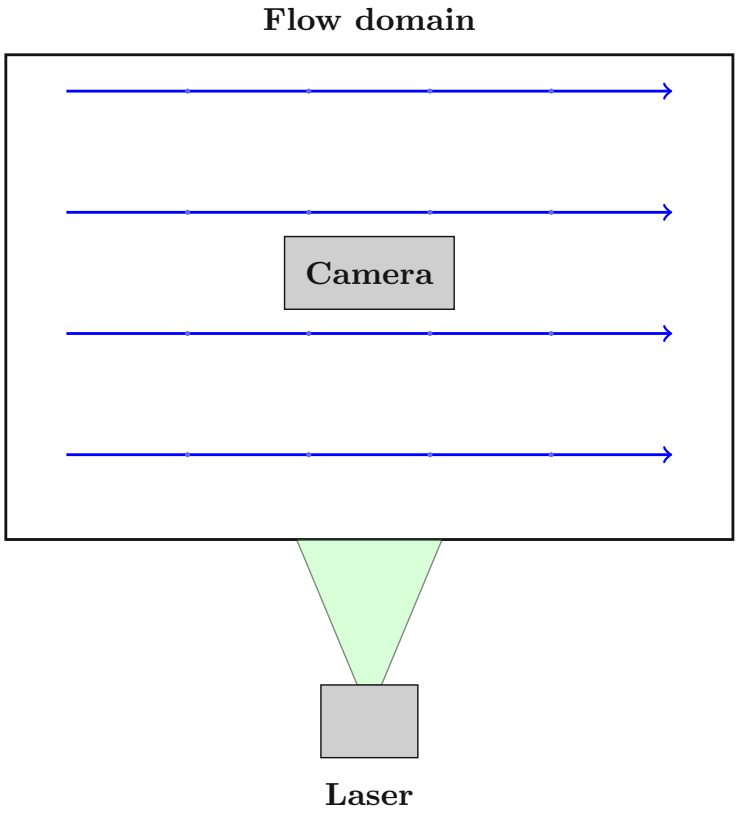

Figure 1.1: PIV arrangement with the laser at the side and the camera looking down on the flow domain from above [7].

Mathematical models for vortices are another area of scientific research. For example, a model for vortex streams in the slab continuous casting mold and analysis with a water model is a specific example of this [8].
Numerous other methods for actively controlling and changing vortices also exist. One active control method can alter the structure of the vortex core by axial momentum injection as shown in a numerical simulation [9]. It also demonstrates that this approach can increase the pressure in the center and improve the operation of pumps.
Apart from this, special vortex flow control units can be used to mitigate or prevent flooding linked to stormwater [10]. These devices, with an inlet and outlet as shown in Figure 1.2, operate with less losses than an orifice plate at low flow rates, which is a very simple device that restricts flow with a circular opening [11]. This means, when a storm is starting more water can be pumped out and upstream water storage reservoirs can be used more effectively. Such vortex control units are also successfully used to prevent the sewer system from flooding, with success.
Methods for reducing the vortex induced motion at spars is also investigated with different methods in [12]. An active method that injects high pressure water can significantly

disrupt such vortices and reduce their effects. Passive injection also works but is less effective.

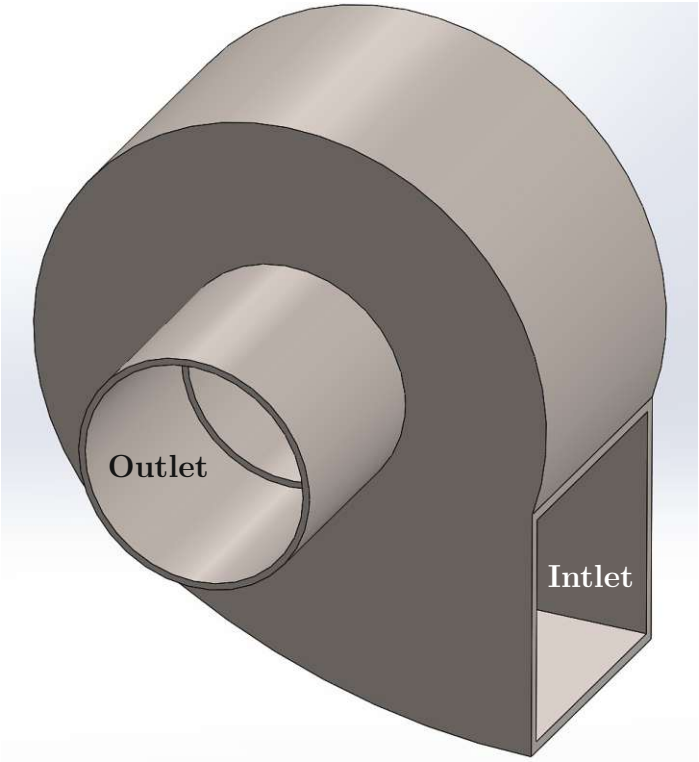

Figure 1.2: Vortex flow control unit with one inlet and outlet [10].

Another passive method looks at the suppression of vortex induced vibrations for a cactus-shaped cylinder at low Reynolds numbers [13]. These can cause damage to structures that are exposed to such forces. Therefore, the effect of fully porous and partially porous spines that are on the surface of a cylinder is explored. In addition, these spines are permeable to different degrees. With a certain combination of these, the amplitude of such oscillations can be reduced. Active methods to reduce such vortex induced vibrations also exist, for example, a Proportional-Integral-Derivative (PID) controller combined with a wake oscillator [14].
There are also numerous papers on reducing the effects of vortex shedding, which is the formation of swirls or the Karman vortex street, for example behind a cylinder when water is flowing past it [15]. So, one approach is injecting fluid and drawing it in through openings on the cylinder, with pressure measurements for the controller [16]. Likewise, control rods that are placed behind the cylinder can be utilized to alter the flow where vortex shedding takes places [17].
Another simple passive method for influencing fluid forces created by the formation of a Karman vortex street behind a cylinder is the use of splitter plates [18]. These are placed behind the cylinder that is placed in a flow and this way the vortices can be disrupted and the resulting forces reduced. This arrangement is shown in Figure 1.3.

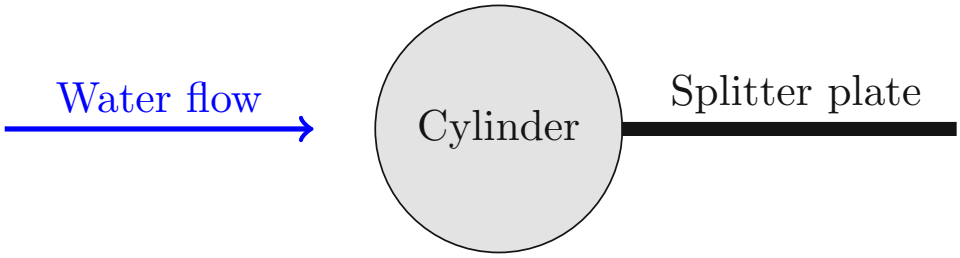

Figure 1.3: Arrangement of splitter plate and cylinder [18].

1.3 Goals of This Thesis

There are three main objectives for this thesis, as listed below.

1. Design and build a test stand that allows to study and measure a confined water vortex.
2. Implement a working control architecture for the vortex.
3. To develop and validate a model of the water vortex.

1.4 Contribution of This Thesis

At present, there is limited research in the area of active vortex control, especially how such a system can be operated in a closed-loop manner. In this work, a tailored setup which can create a vortex is designed and built. The vortex is confined to a cylinder with a bottom and top lid and almost no air inside. The majority of existing vortex control systems are not pressurized, lacking the top lid and this way creating a different vortex. Moreover, not many systems explore the active control of vortices. Another unique feature is the outlet, which is shaped like the inlet, i.e. tangential and located at the side. This means, that the vortex is mainly characterized by a tangential velocity component and can be studied in a controlled environment.
The manufactured setup is made of the thermoplastic Polylactide (PLA), which shows that this 3D-printing material is also suitable for water circuits. Although it has to be coated with an extra layer, in this case candle wax, the setup can withstand low water pressure without leaking. This is a remarkable result and demonstrates that fluid dynamics can be studied with additionally processed printed parts from a standard 3D printer.
Furthermore, the specially developed and tested velocity sensor for the vortex, shows possibilities and limitations of measuring and controlling the strength of a vortex. In addition, this work demonstrates how the sensor, which consists of four light barriers can support the modeling of vortices.
In fact, a model is derived for this specific vortex based on measurements taken with the setup that can be used to obtain the tangential velocity as a function of the axial z coordinate, the radius and the flow rate.

Finally, cascade control is successfully implemented for the test rig, with the inner loop controlling the pump flow rate and the outer the vortex strength. So, this control configuration can reach a given setpoint and highlights possibilities for similar systems.

1.5 Structure of This Thesis

The idea and how this test stand is designed and built is clarified in Chapter 2. Chapter 3 describes the sensors and the utilized actuator, to enable closed-loop operation. Subsequently, Chapter 4 presents the calibration of the measured velocities with data from CFD simulations. Then in Chapter 5, the model of the vortex confined to the cylinder is derived, examined, and validated with calibrated measurements. Chapter 6 examines the designed and implemented controllers for the actuator and vortex. This chapter also presents the resulting closed-loop step responses, which are measured with the physical system. Finally, a conclusion is drawn in Chapter 7.

2 Vortex Test Rig

To create a water vortex confined to a cylinder, a watertight test stand is constructed. Additionally, the system has to withstand pressure and should make the water flow visible. Therefore, this chapter deals with how the test stand is designed and built. First of all, the principle idea of the test rig is explained. Then dimensioning of the cylinder and manufacturing are described. After that, the water tank and final setup are elaborated in more detail.

2.1 Generating a Vortex

To generate a vortex, a round container in the form of a 3D printed cylinder is used in this work. Based on a few simple test setups, the shape of a tangential water inlet was optimized. In Figure 2.1 the test setup is shown with labeled components. The pump and the hall sensor cannot be seen, as these are behind the cylinder and therefore, the approximate locations are labeled.

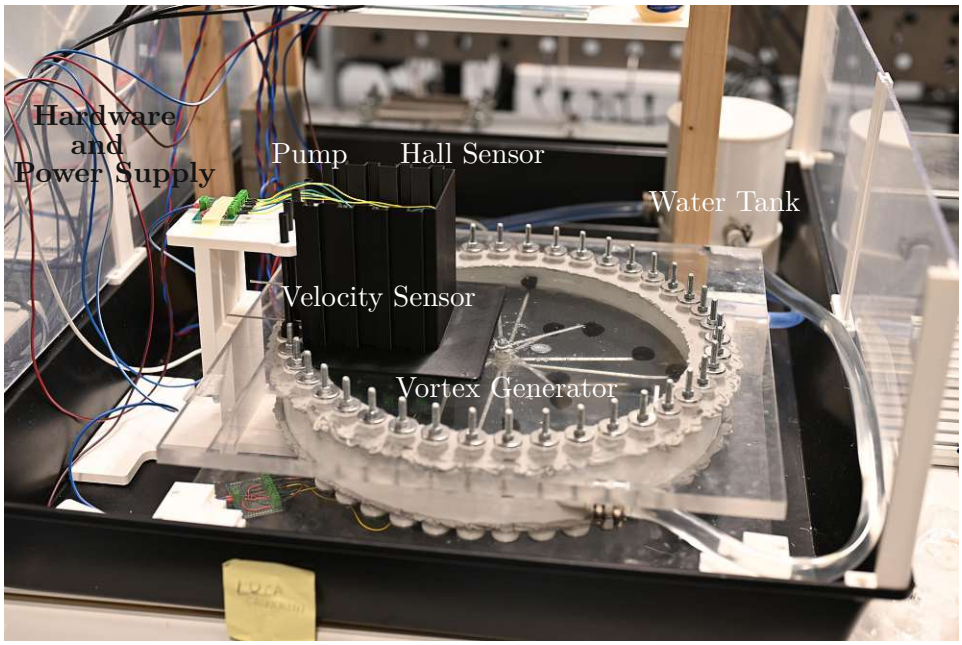

Figure 2.1: Test stand with labeled components.

Figure 2.2 shows the concept of the test stand, with an overview of all essential components, which are labeled in Figure 2.1. In order to excite a vortex, a cylinder with a tangential inlet and outlet is used. This results in a mainly circular flow. To generate this flow, a

gear pump is used and a hall sensor to measure the flow rate. In addition, velocity sensors consisting of light barriers that detect intensity changes, are utilized to measure how fast the water is spinning. Electrical components of the test rig are powered with a power supply and controlled via hardware that is explained later. Additionally, a water tank serves as a reservoir to fill up the system with water and remove excess air.

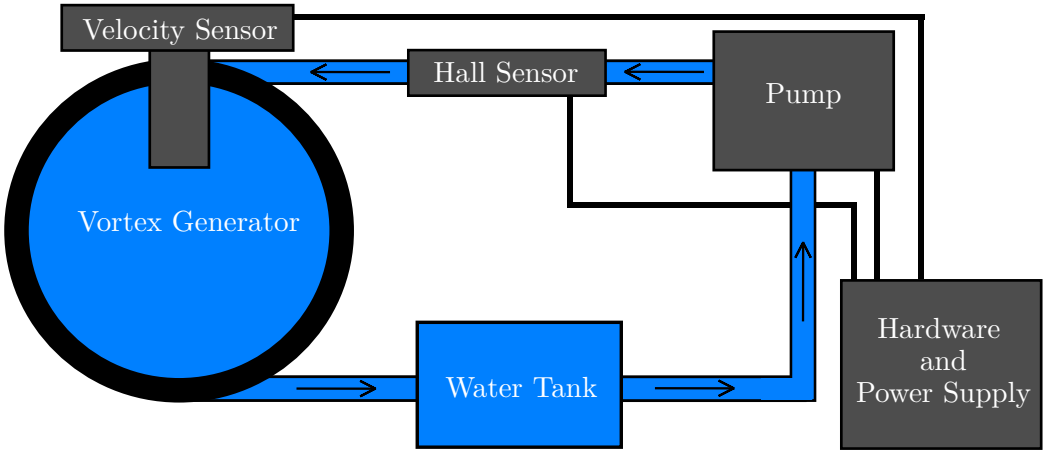

Figure 2.2: Basic idea for a setup to create a vortex, consisting of all the main components.

2.2 Dimensioning the Cylinder

The relevant forces that act on the components in the water circuit have to be taken into account. All parts of the water circuit experience pressure but the cylinder experiences the highest pressure forces due to its large surface area. Especially, the bottom and top lid have large surfaces. This section concentrates on the calculations that are required for dimensioning the cylinder and for selecting the correct components. Clearly, the water circuit should not leak.

2.2.1 Inlet and Outlet

In order to create a vortex that can be visualized, a certain flow velocity has to be reached at the inlet. First of all, the targeted rotations per second of the vortex are chosen and then the necessary speed at the inlet is calculated. Then, the maximum cross sectional area for the required velocity has to be determined, for a pump that has a maximum flow rate of 15 liters per minute (L/min).
The targeted rotations per second of the vortex, are

$$f_t = 4.5 \text{ Hz}. \tag{2.1}$$

Hence, the required velocity at the inlet can be calculated, given the inner radius of the cylinder. Which is chosen to be

$$R_{inner} = 0.1802 \text{ m}. \tag{2.2}$$

Then the volumetric flow rate equation [19] can be rearranged to

$$Q = v \cdot A \rightarrow v = \frac{Q}{A}. \tag{2.3}$$

The inlet velocity equals

$$v_{inlet} = 2 \cdot \pi \cdot R_{inner} \cdot f_t = 5.096 \text{ m/s}. \tag{2.4}$$

With the velocity at the inlet determined, the maximum cross sectional area can be calculated. The volumetric flow rate of the available pump is

$$Q_{pump} = 15 \text{ L/min} = 0.00025 \text{ m}^3/\text{s}. \tag{2.5}$$

This means, that the maximum cross sectional area of the inlet can be

$$A_{max} = \frac{Q_{pump}}{v_{inlet}} = 0.00004906 \text{ m}^2. \tag{2.6}$$

The designed inlet of the cylinder has a cross sectional area of

$$A_{inlet} = 0.00004463 \text{ m}^2 < A_{max}. \tag{2.7}$$

The resulting volumetric flow rate with such an inlet is

$$Q_{in} = v_{inlet} \cdot A_{inlet} = 0.00022746 \text{ m}^3/\text{s} = 13.6 \text{ L/min} < Q_{pump}. \tag{2.8}$$

So, based on these calculations, a pump with a flow rate of at least 13.6 L/min is required. Therefore, the pump with a maximum flow rate of 15 L/min is suited for the task. The outlet is designed larger than the inlet to reduce pressure buildup in the cylinder. The designed outlet has the cross sectional area

$$A_{outlet} = 0.00010027 \text{ m}^2. \tag{2.9}$$

Hence, the speed of the water directly at the outlet equals

$$v_{outlet} = \frac{Q_{in}}{A_{outlet}} = 2.268\text{m/s}. \tag{2.10}$$

This is smaller than the inlet velocity v_{inlet}. Despite $A_{inlet} \neq A_{outlet}$, the inner diameter at the tip of the two hose fittings that connect the hoses with the cylinder is the same. So, the water is leaving and entering the system with the same velocity where the hoses are connected to the cylinder.
The location of the hose connections is also an essential design decision. This decision is made based on preliminary setups. Placing the inlet and outlet near to each other is problematic, as this can create a short circuit for the water flow. The best configuration is with inlet and outlet being placed on opposite positions along the cylinder (see Figure

2.3). Furthermore, the arrangement of the inlet and outlet is in the tangential direction of the main water flow of the vortex. This arrangement is depicted in Figure 2.3 and 2.4. Figure 2.3 shows the placement of inlet and outlet in the middle plane between the bottom and top, i.e. at a height of 30 mm. Figure 2.4 shows the channels inside the cylinder walls. These have to be designed this specific way, to have enough space for the bolt holes needed to fasten the lid on the bottom and top. Sharp edges are avoided in the channel design to minimize the flow resistance and aid the flow into and out of the system [20].

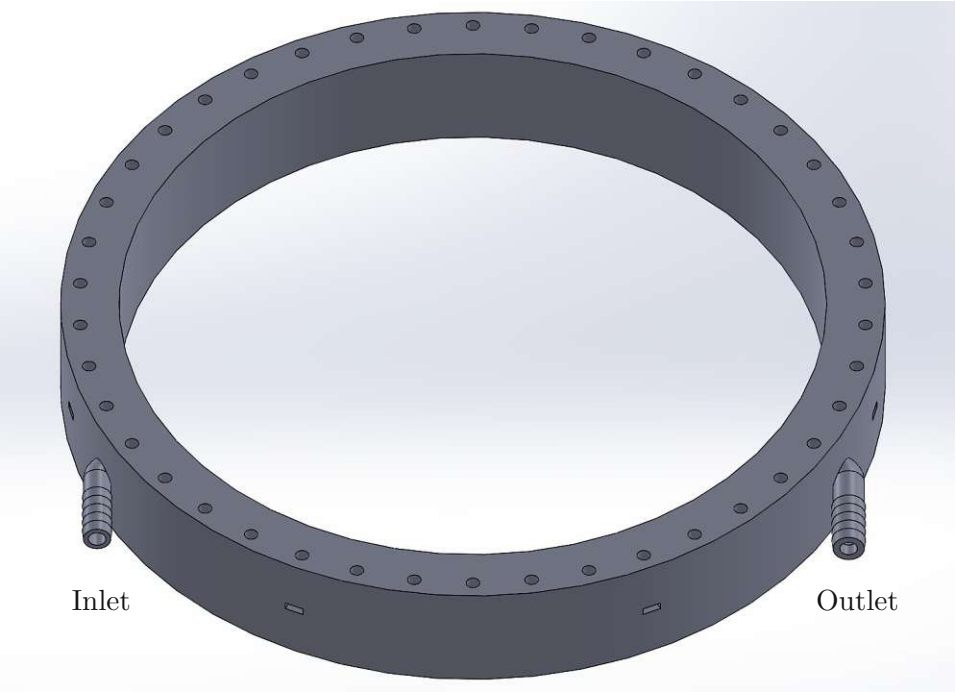

Figure 2.3: Cylinder for vortex generation designed in SolidWorks.

One of the standard ways to seal a hose that is connected to a component in a fluid circuit is the so called hose barb fitting. This geometry consists of barbs that are wider than the inner diameter of the hose. So, this holds the hose in place and helps to seal the connection [21]. The sealing effect comes from the shape, by which the hose is stretched at the barbs. If necessary, hose clamps can be placed over the hose to amplify the sealing geometry effect.
For the considered system, five barbs are used as shown in Figures 2.5 and 2.6. This way, the surface is larger and allows the usage of up to two hose clamps. The hose for the cylinder inlet has an inner diameter of 14 mm. The outlet is connected to a hose with an inner diameter of 16 mm. This ensures reduced pressure losses in the outlet duct.
Two hose clamps are assembled at the outlet and inlet. In addition to this, the outer diameter at the barbs for the inlet is 15 mm and for the outlet 17.2 mm. These measures ensure that the hoses do not leak at the interface.
Before the assembly, all the printed hose connections are smoothed and cleaned with acetone. Due to their rather rough surface, which results from the round structure and

the limited accuracy of the printer, the hose connections are covered with a layer of wax. The very last layer that is applied is standard Vaseline (petroleum jelly), in order to fill all remaining uneven spots [22]. Moreover, Vaseline is readily available and does not create any additional problems during operation. So, apart from candle wax an additional layer between the hose and printed material helps to seal this vital interface.

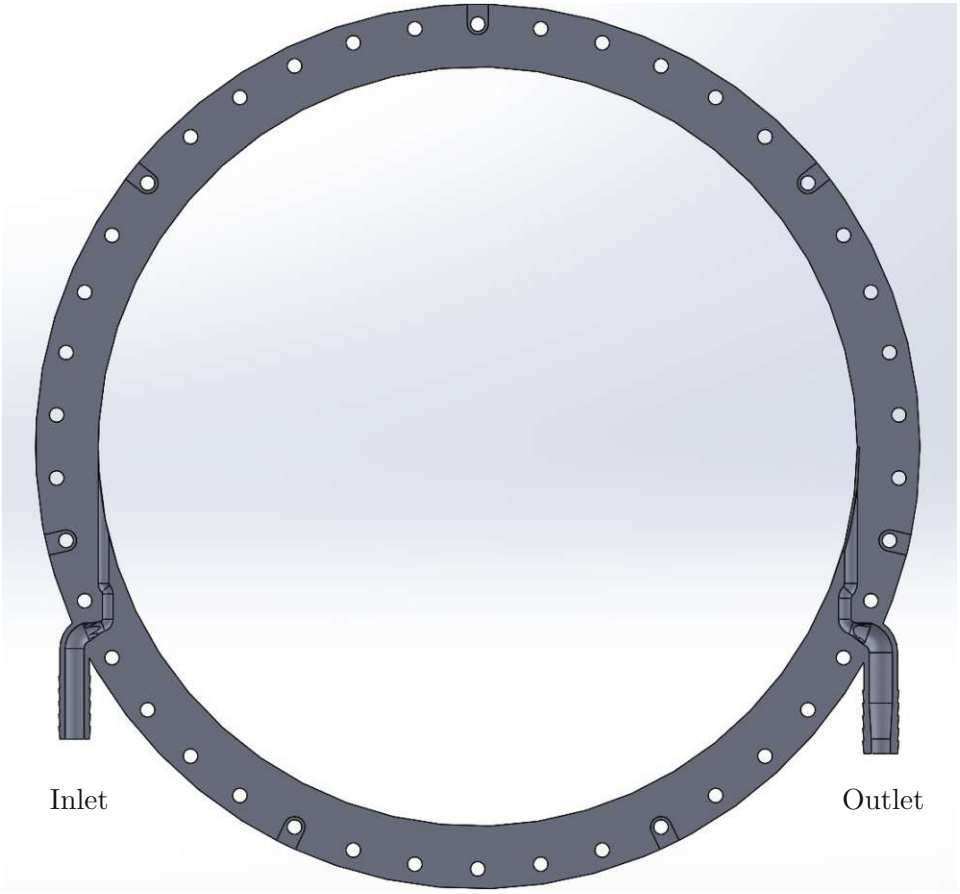

Figure 2.4: Cutaway view of cylinder for vortex generation in SolidWorks.

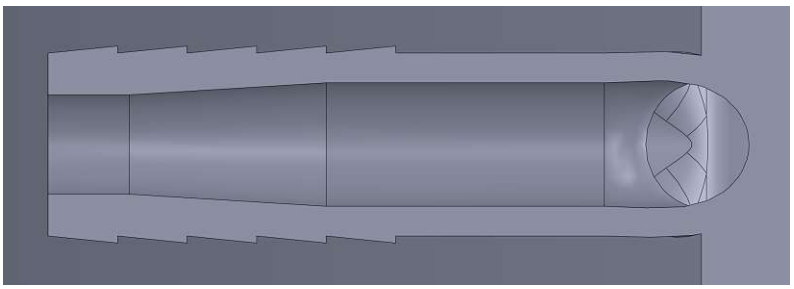

Figure 2.5: Cutaway of hose barb fitting for the outlet designed in SolidWorks.

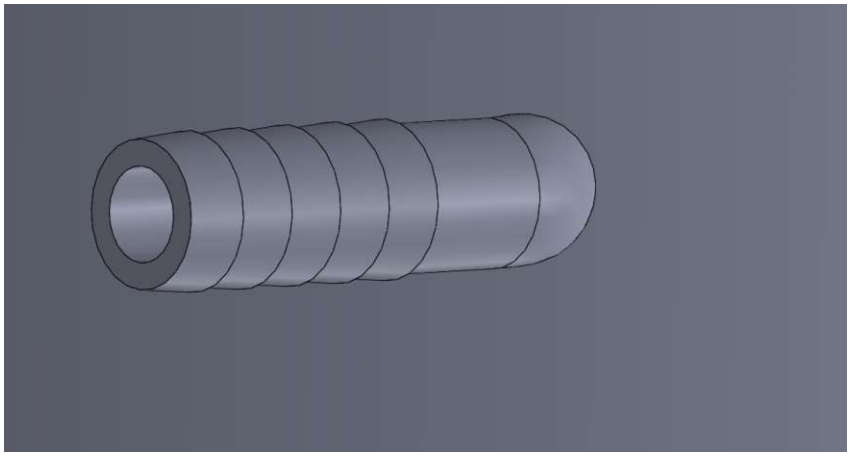

Figure 2.6: Hose barb connection designed in SolidWorks.

In Figure 2.7 the water tank with the lid on top and a printed stand below is shown. Two hose clamps are used for each hose fitting.

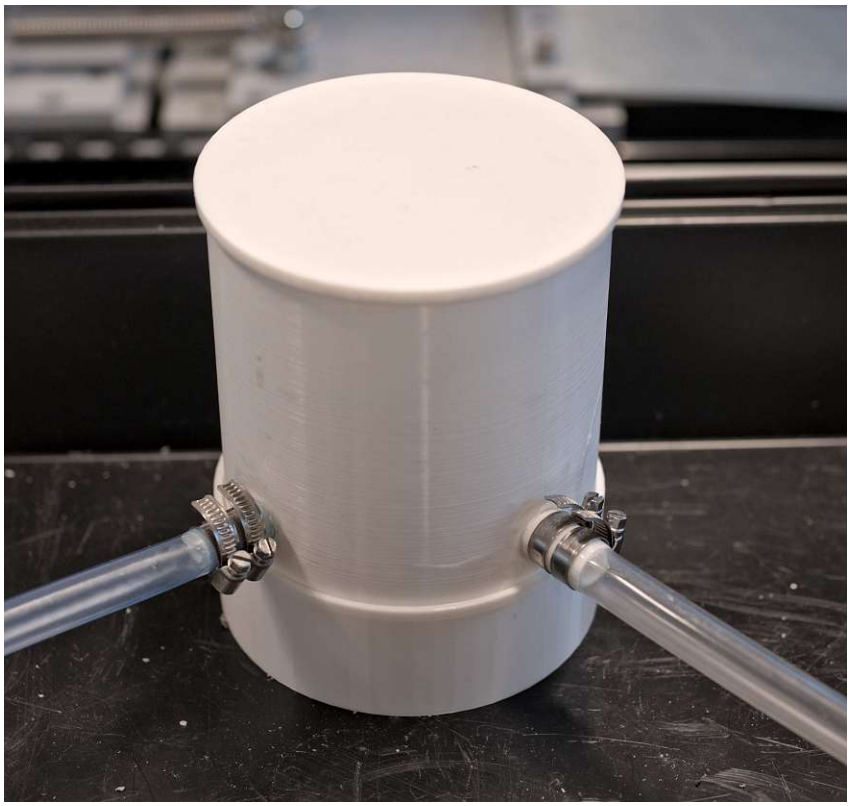

Figure 2.7: Water tank with lid and connected hoses. The right hose is coming from the cylinder, while the left connects the tank with the pump.

2.2.2 Cylinder Lid and Pressure in the Cylinder

A crucial design parameter is the maximum pressure that can be established in the system. To prevent failure of parts, calculations regarding the pressure-dependent forces are required. The two lids experience the greatest pressure force due to their large surface area. Therefore, the focus will be on these parts of the system. The density of water at 20 °C is

$$\rho = 998.3 \text{ kg/m}^3 \tag{2.11}$$

and the acceleration due to gravity equals

$$g = 9.81 \text{ m/s}^2. \tag{2.12}$$

The static pressure

$$p_{stat} = \rho g h \tag{2.13}$$

affects only the bottom lid. The dynamic pressure

$$p_{dyn} = \frac{1}{2}\rho v^2 \tag{2.14}$$

depends on the velocity [19], assuming the density does not change. The pressure in the cylinder is calculated with the equation

$$z_1 + \frac{p_1}{\rho g} + \frac{v_1^2}{2g} + h_p = z_2 + \frac{p_2}{\rho g} + \frac{v_2^2}{2g} + h_t. \tag{2.15}$$

This is the extended Bernoulli equation [19]. The term h_p on the left side is the pump head that comes from the pump adding pressure. Similarly, h_t stands for the total head loss. For the equation two points that are on the same streamline need to be selected. The left side of (2.15) is the first point and the right side the second point on this streamline.

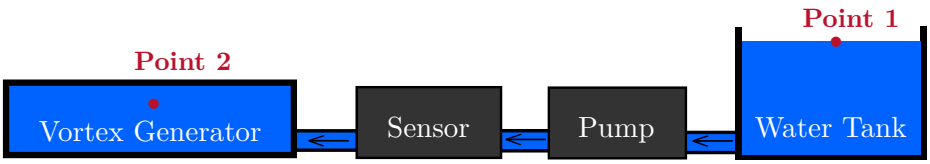

Figure 2.8: Two points for calculating the pressure. The sensor is the hall sensor for measuring flow rate.

The first point is on the water surface of the water tank. To calculate the pressure in the cylinder the second point is in the center of the vortex. In Figure 2.8 the two points are clearly labeled. As the heights are small these can be neglected and therefore,

$$z_1 = z_2 = 0. \tag{2.16}$$

Then rearranging the equation (2.15) yields

$$p_2 = \rho g \left(\frac{p_1}{\rho g} + \frac{v_1^2 - v_2^2}{2g} + h_p - h_t \right). \tag{2.17}$$

The equation (2.17) allows to calculate the pressure p_2 in center of the vortex. The velocity at the first point equals

$$v_1 = 0 \text{ m/s} \tag{2.18}$$

and the absolute pressure is

$$p_1 = 100000 \text{ Pa}. \tag{2.19}$$

The velocity at the second point in the center of the vortex equals

$$v_2 = 0 \text{ m/s}. \tag{2.20}$$

The head loss is also determined. Avoiding unnecessary pressure buildup and losses is important for the setup. For example, reducing the diameter of a hose in the system will result in additional losses. The following frictional head loss expression (also called Darcy's equation, see[23])

$$h_f = f_r \frac{Lv^2}{2Dg} \tag{2.21}$$

can be used to model the friction in pipes and hoses. Table 2.1 clarifies what each parameter in (2.21) means.

Parameter	**Meaning**
f_r	Friction factor
L	Length of hose
v	Velocity
D	Diameter of hose
g	Acceleration due to gravity

Table 2.1: Parameters of the head loss equation.

Based on this equation, a short hose with a large diameter, low velocity, and a smooth surface, which means a smaller f_r, is the optimal combination. Sharp edges and turns are problematic because they cause pressure losses. Therefore, sharp edges and turns are also avoided, when possible. This applies also to the inlet and outlet. The two lids experience the greatest forces because of their large area.
For further calculations the pump head is

$$h_p = 2.703 \text{ m}. \tag{2.22}$$

This value is determined from the ampere-draw diagram in the data sheet of the pump [24], as the pump draws 2.756 A at 24 V. The length of the hose form the water tank to the vortex generator is

$$L = 1.5 \text{ m}. \tag{2.23}$$

The distance covered by the water from the inlet hose fitting to the center of the cylinder is neglected. This is due to the difficulty of estimating the losses for this section. The diameter of the hose is

$$D_{hose} = 0.014 \text{ m} \tag{2.24}$$

and the cross-sectional area

$$A_{hose} = \pi\left(\frac{D_{hose}}{2}\right)^2 = 0.0001539 \text{ m}^2. \tag{2.25}$$

For the pump head (2.22) the flow rate is

$$Q_{pump} = 14.115 \text{ L/min} = 0.0002353 \text{ m}^3/\text{s}. \tag{2.26}$$

This is determined from the flow rate diagram in the data sheet of the pump [24]. Hence, the velocity in the hose is

$$v_{hose} = \frac{Q_{pump}}{A_{hose}} = 1.528 \text{ m/s}. \tag{2.27}$$

Additionally, the dynamic viscosity of water at 20 °C is

$$\mu = 0.001 \text{ Pa} \cdot \text{s} \tag{2.28}$$

and the density for water at 20 °C is given in (2.11) [19]. This allows to determine the kinematic viscosity as follows

$$\nu = \frac{\mu}{\rho} = 1.002 \cdot 10^{-6} \text{ m}^2/\text{s}. \tag{2.29}$$

The Reynolds number [19] in the hose equals

$$Re_{hose} = \frac{v_{hose} D_{hose}}{\nu} = 21352.27. \tag{2.30}$$

The roughness of the rubber hose [19] equals

$$k = 0.0016 \text{ mm}. \tag{2.31}$$

and the relative roughness is

$$\frac{D_{hose}}{k} = 8750. \tag{2.32}$$

With the Reynolds number (2.30), relative roughness (2.32) and the Moody chart from [19] the friction factor approximately equals

$$f_r = 0.026. \tag{2.33}$$

With these parameters the frictional head loss equals

$$h_f = \frac{f_r L (v_{hose})^2}{2 D_{hose} g} = 0.3316 \text{ m}. \tag{2.34}$$

Additionally, the total head loss is

$$h_t = h_f + h_{add}. \tag{2.35}$$

The additional losses are

$$h_{add} = h_{hall} + h_{cyl}. \tag{2.36}$$

These consist of the flow meter h_{hall} and the section from the inlet hose fitting to the center of the cylinder h_{cyl}. For both cases the friction factor f_r is unknown. Therefore, these losses are not part of the calculation and $h_t = h_f$. With (2.17) the pressure in the center of the vortex is

$$p_2 = 123222.6 \text{ Pa}. \tag{2.37}$$

Hence, the overpressure is

$$p_{over} = 23222.6 \text{ Pa} \tag{2.38}$$

and with the following surface area

$$A_{lid} = 0.1020538 \text{ m}^2 \tag{2.39}$$

the force on the lid equals

$$F_{lid} = p_{over} \cdot A_{lid} = 2369.95 \text{ N}. \tag{2.40}$$

For the following calculations, it is assumed that the pressure is uniform over the surface area of the lid. The hydrostatic static pressure on the bottom lid is neglected, as the resulting forces are significantly smaller. Therefore, p_{over} in the center of the vortex is used to determine the force acting on the lid. This results in a safer estimation because the static pressure on the lid is the greatest in the center, as the dynamic pressure is zero. For calculating the deflection of the lid, Young's modulus [25]

$$E = \frac{\sigma}{\epsilon} \tag{2.41}$$

is required. E stands for the relationship between the applied axial stress σ and the resulting strain ϵ, as shown in (2.41) [26]. A larger number means a smaller deflection and thus a stiffer material. According to the data sheet [27], the value for acrylic glass is

$$E_{ac} = 3300 \text{ MPa}. \tag{2.42}$$

Two crucial design parameters are the thickness of the lid

$$h_{ac} = 0.015 \text{ m} \tag{2.43}$$

and its water contact radius

$$R_{ac} = 0.1802 \text{ m} \tag{2.44}$$

(that is experiencing the pressure). The following equation gives the deflection of the lid in the center, according to [25].

$$d_{center} = 0.171 \cdot \frac{p_{over} \cdot R_{ac}^4}{E_{ac} \cdot h_{ac}^3} = 0.3762 \cdot 10^{-3} \text{ m} \tag{2.45}$$

It becomes clear how vital R_{ac} and h_{ac} are. This means that a thick lid reduces and a large surface increases the probability of deformations on the acrylic lid. The maximum deflection according to (2.45) is acceptable.

2.2.3 Bolts

One of the key requirements is the possibility of visually seeing the vortex. Transparent lids are mandatory to fulfill this criterion. This is why acrylic lids are assembled onto the 3D printed side wall of the cylinder. Between these components, a seal or gasket is required.
Figure 2.9 shows the finished setup with the gasket between the lid and cylinder wall. The gasket is realized as a blind flange filled with silicone. The formulas and related constants in the following design calculations are taken from [28].

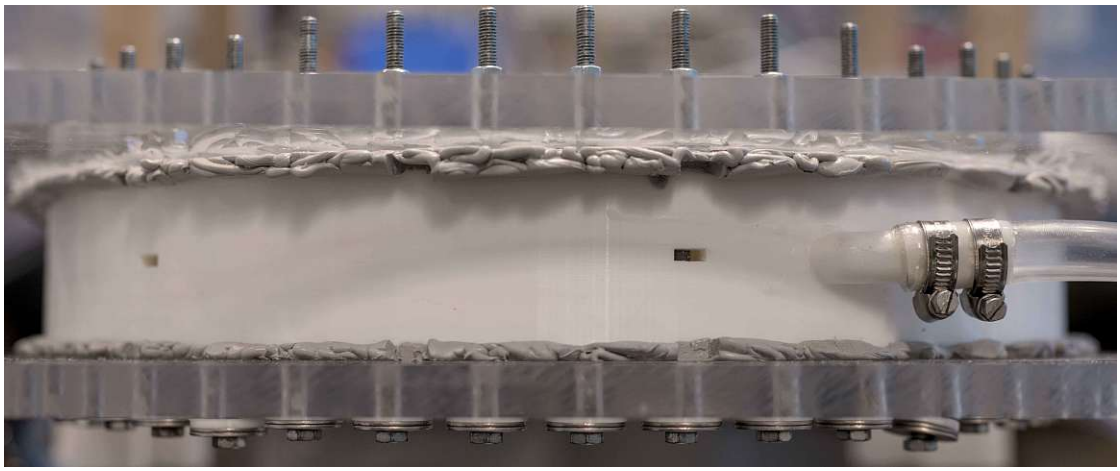

Figure 2.9: The bolts that hold the two lids, the gray gasket and the white cylinder. This combination allows for a visible vortex.

The pressure $p_{over} = 23222.6 \text{ N/m}^2$ that acts on the lids was determined in (2.38). Based on this pressure, the forces in Figure 2.10 are calculated. The thin crosshatch layer represents the silicone gasket. The thicker hatched layer represents the acrylic lid. The

white area with the symmetry line stands for the bolt hole. Table 2.2 describes the parameters in Figure 2.10. The figure shows the forces acting on the lid and the gasket.

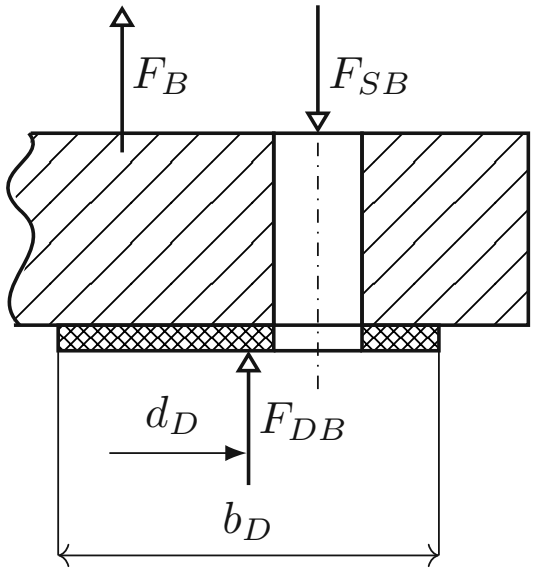

Figure 2.10: Forces acting on the flange gasket [28]. The thin crosshatch layer is the gasket and above is the acrylic lid.

Parameter	Description
d_D	Mean diameter of the gasket
F_{SB}	Minimum force exerted by the bolts
F_{DB}	Force on the gasket
F_B	Pressure force exerted on the lid
b_D	Width of the gasket

Table 2.2: Parameters for forces acting on the flange gasket.

The number of bolts needs to be chosen, before the bolts are selected. As the lid is very stiff and the pressure not problematic, the distance

$$d_{screw} = 30 \text{ mm} \tag{2.46}$$

is assumed between neighboring screws. The bolts are placed at the radius

$$R_{screw} = 200.54 \text{ mm}, \tag{2.47}$$

which is closer to the outer wall. The resulting perimeter is

$$d_{peri} = 2\pi R_{screw} = 1260.00 \text{ mm}. \tag{2.48}$$

Then the number of necessary bolts is

$$n = \frac{d_{peri}}{d_{screw}} = 42. \tag{2.49}$$

Based on this design decision, the required bolt type is determined. The first considered parameter

$$b_D = 0.02976 \text{ m} \tag{2.50}$$

is the width of the gasket, see Figure 2.10. The next value

$$k_1 = 0.5 \cdot b_D = 0.01488 \text{ m} \tag{2.51}$$

stands for the effective sealing width of the gasket during normal operation.

$$S_D = 1.2 \tag{2.52}$$

is a safety factor. The next parameter is

$$Z = 2.91 \tag{2.53}$$

is an additional safety parameter [28]. Again, the largest value is selected for a material with an unknown yield point, to ensure that the system can withstand the pressure. Finally,

$$K = 640 \text{ N/mm}^2 \tag{2.54}$$

is the yield stress for the threaded bolts with material class 8.8. Now the forces can be determined and the required core diameter of the threaded bolts. The force acting on the lid is

$$F_B = p_{over} \ \pi \ {d_D}^2 \frac{1}{4} = 2777.5 \text{ N}. \tag{2.55}$$

The following force

$$F_{DB} = \pi \ d_D \ p_{over} \ S_D \ k_1 = 508.4 \text{ N} \tag{2.56}$$

acts on the clamped gasket and therefore, the bolts need to carry the force

$$F_{SB} = F_B + F_{DB} = 3285.9 \text{ N}. \tag{2.57}$$

Finally, an additional safety factor

$$c_{add} = \frac{65 - Z\sqrt{\frac{F_{SB}}{K \cdot n}}}{15} = 4.266 \text{ mm} \tag{2.58}$$

for the core diameter of the bolts is required. This additional safety factor should not be greater than 3 mm. Therefore, it is set to the value

$$c_{add} = 3 \text{ mm}. \tag{2.59}$$

The required core diameter then equals

$$d_3 = Z\sqrt{\frac{F_{SB}}{K \cdot n}} + c_{add} = 4.017 \text{ mm}. \tag{2.60}$$

Based on this value, appropriate screws need to be selected. M6 screws have a core diameter [28] of

$$d_{3M6} = 4.773 \text{ mm}. \tag{2.61}$$

This is more than enough and fulfills the requirements. With these numbers, the required distance between the screws can be determined. The first essential parameter

$$d_w = 10 \text{ mm} \tag{2.62}$$

is the diameter of the M6 screw head. This is followed by the thickness of the lid, which is

$$h_{min} = 15 \text{ mm}. \tag{2.63}$$

The minimum separation between the screws of a flange [28] should be

$$D_A = d_w + 2h_{min} = 40 \text{ mm}. \tag{2.64}$$

This is larger than the assumed distance of 30 mm. To sum up, a total of 42 galvanized M6 bolts with material class 8.8 are selected for the cylinder. Together with the thick lid they ensure that the cylinder is watertight.

2.2.4 Boundary Layer Thickness

At the surfaces inside of the cylinder, a so called boundary layer forms. The main reasons for this phenomenon are no-slip conditions directly at the surface and viscous friction in the nearby fluid volumes. Boundary layers can be laminar or turbulent and often times there is a transition region from laminar to turbulent [29]. The goal for this section is to estimate the thickness of the boundary layer to make sure the cylinder is large enough to mitigate the influence of the boundary layer, as the focus of this work is not on examining this phenomenon.
One important dimensionless number that is essential here is the Reynolds number. It helps to categorize whether the flow in a boundary layer is turbulent or laminar. The Reynolds number and its threshold to distinguish between laminar and turbulent flow depend on the respective geometry. A higher velocity results in a larger Reynolds number [19]. This is clear from the definition

$$Re = \frac{vl\rho}{\mu} = \frac{vl}{\nu}. \tag{2.65}$$

For the calculations, the dynamic viscosity from (2.28) is used and the kinematic viscosity (2.29). The next parameter

$$f_v = 4.5 \text{ Hz} \tag{2.66}$$

is the frequency or the rotations per second of the vortex. Additionally, the inner diameter of the cylinder is

$$D_{in} = 0.36047 \text{ m}. \tag{2.67}$$

The maximum angular velocity that is reached with the designed inlet equals

$$\omega = f_v \cdot 2 \cdot \pi = 28.274 \text{ rad/s}. \tag{2.68}$$

This parameter is required later. To determine a realistic Reynolds number for the cylinder, an equation for a stirred vessel from [30] is used.

$$Re_{vessel} = \frac{D_{in}^2 f_v \rho}{\mu} = 583731 \tag{2.69}$$

Additionally, the Reynolds number for a rotating disc [31] in a fluid is calculated as follows

$$Re_{disc} = \frac{\omega \, D_{in}^2 \, \rho}{2\mu} = 1.83385 \cdot 10^6. \tag{2.70}$$

This is a different scenario, but it shows that the Reynolds number is large and increases in a quadratic manner with the diameter of the disc.
These large Reynolds numbers indicate that the flow inside the cylinder is turbulent. In [32] it is stated that the rotating disc becomes fully turbulent at $Re_{disc} = 4.6 \cdot 10^5$.

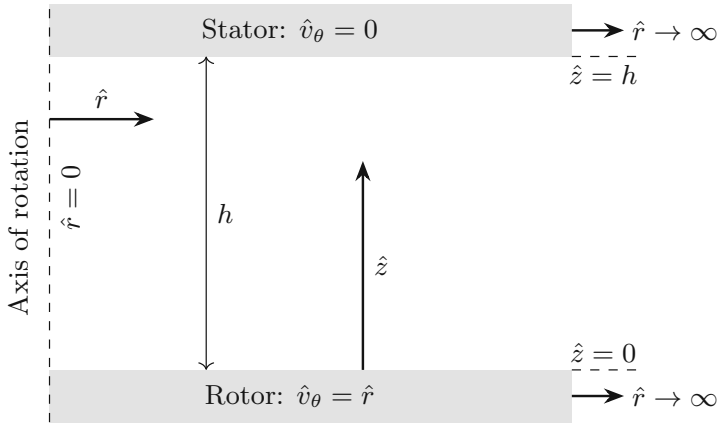

Figure 2.11: Drawing of the arrangement regarding the two infinite disks for the Bödewadt boundary layer [33]. The bottom disk rotates and the top is stationary.

To estimate the boundary layer height, the Bödewadt boundary layer thickness for a stationary disc that has a rotating disc below is calculated. In Figure 2.11 the schematic drawing for this scenario is shown. The boundary layer develops on the non-rotating stator $\hat{v}_\theta = 0$ and the spinning rotor that are separated by the distance h. Table 2.3 contains the description of all relevant parameters. According to [33], the Reynolds number equals

$$Re_{bw} = \frac{\omega h^2}{\nu} = 101584 \tag{2.71}$$

and the boundary layer for the stationary disc is

$$\delta_{bw} = \frac{4.9025}{\sqrt{Re_{bw}}} = 15.382 \text{ mm}. \tag{2.72}$$

This is an approximation, as the discs have an infinite diameter and there are no side walls. Note that this result is only valid for the maximum rotational frequency f_v.

Parameter	**Description**
h	Distance between the two disks
$\hat{r}$	Radial coordinate
$\hat{z}$	Vertical axial coordinate
$\hat{v}_\theta$	Angular velocity

Table 2.3: Parameters in Figure 2.11.

Frequency (Hz)	Angular velocity (rad/s)	Reynolds number	**Boundary layer height (mm)**
0.2	1.2566	4514.86	72.96
0.4	2.5133	9029.73	51.59
0.6	3.7700	13544.59	42.12
0.8	5.0265	18059.45	36.48
1.0	6.2832	22574.32	32.63
1.2	7.5398	27089.18	29.79
1.4	8.7965	31604.05	27.58

Table 2.4: Boundary layer thickness at low angular velocities.

In Table 2.4, the boundary for low angular velocities is shown. At an angular velocity of 3.77 rad/s the boundary layer height is still 42.12 mm and goes down to 27.58 mm for 8.7965 rad/s. Clearly, the boundary layer is significantly thicker at lower velocities.
On the basis of these calculations, the height of the cylinder is chosen to be at least 60 mm to ensure that a vortex can be created. Making the cylinder even higher would further reduce the effect of the boundary layer on the vortex. Besides, more material and time is required to manufacture a larger cylinder.
As mentioned in [32], the composition of the flow between a rotating and stationary disc is very sophisticated. So, in the cylinder a three dimensional boundary layer develops with the corresponding velocity profile that would require additional equipment to be measured.

The final cylinder design has an outer diameter of 420 mm and an inner diameter of 360.47 mm. The inner height of the cylinder is 60 mm, which should sufficiently reduce the effect of the boundary layer. Including the water tank the system contains a water volume of approximately 8 liters.

2.3 Printing a Watertight Cylinder

This section focuses on the flat gasket for the two cylinder lids and the printing process. Additionally, measures to improve the watertightness of the setup are discussed.

2.3.1 Flat Gasket for the Lid

Clearly, the setup should be watertight. Additionally, the two lids should be transparent and removable so that the inside of the cylinder is accessible and modifiable. This way the velocity sensor, which will be discussed in later chapters, can be easily installed or removed. Therefore, a solution that glues the lids to the printed cylindrical ring or makes their removal cumbersome is not desired.
To prevent water leaks between the cylinder and the two lids a flat gasket made out of silicone sealant is used. Because the surface of the printed material is rather rough, the gasket is molded directly onto the cylinder. To create a flat gasket, the lid is pressed down on the soft silicone. With the silicone in the right shape, the setup dries for about one week. After everything is dry, the lid is removed. The resulting gasket is 2 mm thick and covers the bottom and top side of the cylinder.
Another key aspect is the evenness of the gasket and the surfaces that are in contact with the silicone. Any seal or gasket that does not have an even surface is unsuitable. The same is true for the contact surfaces. With an uneven surface more pressure has to be applied to the seal, to make it watertight. This can lead to its destruction. Furthermore, the water pressure forces on one side of the gasket increase with a larger surface area. For this reason, the gasket is not thicker than 2 mm.
Another important design aspect is the stiffness of the lid and the applied pressure on the flat gasket via the bolts. This pressure is applied via the threaded bolts. When the number of bolts is insufficient and the lid too compliant leakage can occur in the areas between two bolts. These are the areas with the lowest pressure on the seal that is caused by local deformation of the acrylic. This implies that the lid should be stiff to minimize its local deformations. Generally, increased force applied by the screws on the gasket reduces leakage [34]. For these reasons, two 25 mm metal washers are used for each bolt to spread the forces exerted by the screws more evenly. Under the metal washers, a 3 mm thick PLA washer helps to protect the lid.
Besides, insolubility in water for all used materials is essential. This important criterion is fulfilled, also by the additional layer of Vaseline (petroleum jelly) that the silicone is coated with, which acts as an extra sealant [22].
The silicone sealant has a 20 ± 5 A shore hardness and is suited for temperatures from -50°C to +120°C, as written on the packaging. The temperatures in the considered water circuit are well within this operating range of the silicone.

2.3.2 Watertightness and Printing

The printed cylindrical ring requires additional treatment before it can be used in the water circuit for longer periods of time.
Compared to printed parts for dry applications, a few things have to be adjusted. First of all, one or two perimeters are not enough for designs that are part of a pressurized water circuit. Perimeters are the lines that the printer prints for the outer contour, which in the case of the cylinder is the inner and outer wall, for example. A higher number of perimeters results in thicker printed walls. This means, that 2 perimeters yield a wall that is 0.80 mm thick and 5 perimeters a wall that is 2.00 mm wide, if a 0.4 mm nozzle is used. Clearly, this makes a difference and for this reason the design has 5 perimeters. This is of particular importance for the inner wall, which is in contact with the water.
Another crucial printing parameter is the infill. Figure 2.12 shows the difference between having two or five perimeters inside the cylinder with the same infill. This implies that an increased infill does not increase the thickness of the walls of the cylinder. Only an increased number of perimeters does widen the walls. Instead, the inner structure of the printed volumes becomes denser when infill is raised. Printing time goes up with both the number of perimeters and the infill.

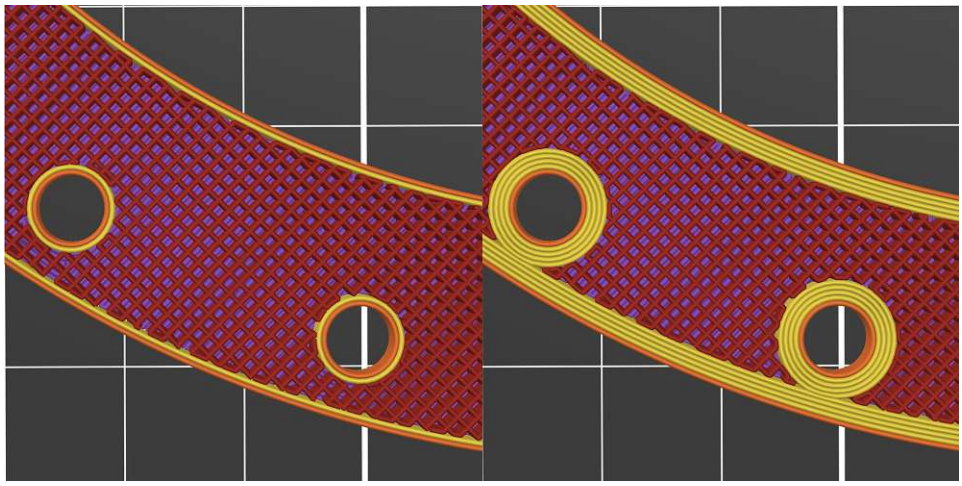

Figure 2.12: Left image with two perimeters and right with five, created in PrusaSlicer.

The printed cylindrical ring for the test stand has an infill of 20%. The layer height of the printed structure is 0.20 mm. Generally, high infills are not necessary for printed surfaces that are in contact with water but rather a high number of perimeters [35].
Multiple perimeters are not enough for operating the test stand with water for lengthy time periods because the printing material PLA absorbs water. Consequently, additional measures are necessary, like another material to coat the surfaces that are in contact with water. Before applying this layer, the surface is cleaned with alcohol and acetone.
Generally, there are different possible coating materials for making printed surfaces watertight. One material that proves to be convenient, is candle wax. Its application is straightforward. The wax can be heated up with a hot air gun and spread over the

surface. Candle wax has a low melting point and is insoluble in water. With the water in the test rig reaching only room temperature, the low melting point is acceptable.
3D printers that work with the Fused Deposition Modeling (FDM) principle use thermoplastics to print. These plastics have to be heated up for the printing process and once extruded they cool down. This results in temperature gradients in the object, which can lead to tension and warping of the printed object [35]. Essentially, the mechanical properties depend on the vertical position due to the temperature differences. Especially sharp corners are problematic in this regard. Due to this problem, the object can bend (similar in shape to a banana).
To counteract this issue, heated beds are utilized. This way, the material can be heated from below. Sharp edges and corners should be avoided if possible. These measures help mitigate the problem of warping. Therefore, the cylinder is also manufactured with a heated bed and due to its round shape there are no sharp corners at the bottom. In addition to this, glue stick is employed to improve adhesion at the bottom layer and the printing bed.
The thermoplastic PLA is a convenient printing material as the melting point is not that high. PLA has a slightly higher coefficient of thermal expansion than Acrylonitrile Butadiene Styrene (ABS) but lower than Polyethylene Terephthalate type G (PET G) [36].
Standard printers are utilized to manufacture all parts. The cylinder and other larger objects were printed with an Anycubic Kobra 2 Max. For smaller parts, the Prusa MK4 was used.

2.4 Water Tank

Another component of the water circuit is the water tank shown in Figure 2.7. Its main purpose is to add water and fill up the cylinder. Additionally, air that is inside the cylinder can be removed via this tank by tilting the cylinder in such a way that its outlet is at the top. The water tank is also printed with PLA and its surfaces with water contact are smoothed with acetone. Following this step, the inner wall along with the hose barb fittings is coated with candle wax. The volume of this component is 2.23 liters when completely filled up.

2.5 Final Setup

This section describes the hardware, software and mechanical components of the test stand. Sensors and actuators are described in the next chapter.

2.5.1 Hardware

To run the system in real time, the MicroLabBox from dSPACE is utilized. This device runs the software and interfaces with the physical devices. All signals that are coming from the sensors are first sent to isolation amplifiers, to ensure that the MicroLabBox

is not damaged by high currents or voltages. Specifically, DC-isolation amplifiers from Knick of the type P 27000 H1 are used.

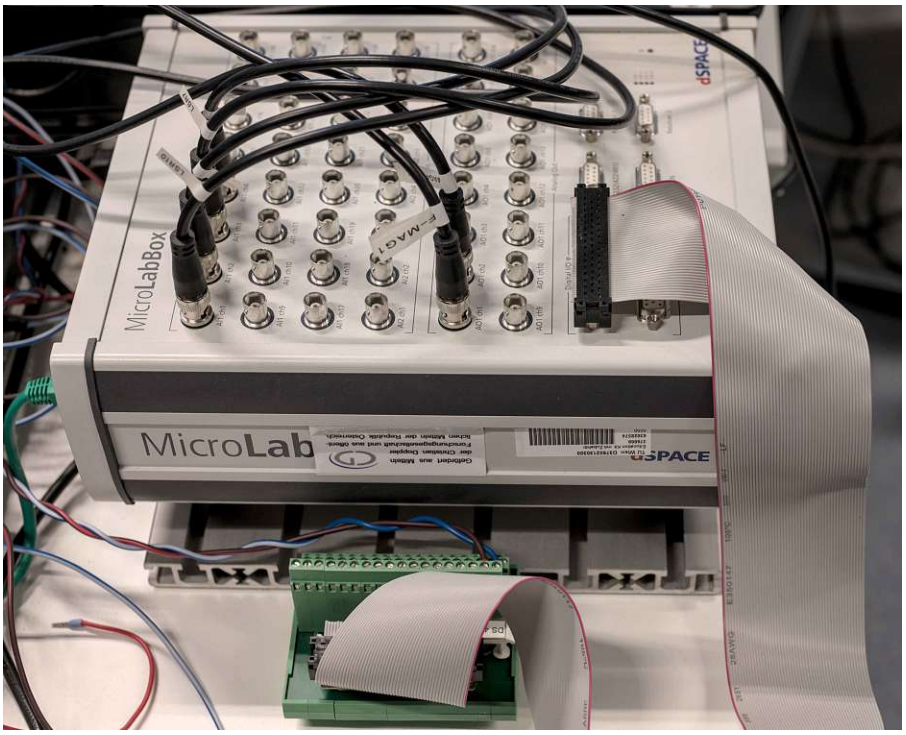

Figure 2.13: Dspace MicroLabBox with connected analog inputs and outputs. The only digital input, which is the hall sensor for measuring flow rate, is also connected.

Additionally, the capability of handling a large number of analog inputs, digital inputs, analog outputs and digital outputs makes the MicroLabBox suited for the task. Moreover, the relevant code is written in Simulink and the compiled version can run on the dSPACE device, which is briefly discussed in the following section. Figure 2.13 shows the MicroLabBox with the four connected analog inputs from the velocity sensors on the very left. The two analog outputs for the motor driver are in the middle and to the right is the digital input from the hall sensor, connected with a 50 pin D-subminiature connector. All of these devices are explained in Chapter 3.
The pump is controlled and powered with an ESCON 50/5 servo controller motor driver from maxon motor ag. In the next chapter, this is discussed in more detail.

2.5.2 Software

The entire control architecture is programmed in the Simulink environment, which is part of Matlab. Next, the compiled code is transferred to the MicroLabBox. With the software ControlDesk, the PC communicates with the MicroLabBox. For instance, all values such as setpoints for controllers can be adjusted or sensor voltages observed.

2.5.3 Power Supply

To supply the different electrical components of the test stand, a programmable power supply HMP4040 from ROHDE & SCHWARZ HAMEG is used. With four channels, all sensors and the actuator can be supplied. Moreover, the current can be limited and the power drawn from the different devices can be seen on the display.

2.5.4 Cylinder and Other Components

As already mentioned, the cylinder is made of PLA with a 0.2 mm layer height, 5 perimeters and 20% infill. The inner diameter is 360.47 mm and the outer 420 mm. A 2 mm thick layer of silicone lies between the 15 mm thick lids and the cylinder. All of this is held together with 42 galvanized M6 bolts. Considering all components, the circuit in Figure 2.14 has a volume of roughly 8 liters, with the water tank.
Some other components of the test stand are also printed with PLA, for example, the water tank and the sensor housing. Hoses, acrylic lids and hose clamps are standard components that were purchased.

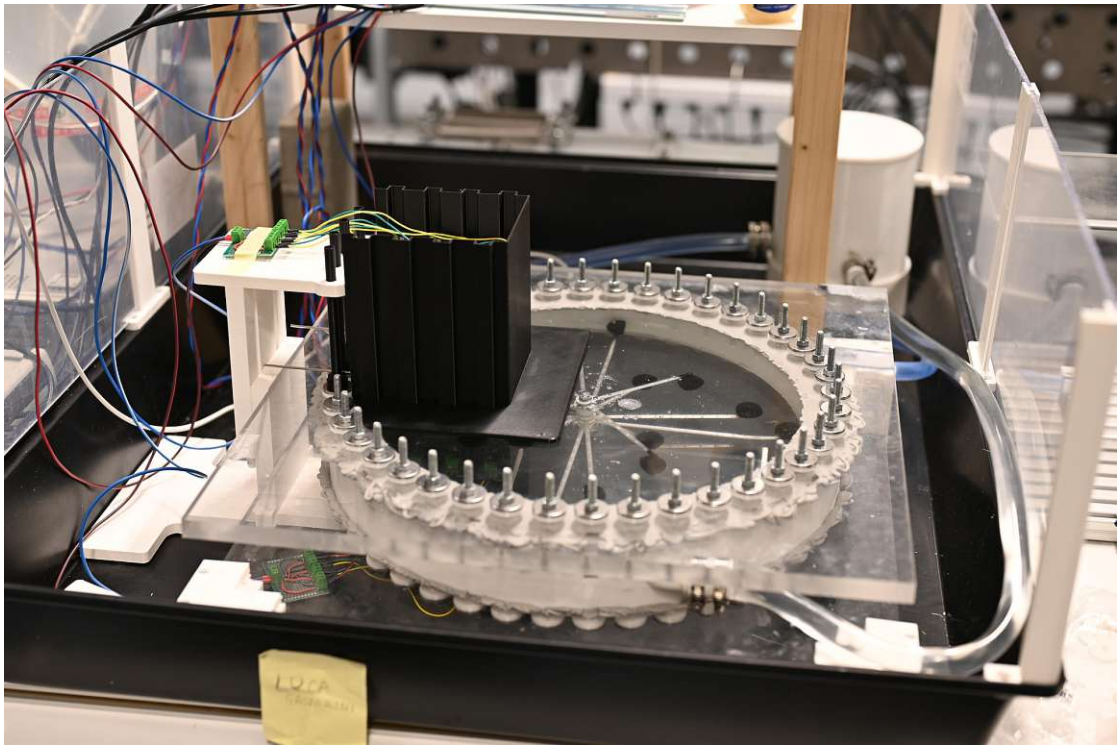

Figure 2.14: Final setup filled up with water, with the light sensor on the side. The black paddles (hemispherical-cups) in the cylinder are responsible for velocity measurements. The water tank, hall sensor and pump are behind the cylinder. To protect the surrounding equipment against water, acrylic sheets are mounted on the sides.

2.5.5 Sensors and Actuator

For measuring the velocity of the vortex at four points along the radius, a device is developed. This device consists of pivoted paddles and light barriers, which detect the movement of the paddles. Figure 2.14 depicts the finished setup with this instrument and in the following chapter this entire sensor is discussed in detail.
The gear pump is the only actuator of the entire system. This is a positive displacement pump, meaning that a specific amount of volume is pumped per revolution [26]. With this device, the vortex is created and driven by pumping the water tangentially into the cylinder.

3 Sensors and Actuators

In order to measure the velocity of the water vortex, a sensor is developed. It measures at four points along the radius. As the lid is transparent and also the liquid, a light barrier that measures intensity changes is feasible. These changes in illumination are caused by paddles that move with the vortex, similar to a wind anemometer. In this chapter, first the fluid velocity sensor is elaborated in detail. Also the hall sensor, which measures the fluid flow is outlined. Finally the gear pump is described.

3.1 Sensors for Detecting the Vortex Velocities

This section focuses on the sensors that measure the velocity of the vortex. Figure 3.1 shows the final version with all relevant components labeled. Figure 3.2 shows the sensor without the paddles. Each light barrier measures one velocity in the vortex with the help of printed paddles (hemispherical-cups) that rotate with the vortex.

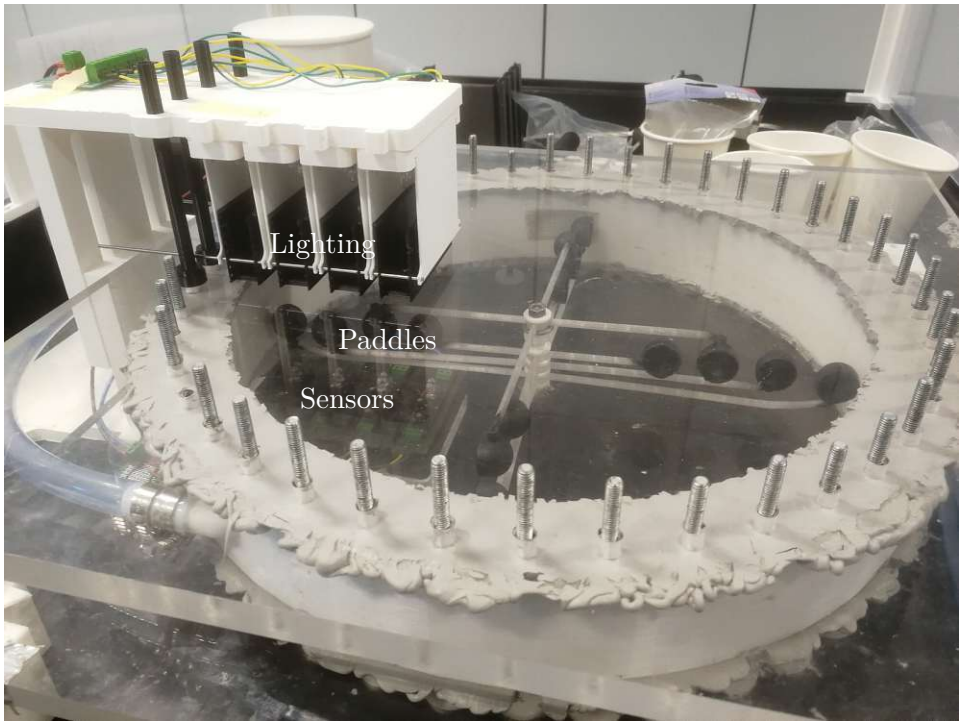

Figure 3.1: Complete velocity sensor with the light barrier and paddles.

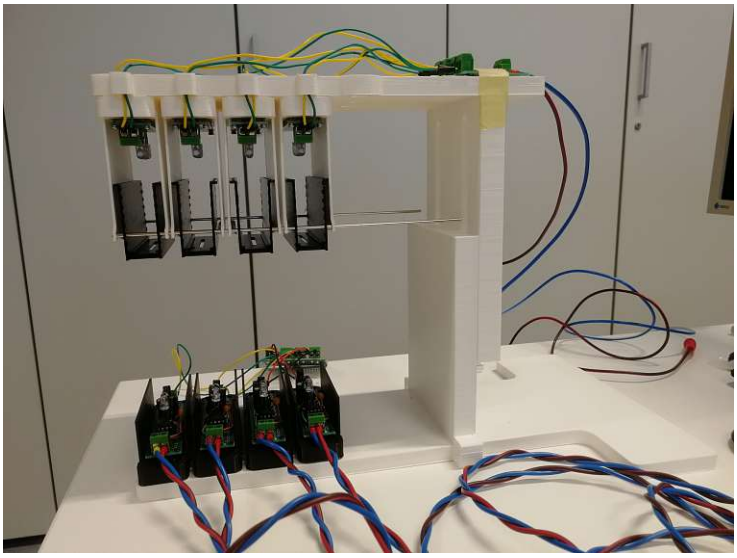

Figure 3.2: Velocity sensors consisting of the four light barriers.

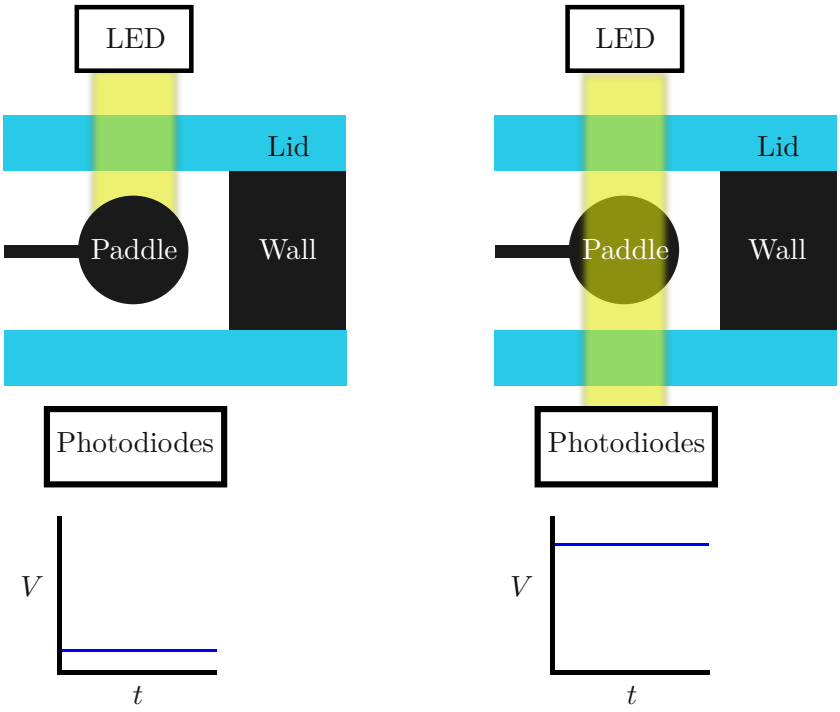

Figure 3.3: Working principle of the light barrier with the cylinder, the side wall, the two lids, and one paddle depicted in the figure. In the left image, light is being blocked by the paddle and in the right image not. Below are the corresponding different voltage levels of the transimpedance amplifier.

3.1.1 Working Principle of the Sensor

Generally, the fluid flow in water is invisible. The goal of this work is to control and model a water vortex inside the cylinder. Therefore, a sensor is necessary for closed-loop control. For that reason, pivoted paddles that work similarly to an anemometer rotate with the vortex. Four sensors measure the velocity at different points along the radius.
A central question is how the fluid flow in the vortex can be converted into an electrical signal that can also be measured. One option is a light barrier, which detects a change of the light intensity. This variation is caused by an object moving through this barrier. Specifically, the paddle that rotates with the vortex briefly blocks the light. Below a photodiode can detect this change in illumination and with the help from a transimpedance amplifier the small current from the diode is converted into a voltage, which is measured at the output [37]. Figure 3.3 shows this principle. The light source in Figure 3.3 consists of Light-Emitting Diodes (LEDs) that are placed above the circuit.
Additionally, there are a total of four connected paddles for each measurement point along the radius, see Figure 3.1. These rotate about the axis in the center of the cylinder. In total there are 16 paddles for all four measurement points.

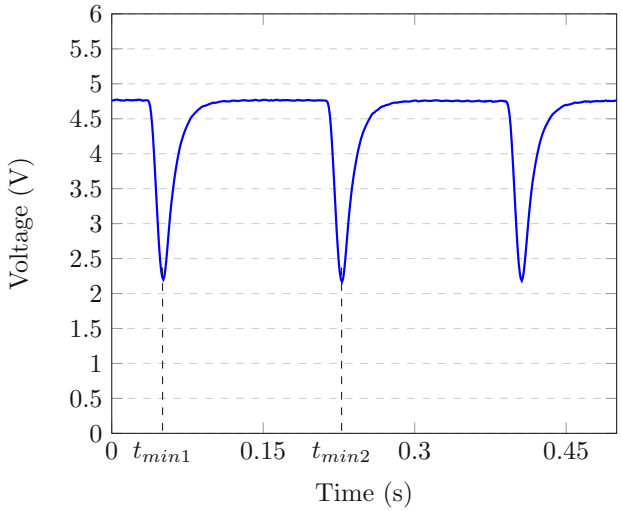

Figure 3.4: Graph with time between two minima clearly labeled.

The paddles that rotate with the vortex produce a changing voltage at the photodiodes. This specifically means that voltage drops when the light is blocked by the paddle and then rises again to the standard level, indicating that no objects interfere with the light. Clearly, an electrical signal with minima will result from this system as can be seen in Figure 3.4 and 3.5. Once the first two minima are detected, the time between them can be measured. So, as the distance between two paddles of the same radius is known, the velocity equals

$$v_{vortex} = \frac{d_{cup}}{t_{min2} - t_{min1}} = \frac{d_{cup}}{\Delta t}. \tag{3.1}$$

Figure 3.4 clearly shows two minima at t_{min1} and t_{min2} that can be used for this calculation.

With this simple equation, the velocities for the other paddles can also be determined. This specific graph in Figure 3.4 is the result of a test run with compressed air.

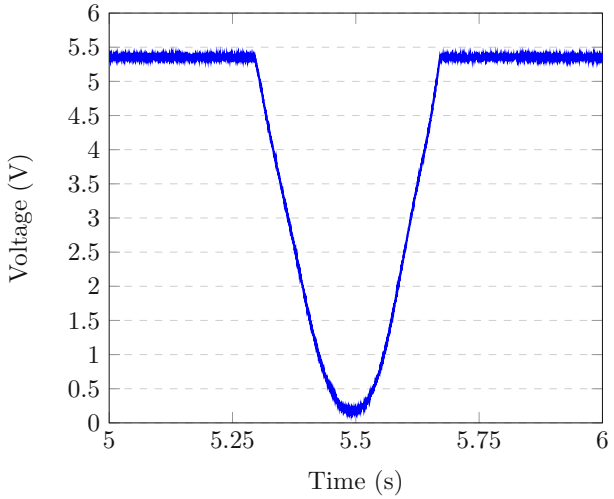

Figure 3.5: Voltage over time of the light barrier at a very low velocity. The single voltage drop caused by the paddle is clearly visible.

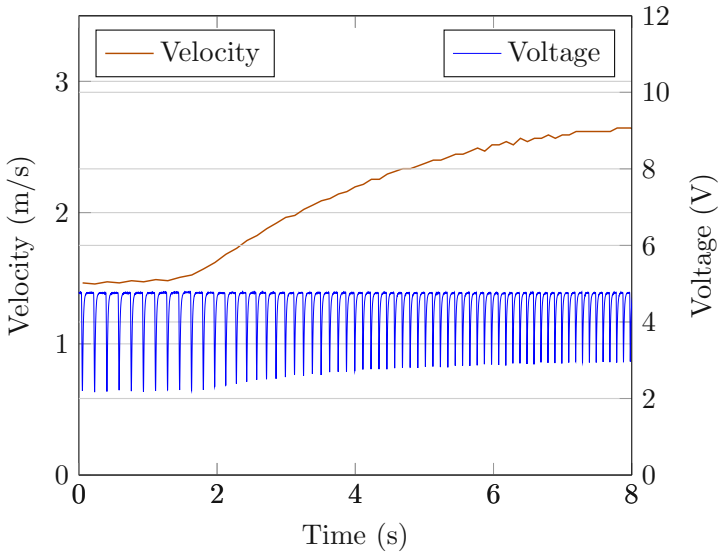

Figure 3.6: Voltage over time of the light barrier at higher speeds.

The signal in Figure 3.6 is the result of the paddles moving much faster than in Figure 3.5. In Figure 3.6, it can be seen that the voltage drop reduces and the frequency increases as the velocity goes up. Therefore, less time remains for the rotating paddle to block the light. Moreover, for testing purposes the velocity sensor was operated with compressed air in Figure 3.6, which is the reason for the relatively high velocity.

The paddles are placed as far away from the center as possible where the water velocity is the highest. This is because near the center the water moves very slowly and this would not yield any valuable information. In the Subsection 3.1.3, the paddles (hemispherical-cups) are elaborated in more detail.
Moreover, the paddles average the velocity over the area of the cup. The friction in the bearings at the center of the shaft add additional resistance. Also the shafts of the paddles interfere with the water flow. Therefore, this sensor does not measure the exact velocity of the water flow, but a lower velocity.

3.1.2 Sensor Housing

To ensure that the light barrier sensor is not disturbed by environmental light, a housing is developed. The photodiode circuit is attached to a small movable platform, in order to adjust its position. Moreover, each LED light strip is adjustable in the same way. Additionally, the vertical distance between the lights and sensor circuit can be changed with M8 screws that are attached on the side of the sensor housing. The areas labeled with red circles in Figure 3.7 show where M8 nuts are placed in the labeled lower part and the M8 screws in the top part. The labeled grooves are slightly wider than the bolts, allowing for free movement of the two components in the vertical direction. Hence, the vertical position can be adjusted and the M8 threaded bolts hold the two parts together.

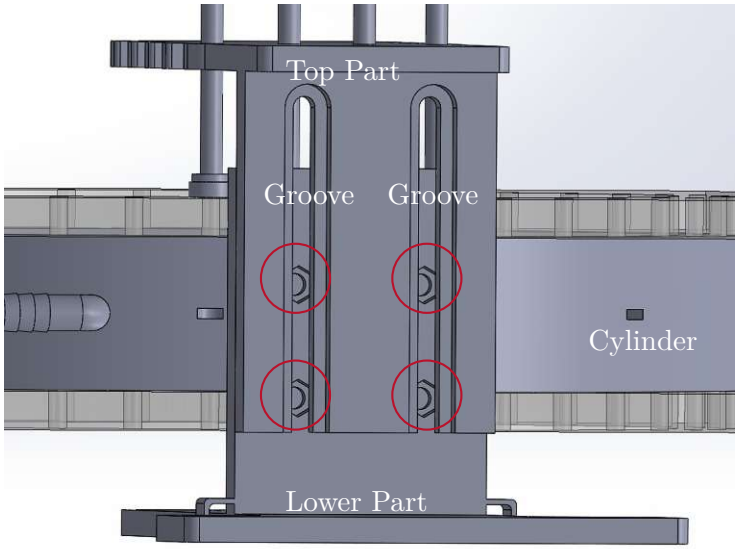

Figure 3.7: Velocity sensor housing from the side showing the position of the screws for adjusting the height.

3.1.3 Paddles for Flow Velocity Measurements

The paddles are hemispherical-cups with an outer diameter of 22 mm. The four paddles are placed 31 mm from each other (along the radial direction) and at a height of 30 mm

above the bottom lid. There are four paddles for every radius as shown in Figure 3.8, as the measurement accuracy and robustness increase with four paddles for one radius. This is due to the fact that torque increases and bearing friction remains unchanged when more paddles are used. The entire paddle structure, including the arms, is printed with transparent PLA and the paddles are painted black. These measures are necessary to ensure as few false signals as possible, which could be created by the shafts of the paddles at the three inner sensors.
Figure 3.8 shows the entire mechanical setup with arms and paddles. To hold the sensor arrangement in place, an M6 bolt that is glued to the bottom lid serves as a central axle. The arms of the paddles are partially hollow, with additional support structures inside, to reduce their weight. With a diameter of 4 mm, the arms provide enough stiffness. In Figure 3.9 the design of the arm is shown.

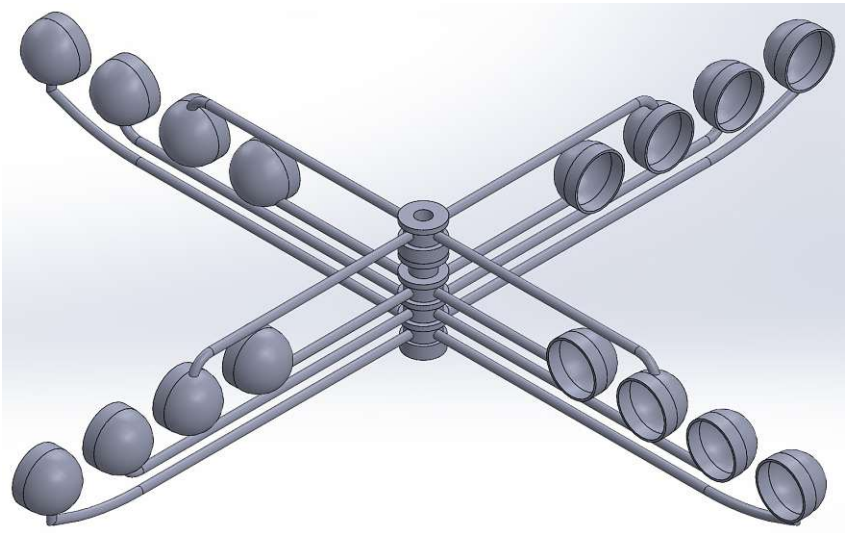

Figure 3.8: The four paddles for each radius with the shaft and bearings in the center.

Figure 3.9: Sectional view of an arm and a paddle. The arm has a partially hollow structure.

Table 3.1 contains the locations of the paddles along the radius of the cylinder. The distance from one paddle to the next, measured from the center, is always 31 mm. All paddles are located at the same height of 30 mm.

Parameter	Position in radial direction from center (m)
First paddle R_{pad1}	0.165
Second paddle R_{pad2}	0.134
Third paddle R_{pad3}	0.103
Fourth paddle R_{pad4}	0.072

Table 3.1: Position of the four paddles (hemispherical-cups) along the radius.

3.1.4 Circuit Design for Transimpedance Amplifier

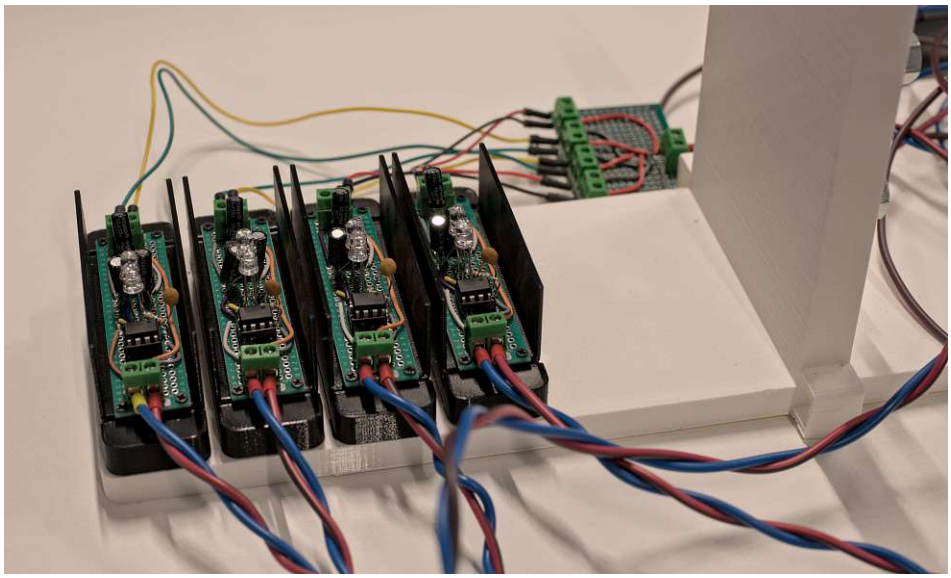

Figure 3.10: Four transimpedance amplifier circuits, each with two photodiodes and one operational amplifier. The thin side walls reduce unwanted light.

The idea behind a transimpedance amplifier, shown in Figure 3.10, for this specific case is to convert a changing optical signal into a voltage that can be measured [37]. In this work, the transimpedance amplifier is designed according to a technical document for such devices from Texas Instruments [38]. All equations in this subsection are taken from this guide.
For the transimpedance amplifier circuit, illustrated in Figure 3.11, a TL071CP JFET-input operational amplifier is used. This amplifier has a low input bias current and less noise than other devices of this type. These characteristics are crucial when very low currents are to be amplified. For an illuminance of 1000 lx with standard illuminant A and a rverse voltage of 5 V, a current in the range of 50 μA coming from the photodiode is amplified and turned into a voltage [39]. This voltage V_{OUT} can be easily measured, which is not the case for the small current generated by the photodiode. The TL071CP

has to be operated with a dual-supply, which is standard for operational amplifiers. In Figure 3.12 this supply configuration is depicted.

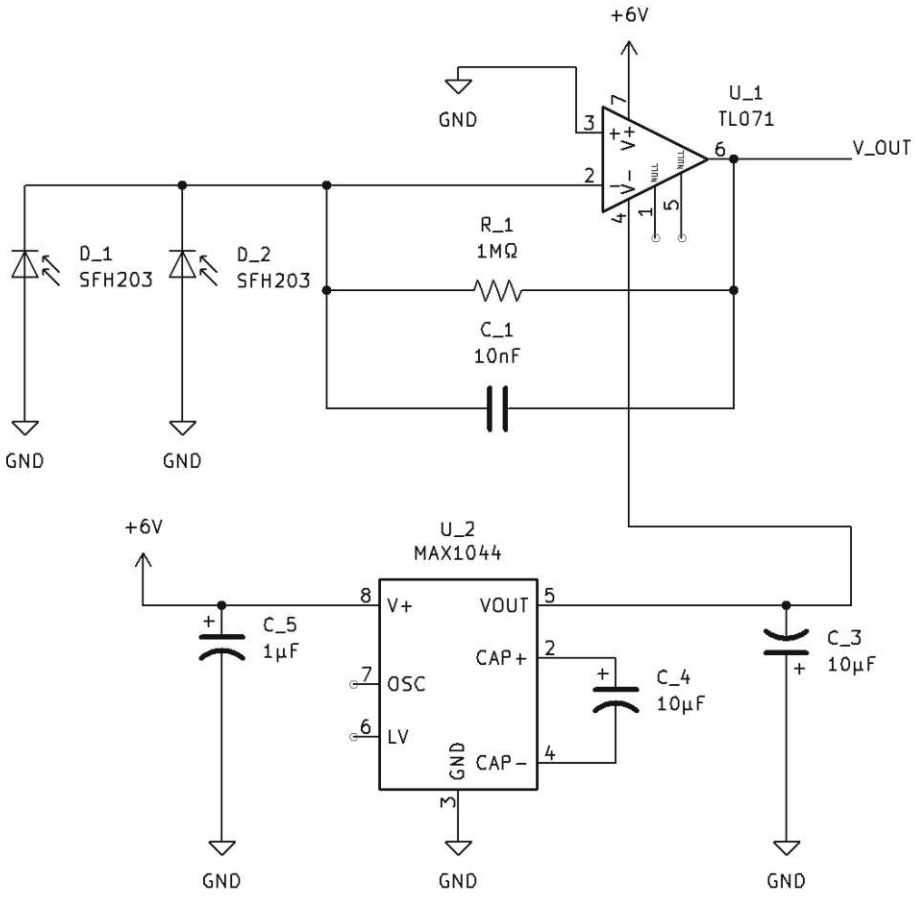

Figure 3.11: Transimpedance amplifier circuit to amplify small currents coming from the two photodiodes. The MAX1044 switched-capacitor voltage converter that inverts the supply voltage for the TL071 is also shown.

Similar operational amplifiers, such as the TL031CP, have a smaller input bias current but a smaller slew rate [40]. Therefore, the TL071CP, having a maximum input bias current of 7 nA and a minimum slew rate of 8 V/μs [41], offers a good trade-off.
The chosen maximum output voltage for the TL071CP is

$$V_{OUTmax} = 5 \text{ V} \tag{3.2}$$

and the minimum output voltage equals

$$V_{OUTmin} = 0 \text{ V}. \tag{3.3}$$

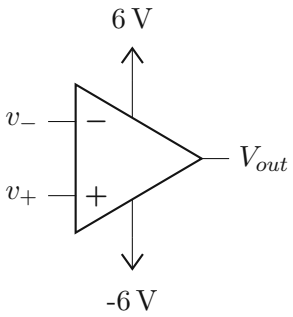

Figure 3.12: Operational amplifier with dual-supply configuration.

With the ±6 V power supply, the operational amplifier can amplify up to slightly more than 5 V before saturating. The resistor responsible for amplification equals

$$R_1 = 1 \text{ M}\Omega. \tag{3.4}$$

For R_1 a large value is selected to ensure that small currents are also amplified. Therefore, the required current of the photodiode is

$$I_{phd} = \frac{V_{OUTmax} - V_{OUTmin}}{R_1} = 5 \ \mu\text{A}. \tag{3.5}$$

The photodiode can generate larger currents than I_{phd} [39] and therefore, the signal can be amplified with this circuit. When both photodiodes are well illuminated, the output current is even higher, which implies that the amplifier will saturate. This behavior is intentional. The sensor should actually have a high output voltage also when one photodiode is illuminated and the other one is blocked by an arm from another paddle. This way, the arms of the paddles cannot create a significant voltage drop, as the photosensitive area is greater. Moreover, the pleasant side effect of this specific circuit are the clear minima, as the two photodiodes are almost as wide as a paddle.
The assumed maximum velocity of the vortex is

$$v_{max} = 2 \text{ m/s}. \tag{3.6}$$

The distance between two outermost paddles at the radius R_{pad1} is

$$d_{pad1} = \frac{2\pi R_{pad1}}{4} = 0.2592 \text{ m}. \tag{3.7}$$

This yields a frequency of

$$f_{max} = \frac{v_{max}}{d_{pad1}} = 7.72 \text{ Hz}. \tag{3.8}$$

During operation a maximum speed of around

$$v_{act} = 0.79 \text{ m/s} \tag{3.9}$$

was observed at the outermost paddle. This gives a frequency of

$$f_{act} = \frac{v_{act}}{d_{cup1}} = 3.05 \text{ Hz}. \tag{3.10}$$

Generally, the circuit also works at velocities above 2 m/s although at these speeds the voltage drop is less significant. The selected circuit bandwidth is

$$f_{band} = 16.5 \text{ Hz}. \tag{3.11}$$

With this information, the corresponding capacitor equals

$$C_1 = \frac{1}{2\pi R_1 f_{band}} = 9.65 \text{ nF} \approx 10 \text{ nF}. \tag{3.12}$$

This selected capacitor yields the cutoff frequency [42]

$$f_{cut} = \frac{1}{2\pi R_1 C_1} = 15.92 \text{ Hz}. \tag{3.13}$$

Parasitic capacitances such as the common-mode input capacitance and differential input cpapcitance are neglected, as the values are in the picofarad range [41].
According to the TL071CP data sheet [41], the gain bandwidth of this operational amplifier is 5.25 MHz, which is more than necessary for this sensor.
The designed circuit works very well. Even though two photodiodes are never exactly identical, there are no problems during operation with equalizing currents flowing between these two parallel diodes or at least they are very small.

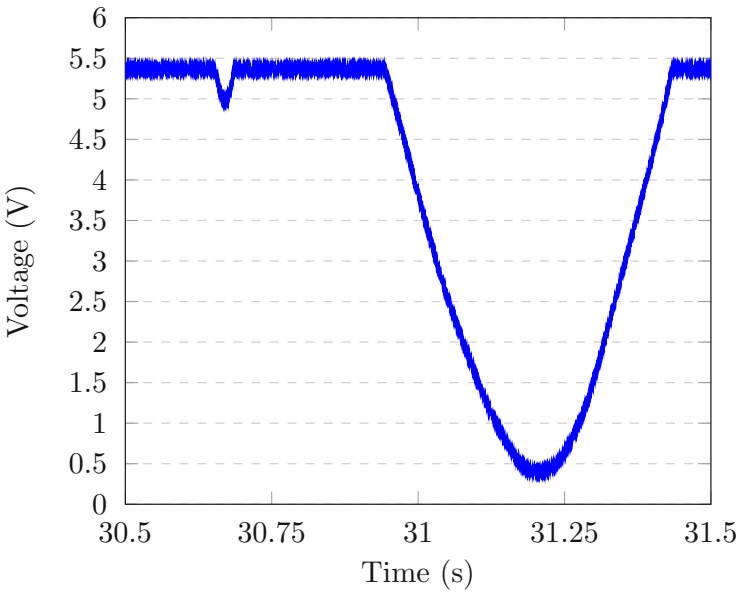

Figure 3.13: Voltage over time of the light barrier for the innermost paddle at a flow rate of 4 L/min.

The arms of other paddles only cause a minimal voltage drop and the interference with the signal is not problematic. In Figure 3.13, a small drop caused by another arm is shown for

the innermost paddle measured at a flow rate of 4 L/min. The high amplification causes the amplifier to saturate when nothing blocks the light, depending on the illumination. The sensor works and measures the changes in light intensity brought about by the moving paddles. Additionally, the high-frequency measurement noise shown in Figure 3.13 is reduced with a moving average filter that has a window size of 171.
A switched-capacitor voltage converter is required to supply the operational amplifier with negative voltage relative to ground. For this purpose a MAX1044 is used, which can invert the supply voltage with merely two capacitors [43]. The circuit diagram in Figure 3.11 includes the MAX1044, which is below the operational amplifier.

Figure 3.14: The rectangular aperture mask for creating a strip of light with a 2.5 mm opening.

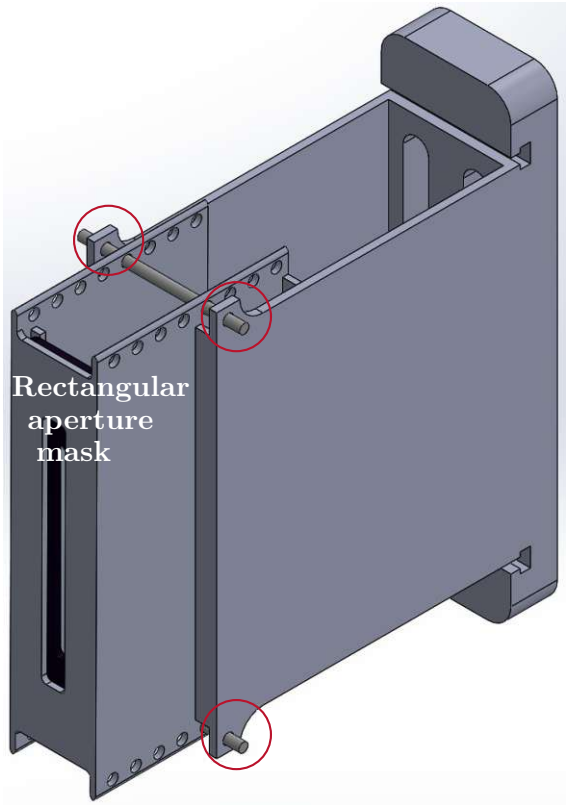

Figure 3.15: The rectangular aperture mask inserted into the front part. Its height can be adjusted with bolts that are inserted in the labeled areas.

3.1.5 LED Lighting for Light Barrier

The aim of the LED lighting is to create a strip of light only shining on one sensor and not interfering with neighboring sensors.
To have a strip of light at the sensor, black PLA parts are printed with a rectangular opening (rectangular aperture mask), see Figure 3.14. The corners of the rectangular contours are curved and the gap is 2.5 mm wide. Figure 3.2 shows the final version with all components assembled. The vertical distance between the black PLA parts and the light sources can be changed with bolts, see Figure 3.15. This adjustment option allows for an optimal strip of light. When correctly adjusted, a narrow light strip is projected on the two photodiodes located below. This is shown in Figure 3.16.

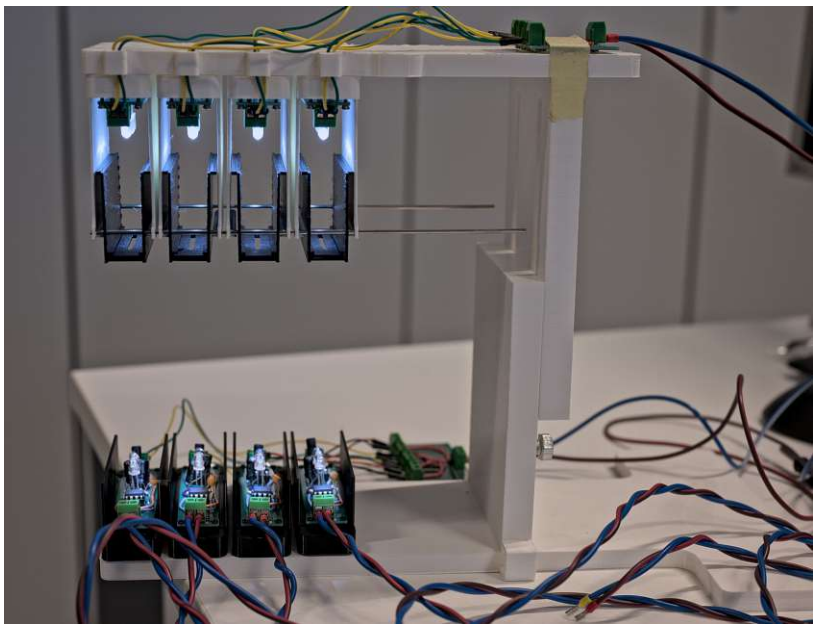

Figure 3.16: Light barrier with lights turned on. Visible are the projected light strips.

For the lighting, LEDs emitting white visible light are used. This type of light works well with the photodiodes. The LEDs are arranged in rows of 6 diodes each. The LEDs are connected in parallel to work at the same voltage, see Figure 3.17.

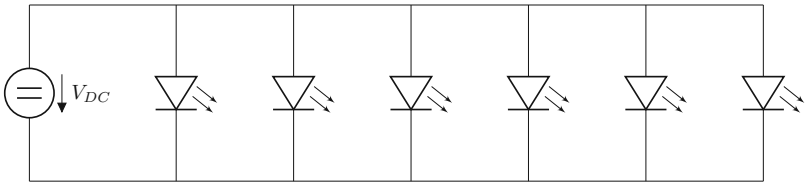

Figure 3.17: The LED lighting circuit.

Choosing the right operating voltage is crucial for the sensor. Higher voltages result in a

more powerful light and lower voltages in a less powerful one. When one paddle passes through the light barrier, a drop of the output voltage V_{OUT} is created. This voltage drop depends on the incident light intensity and the actual speed of the paddle moving through the light barrier. Dimmer light will increase the sensitivity of the sensor, meaning that an output voltage drop may also be observed when an arm passes through the light barrier. For the inner sensors, this effect is more pronounced as they see more arms of the outer paddles.

Figure 3.18: Cover for light barrier against ambient light.

With all of this in mind, a supply voltage of 2.9 V proved to work well for the LEDs.

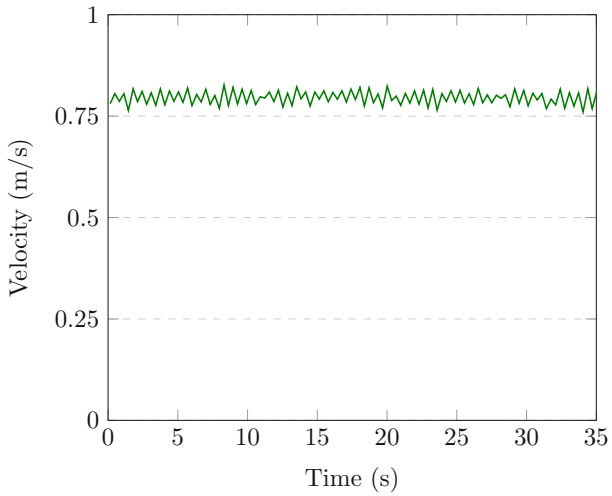

Figure 3.19: Measured velocity at the outermost paddle for a flow rate of 13 L/min.

Figure 3.18 shows the black PLA cover to protect the light barrier from ambient light. This part can be slid over the top part of the sensor and rests on the top lid of the cylinder,

see Figure 2.14. Thanks to this cover, the setup can be operated independently of the lighting conditions. The cover ensures that the photodiodes receive light only from the LEDs above. Otherwise no reliable measurements can be taken, if ambient light shines on the photosensitive area from different directions.
Figure 3.19 shows the measured velocity at the outermost paddle at a flow rate of 13 L/min. The observed measurement noise is acceptable. This is the velocity calculated from the processed raw data and is not calibrated. Chapter 4 looks at the calibration of the measured velocity.

3.2 Hall Sensor for Measuring the Flow Rate

For measuring the flow rate of the pump, an FT-110 flow meter from Gems Sensors is assembled in the circuit right after the outlet of the gear pump. The hall sensor is supplied with 6 V. A 13 kΩ pull-up resistor is connected between the sensor output and the positive supply, as suggested in the data sheet [44]. This is to ensure a default high state, when no water is flowing. In addition to this, the isolation amplifier halves the sensor output signal, which means that 3 V is the maximum output voltage. As the MicroLabBox can only handle voltages up to 5 V at its digital inputs, this is necessary. Below 0.8 V, the signal is interpreted as zero and above this threshold the signal is one [45]. Utilizing the hall effect, the rotational movement of a small turbine wheel in the sensor is converted into a digital signal. This signal is then processed in the MicroLabBox to compute a flow rate. The latter is used for feedback control of the pump.

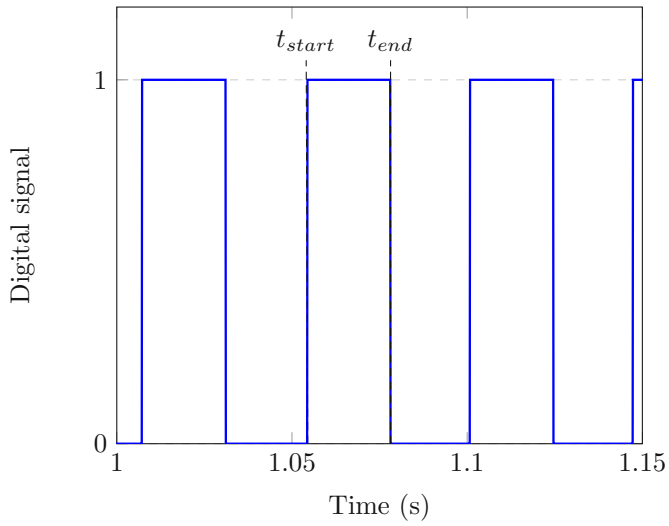

Figure 3.20: Hall sensor signal, after the voltage has been converted into a digital signal.

To calculate the flow rate in real time, half of a period of the signal is detected and the frequency is determined as follows

$$f_{flow} = \frac{1}{2 \cdot (t_{end} - t_{start})} = \frac{1}{2 \cdot T_{half}}. \tag{3.14}$$

The time t_{start} at the beginning of a sequence and t_{end} at the end of a sequence are labeled in Figure 3.20. So, half of a period is the time it takes for a sequence of ones or zeros to end and then for the next sequence to start. The maximum flow rate reached by this pump is

$$Q_{15} = 15 \text{ L/min}. \tag{3.15}$$

This results in a frequency of

$$f_{15} = 251 \text{ Hz} \tag{3.16}$$

according to the data sheet [46]. With these values and assuming a linear behavior of the sensor, the flow rate can be determined in real time as follows

$$Q_{hall} = \frac{f_{flow}}{f_{15}} Q_{15}. \tag{3.17}$$

Generally, one liter generates 1000 pulses [44], which means that a maximum flow rate of 15 L/min generates 15000 pulses or the frequency f_{15}.

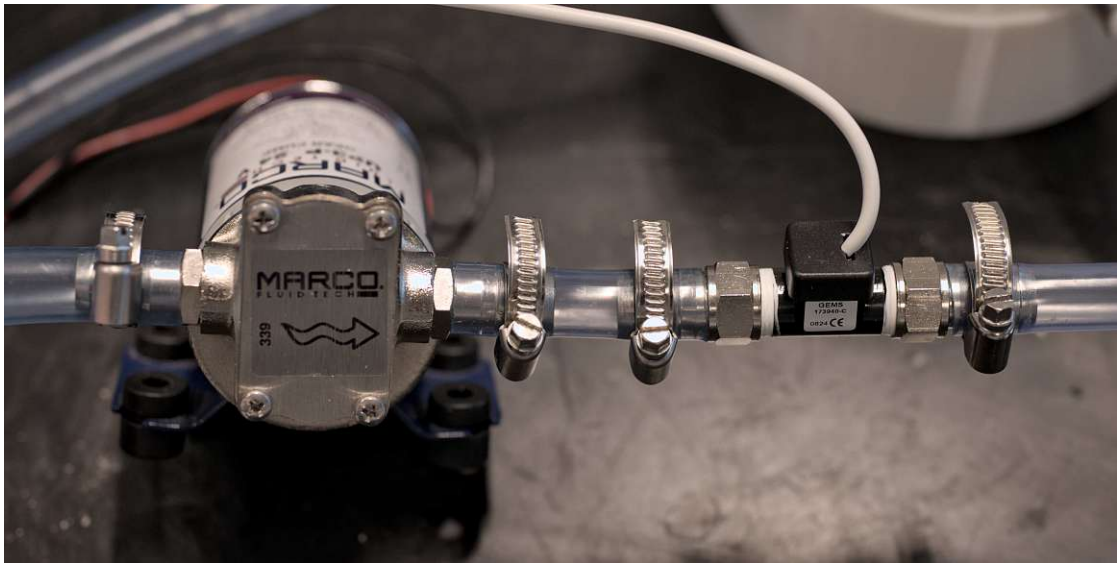

Figure 3.21: Pump and hall sensor.

Additionally, there is some jitter in the sensor output signal and therefore, a moving average of the signal with a window size of six is used. In addition, the sample rate is set to 0.0001 s, which also mediates the problem regarding jitter.
Figure 3.21 shows the pump and the hall sensor assembled in the test stand. All hoses are attached with hose clamps and the sensor is placed right after the outlet of the pump.

3.3 Actuator

To generate the water flow, a UP3-P gear pump from MARCO pumps is utilized. This is a DC motor with a gear pump attached to it. This is the only actuator in the test setup. The maximum flow rate of 15 L/min is reached at 24 V and a 5 A fuse is to be used. However, the maximum current is limited by the power supply to less than 5 A [24]. During normal operation, such high currents are not reached.
Pressure can build up as a consequence of resistances in the water circuit [20]. This reduces the flow rate through the circuit. For example, a small outlet can lead to a large pressure buildup inside the cylinder. In the case of this setup, at near 24 V, the pump is generating a flow rate of 13 L/min, which is less than the nominal flow rate of 15 L/min. This shows that there are measurable losses.

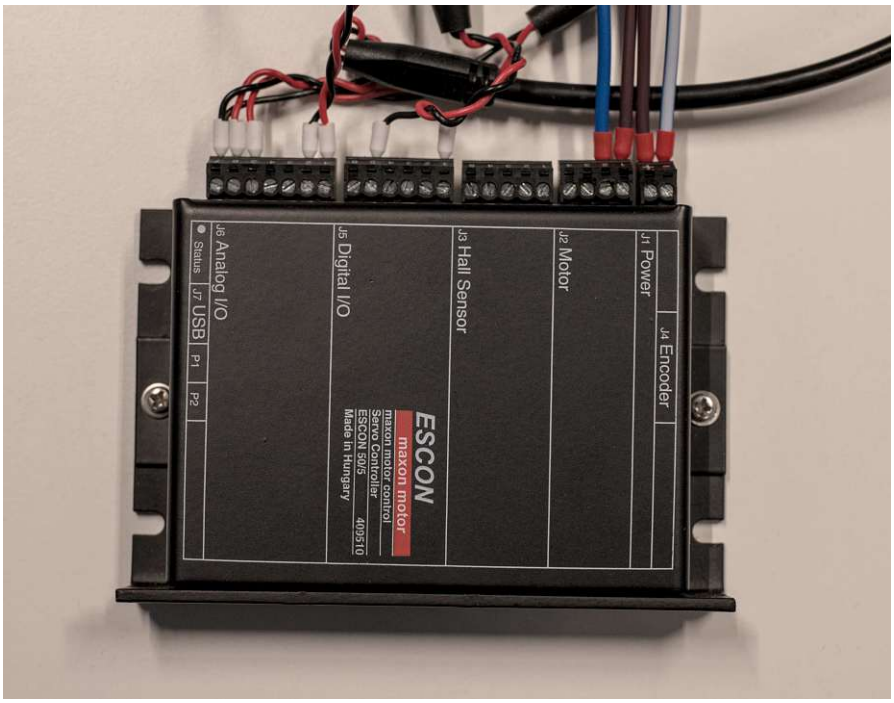

Figure 3.22: ESCON motor driver for the gear pump.

The DC motor of the pump is supplied by a motor driver. This device contains power electronics that can handle the required large currents and voltages and can also work with signals from the MicroLabBox. So, this device is an interface between the pump and the MicroLabBox. For the test stand, the ESCON 50/5 servo controller, from maxon motor ag, powers and controls the pump. With a maximum output voltage of 50 V and 5 A continuously available current, this driver is perfectly suited for this application [47]. In Figure 3.22, this device with the connected wires is shown.
For operation, the motor driver needs a digital enable signal, which is a constant 3 V DC signal coming from the MicroLabBox. To alter the voltage supplied to the gear pump motor, an analog input at the motor driver is available. This is connected to the

MicroLabBox, which sends a voltage signal ranging from 0 V to 9 V to the motor driver. This signal is amplified from 0 V up to 24 V for the actuator, which draws the required current at the supplied voltage.

4 Calibration with CFD Data

This chapter focuses on the calibration of the measured flow velocity. This is necessary due to the sensor configuration with paddles that do not measure the exact velocity of the water. There are various reasons for this, such as friction in the bearings of the paddles and the density of PLA, which is higher than that of water. Additionally, the arms of the paddles also influence the flow in the cylinder. Therefore, velocity information from CFD simulations is used to calibrate the measurements.

4.1 CFD Software

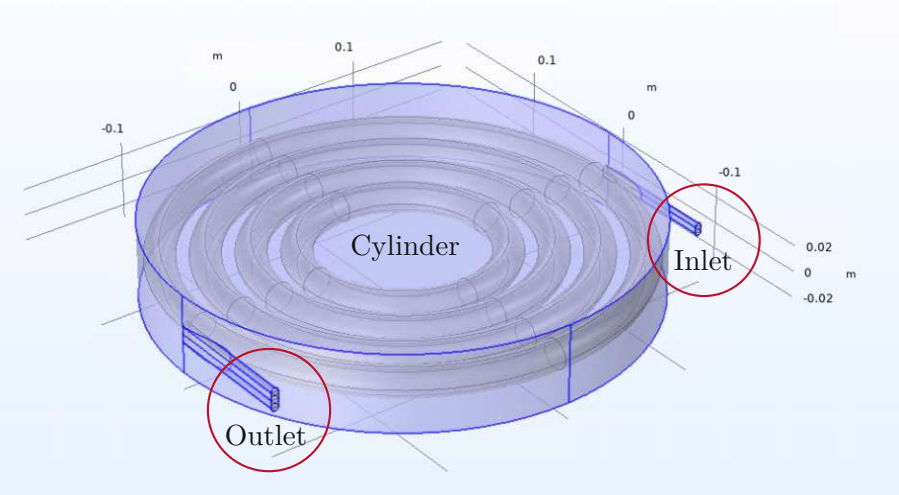

Figure 4.1: Cylinder for 3D simulations.

To carry out three-dimensional simulations at different flow rates, COMSOL Multiphysics is used.
No-slip conditions are used at the walls for the simulation, which means there is a boundary layer [29]. Figure 4.1 depicts all of the surfaces effected by this, including the inlet and the outlet. For the simulation, the velocity is prescribed at the inlet and the pressure at the outlet. Additionally, the average velocities over the area of the paddles is calculated. The toruses shown in Figure 4.1 are these areas that correspond to the positions of the four paddles along the radius.
Generally, the flow regime is turbulent. The simulations are based on the Reynolds-Averaged-Navier-Stokes (RANS) equations, which contain the Reynolds stresses and these require a turbulence model [48]. There are different options with varying number of

transport equations. In this work, a model of the $k-\varepsilon$ type is used, as it helps to reduce the computational load with only two transport equations. The alternative Reynolds stress model, for example, has seven transport equations. So, the $k-\varepsilon$ model is one of the simplest turbulence models and it can handle simple scenarios very well [49]. RANS models only the mean flow and how it is influenced by turbulence.
This turbulence model consists of two transport equations. One is the turbulent kinetic energy k and the other one is the turbulent kinetic energy dissipation rate ε [48]. With the equation

$$\mu_t = C_\mu \rho \frac{k^2}{\varepsilon}, \tag{4.1}$$

the turbulent viscosity can be determined [50]. C_μ in equation (4.1) is just a constant and ρ the density of the fluid. The turbulent viscosity μ_t is essential for calculating the Reynolds stress. The mesh shown in Figure 4.2 is tetrahedral.

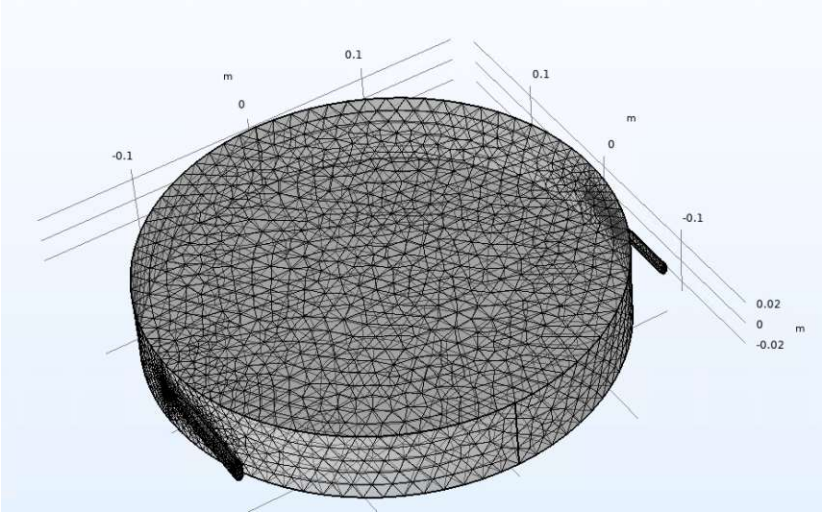

Figure 4.2: Tetrahedral mesh for the cylinder.

In total six equations have to be solved, including the two transport equations. The remaining ones are the three RANS equations and the continuity equation. The continuity equation [49] is

$$\rho \nabla \cdot \mathbf{u} = 0. \tag{4.2}$$

The incompressible RANS equations (3D momentum equations, see [49]) are

$$\rho(\mathbf{u} \cdot \nabla)\mathbf{u} = \nabla \cdot [-p\mathbf{l} + \mathbf{K}] + \mathbf{F} + \rho\mathbf{g}. \tag{4.3}$$

All symbols in bold are vectors such as the velocity $\mathbf{u}$. Therefore, (4.3) consists of three equations one for the x-component, y-component and the z-component. The $\mathbf{K}$ stands for

$$\mathbf{K} = (\mu + \mu_t)(\nabla\mathbf{u} + (\nabla\mathbf{u})^T). \tag{4.4}$$

The transport equation for k is

$$\rho(\mathbf{u}\cdot\nabla)k = \nabla\cdot\left[\left(\mu+\frac{\mu_t}{\sigma_k}\right)\nabla k\right] + P_k - \rho\varepsilon \tag{4.5}$$

and for ε [49] it equals

$$\rho(\mathbf{u}\cdot\nabla)\varepsilon = \nabla\cdot\left[\left(\mu+\frac{\mu_t}{\sigma_\varepsilon}\right)\nabla\varepsilon\right] + C_{\varepsilon 1}\frac{\varepsilon}{k}P_k - C_{\varepsilon 2}\rho\frac{\varepsilon^2}{k}. \tag{4.6}$$

The last equation is

$$P_k = \mu_t[\nabla\mathbf{u} : (\nabla\mathbf{u} + (\nabla\mathbf{u})^T)]. \tag{4.7}$$

This is the equation for the production of turbulent kinetic energy, which appears in the transport equations (4.5) and (4.6). The : stands for the Frobenius inner product of two matrices. Table 4.1 contains the values of the parameters in the equations.

Parameter	**Value**
$C_{\varepsilon 1}$	1.44
$C_{\varepsilon 2}$	1.92
C_μ	0.09
σ_k	1
σ_ε	1.3

Table 4.1: Numerical values of the parameters [49].

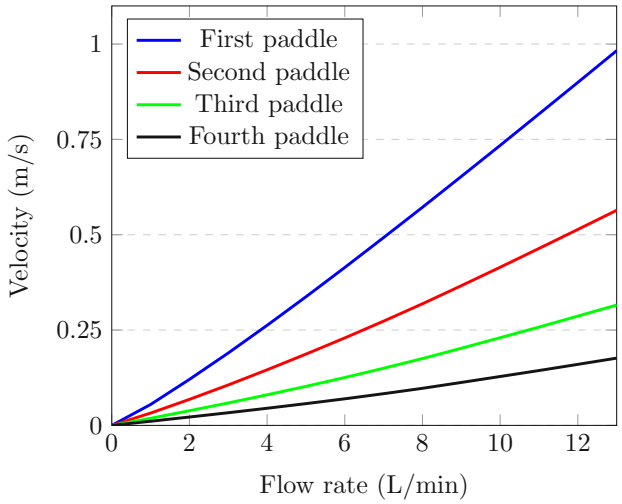

Figure 4.3: Graph of the flow velocity as a function of the flow rate from the CFD data.

4.2 Calibration

As the velocity sensor does not measure the exact velocity of the water flow, calibration is necessary. For this, the measured data is fitted to the simulated one with a least squares procedure. This method allows to determine the coefficients of a first order polynomial to calibrate the physical measurements. The calibrated velocities are used in the next chapter for the derivation of a control oriented vortex model.
Figure 4.3 shows the water velocities computed from the CFD simulations at the positions of the paddles as a function of the flow rate.
For the calibration, the CFD values serve as reference and the physical measurements are to be corrected based on this reference. In fact, the sum of the squared error

$$f_{err} = \sum_{n=1}^{m} (y_{CFD,n} - (a_2 \cdot y_{meas,n} + b_2))^2 \tag{4.8}$$

is minimized and the coefficients a_2 and b_2 for a first-order polynomial are determined [51]. This is carried out with the function polyfit in Matlab. The polynomial $a_2\, y_{meas,n} + b_2$ fits the measured data $y_{meas,n}$ to the CFD values $y_{CFD,n}$. Once the coefficients are known, the corrected calibrated measurements are calculated

$$\forall n \in \{1, \ldots, m\}, \quad y_{calib,n} = a_2 \cdot y_{\mathrm{meas},n} + b_2. \tag{4.9}$$

The same procedure is used for all four paddles. Figure 4.4 shows the simulated fluid velocities as well as the uncalibrated and the calibrated measurements at the first paddle (outermost paddle). The calibrated values are very close to the ones from the simulation.

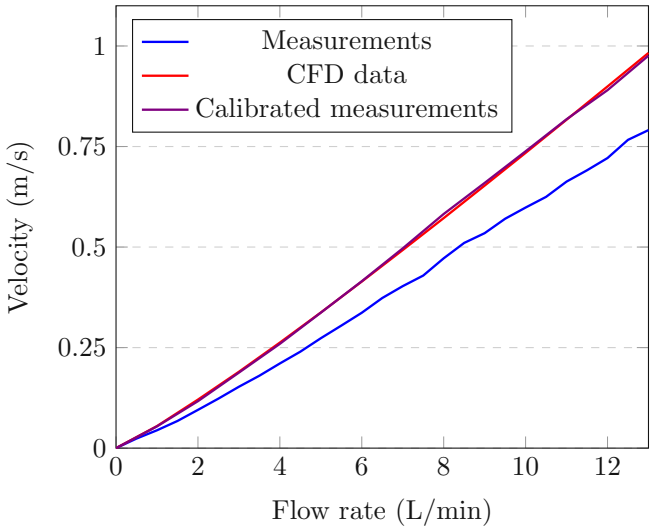

Figure 4.4: Graph of the flow velocity and flow rate, comparing CFD data, physical measurements and calibrated measurements for the outermost paddle (first paddle).

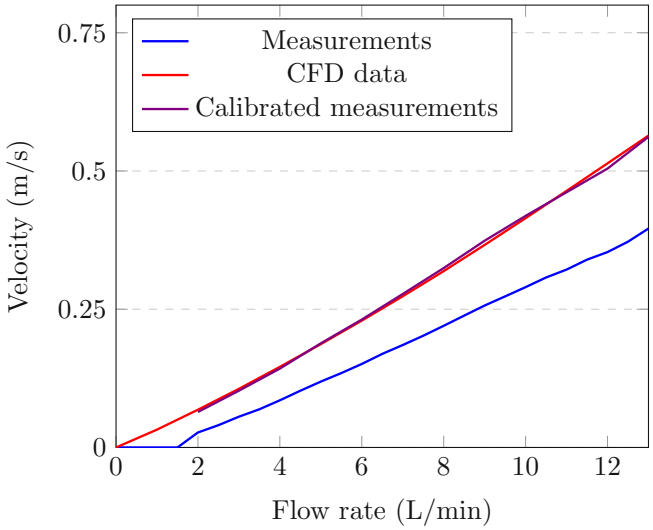

Figure 4.5: Graph of the flow velocity and flow rate, comparing CFD data, physical measurements and calibrated measurements for the second paddle.

The three inner paddles cannot measure a velocity at very low flow rates (see Figures 4.4 to 4.5). They start moving only at a flow rate of 2 to 3 L/min, depending on their initial angular position. For these three paddles, thus only non-zero measurements are utilized for calibration. This has no negative effect on the model, as only the calibrated measurements at 13 L/min are later required.
In Figure 4.5, there is a discrepancy, similar as for the first paddle, between the CFD data and physical measurements. Again the calibrated data is fitted quite well to the simulation results.

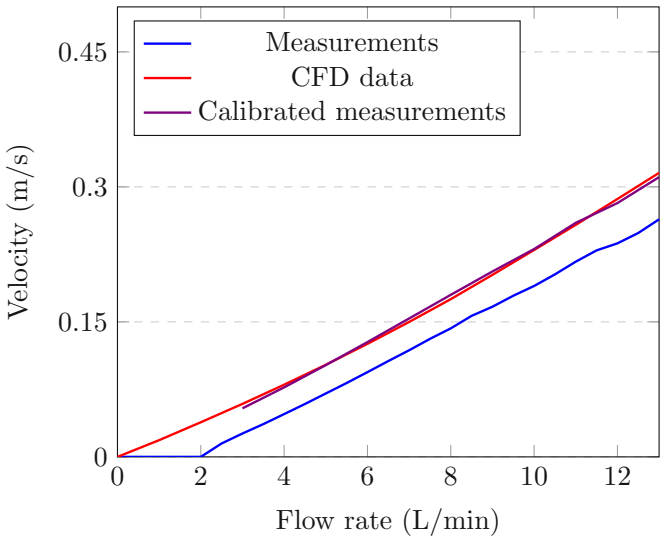

Figure 4.6: Graph of the flow velocity and flow rate, comparing CFD data, physical measurements and calibrated measurements for the third paddle.

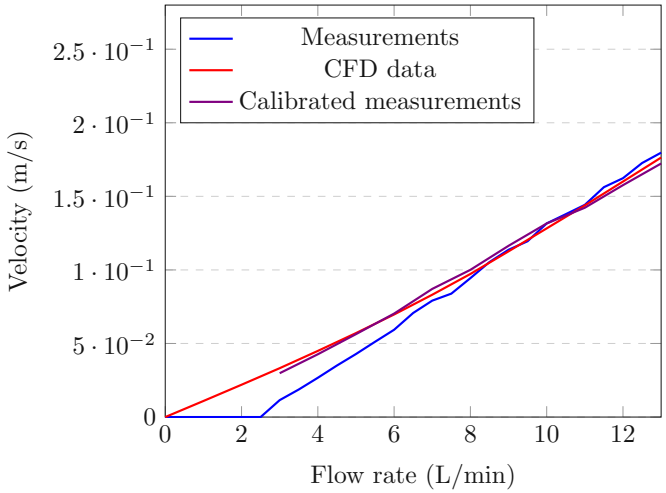

Figure 4.7: Graph of the flow velocity and flow rate, comparing CFD data, physical measurements and calibrated measurements for the fourth paddle.

For the third paddle, see Figure 4.6, the slopes of the measurements and simulation results are almost the same. Again, the calibrated data is fitted well to the CFD values.
The fourth graph in Figure 4.7 is qualitatively different from the others. The measurements and simulation velocities are almost equal at higher flow rates, which is only the case for the fourth paddle. At low flow rates, the CFD data gives higher velocities than the measurements. The reasons for this behavior are not entirely clear. Possibly the bearing friction plays a role in this regard.
At low velocities, static friction in the bearings of the paddles plays a more significant role. Additionally, the vortex has a complex structure, just like the boundary layer that forms at the inner surfaces. These effects make it difficult to accurately measure the velocity at low flow rates in the center.

5 Control-Oriented Vortex Model

In this section a two-dimensional steady-state model that describes the tangential velocity component of the confined vortex is derived. The basis for the derivation of the vortex model are the Navier-Stokes equations. These Partial Differential Equations (PDEs) from fluid mechanics can describe the flow of liquids and gases.

5.1 Navier-Stokes Equations

With the considered system being axisymmetric, the basis for the derived model are the Navier-Stokes equations in the cylindrical coordinates.
The constructed setup has a tangential input and output, generating a vortex that reaches maximum velocity near the vertical wall and that drops to zero at the center. Moreover, the system is closed with only water inside (and a few negligible air bubbles at the top). Furthermore, the sophisticated three dimensional boundary layer that forms at the inner surfaces of the cylinder is not modeled.
An important assumption of this model is that the fluid is incompressible, which means that the partial derivative of the density with respect to time vanishes.

$$\frac{\partial \rho}{\partial t} = 0 \tag{5.1}$$

In this case, the continuity equation equals

$$\frac{1}{r}\frac{\partial \rho r u_r}{\partial r} + \frac{1}{r}\frac{\partial \rho u_\phi}{\partial \phi} + \frac{\partial \rho u_z}{\partial z} = 0 \tag{5.2}$$

and the incompressible Navier-Stokes equation [52] for the r coordinate is

$$\begin{aligned} \rho\left(\frac{\partial u_r}{\partial t} + u_r\frac{\partial u_r}{\partial r} + \frac{u_\phi}{r}\frac{\partial u_r}{\partial \phi} + u_z\frac{\partial u_r}{\partial z} - \frac{{u_\phi}^2}{r}\right) &= -\frac{\partial p}{\partial r} \\ +\mu\left(\frac{1}{r}\frac{\partial u_r}{\partial r} + \frac{\partial^2 u_r}{\partial r^2} + \frac{1}{r^2}\frac{\partial^2 u_r}{\partial \phi^2} + \frac{\partial^2 u_r}{\partial z^2} - \frac{u_r}{r^2} - \frac{2}{r^2}\frac{\partial u_\phi}{\partial \phi}\right) + \rho g_r \end{aligned} \tag{5.3}$$

for the ϕ coordinate

$$\begin{aligned} \rho\left(\frac{\partial u_\phi}{\partial t} + u_r\frac{\partial u_\phi}{\partial r} + \frac{u_\phi}{r}\frac{\partial u_\phi}{\partial \phi} + u_z\frac{\partial u_\phi}{\partial z} + \frac{u_r u_\phi}{r}\right) &= -\frac{1}{r}\frac{\partial p}{\partial \phi} \\ +\mu\left(\frac{1}{r}\frac{\partial u_\phi}{\partial r} + \frac{\partial^2 u_\phi}{\partial r^2} + \frac{1}{r^2}\frac{\partial^2 u_\phi}{\partial \phi^2} + \frac{\partial^2 u_\phi}{\partial z^2} - \frac{u_\phi}{r^2} + \frac{2}{r^2}\frac{\partial u_r}{\partial \phi}\right) + \rho g_\phi \end{aligned} \tag{5.4}$$

and finally for the z coordinate

$$\begin{aligned}\rho\left(\frac{\partial u_z}{\partial t}+u_r\frac{\partial u_z}{\partial r}+\frac{u_\phi}{r}\frac{\partial u_z}{\partial \phi}+u_z\frac{\partial u_z}{\partial z}\right)&=-\frac{\partial p}{\partial z}\\ +\mu\left(\frac{1}{r}\frac{\partial u_z}{\partial r}+\frac{\partial^2 u_z}{\partial r^2}+\frac{1}{r^2}\frac{\partial^2 u_z}{\partial \phi^2}+\frac{\partial^2 u_z}{\partial z^2}\right)&+\rho g_z.\end{aligned} \tag{5.5}$$

All of the above equations are in cylindrical coordinates. As the system is closed and the inlet and outlet are tangential to the side walls, it is assumed that there is no flow in the z-direction, i.e.

$$u_z = 0. \tag{5.6}$$

Moreover, the small radial velocity is assumed to be zero, i.e.

$$u_r = 0. \tag{5.7}$$

Also, the gravitational components in all directions are zero, i. e.

$$g_\phi = g_r = g_z = 0. \tag{5.8}$$

Because of rotational symmetry, derivatives with respect to ϕ vanish, which means

$$\frac{\partial}{\partial \phi} = 0. \tag{5.9}$$

Since only a steady-state model is derived, derivatives with respect to t also vanish, thus

$$\frac{\partial}{\partial t} = 0. \tag{5.10}$$

With these assumption, merely the tangential velocity u_ϕ remains and (5.3) reduces to

$$\frac{\rho\, {u_\phi}^2}{r} = \frac{\partial p}{\partial r}, \tag{5.11}$$

which is the differential equation for the pressure model in Section 5.7. Equation (5.5) simplifies to

$$\frac{\partial p}{\partial z} = \rho g_z = 0, \tag{5.12}$$

which results in

$$p = p(0,r,t) + \int_0^z \rho g_z \; dz = p(0,r,t) + \rho g_z z. \tag{5.13}$$

This is the static pressure that acts on the bottom lid. Equation (5.4) simplifies to

$$0 = \frac{1}{r}\frac{\partial u_\phi}{\partial r} + \frac{\partial^2 u_\phi}{\partial r^2} + \frac{\partial^2 u_\phi}{\partial z^2} - \frac{u_\phi}{r^2}. \tag{5.14}$$

The solution of this partial differential equation will be computed in Section 5.4.

5.2 Boundary Conditions

For the vortex that is generated inside the cylinder, specific boundary conditions arise. First of all, the velocity at the center of the vortex is

$$u_\phi(0, z, Q) = 0. \tag{5.15}$$

Additionally, the velocity at the bottom lid equals

$$u_\phi(r, 0, Q) = 0 \tag{5.16}$$

and at the upper lid

$$u_\phi(r, H, Q) = 0. \tag{5.17}$$

The velocity at the position of the outermost paddle is

$$u_\phi(R_{pad1}, H/2, Q) = u_{\phi R_{pad1}}(Q) = A_1 Q^2 + A_2 Q. \tag{5.18}$$

This boundary condition for the tangential velocity is a function of the flow rate based on the calibrated measurements. This quadratic polynomial with offset zero is determined with the same method as in Chapter 4 with the polyfit function in Matlab, see (4.8). For this case the two data sets are the flow rate and velocity at the outermost paddle. The coefficients of this quadratic polynomial and the other parameters are listed in Table 5.1.

Parameter	**Value**
R_{pad1}	0.165 m
H	0.06 m
Q_{13}	13 L/min
A_1	0.000682079750307957
A_2	0.0677590851725335

Table 5.1: Numerical values of the parameters for the boundary conditions.

The control input for the vortex is the flow rate Q in L/min and this is described by the function $B(Q)$ that is multiplied with the derived model, see (5.39) and (5.45). This flow rate function is defined with the boundary condition (5.18) of the velocity at the outermost paddle with respect to the flow rate. With these constraints, the function describing the vortex can be determined.

5.3 Initial Conditions

The fluid initially has the velocity profile mainly consisting of a tangential component. Therefore, at the time

$$t_{in} = 0 \tag{5.19}$$

the radial velocity component is

$$u_r(r, z, t_{in}, Q) = 0. \tag{5.20}$$

and the axial velocity component equals

$$u_z(r, z, t_{in}, Q) = 0. \tag{5.21}$$

Additionally, the tangential velocity equals

$$u_\phi(r, z, t_{in}, Q) = f_m(r, z, t_{in}, Q). \tag{5.22}$$

For this case, the function f_m stands for the derived model that describes the vortex. As a steady-model is studied in this work the time dependent spin-up process of the vortex is not considered.

5.4 Solving the PDE

A steady-state two-dimensional model is derived for the vortex. The method of separation of variables [53] is used to solve the partial differential equation (5.14). The velocity is split up into two functions

$$u_\phi(r, z) = a(r)b(z) \tag{5.23}$$

and insertion in (5.14) gives

$$0 = \frac{\left(\frac{\partial^2 a(r)}{\partial r^2}\right) b(z) r + \left(\frac{\partial a(r)}{\partial r}\right) b(z)}{r} + a(r)\left(\frac{\partial^2 b(z)}{\partial z^2}\right) - \frac{a(r)b(z)}{r^2}. \tag{5.24}$$

Simplified this becomes

$$-\frac{\frac{\partial^2 b(z)}{\partial z^2}}{b(z)} = \frac{\left(\frac{\partial^2 a(r)}{\partial r^2}\right) r^2 + \left(\frac{\partial a(r)}{\partial r}\right) r - a(r)}{a(r) r^2} = k. \tag{5.25}$$

Both sides have to equal the constant k that has to be found. This is a standard approach for the separation of variables. The right hand side is

$$-\frac{\partial^2 b(z)}{\partial z^2} = b(z)\, k. \tag{5.26}$$

The general solution for this differential equation equals

$$b(z) = B_1 \sin\left(\sqrt{k}\, z\right) + B_2 \cos\left(\sqrt{k}\, z\right). \tag{5.27}$$

To fulfill the boundary condition (5.16) the cosine function is not part of the solution and therefore,

$$b(z) = B_1 \sin\left(\sqrt{k}\, z\right). \tag{5.28}$$

The next boundary condition (5.17) results in

$$b(H) = B_1 \sin\left(\sqrt{k}\, H\right) = 0 \tag{5.29}$$

therefore,

$$\sqrt{k}H = \pi \rightarrow k = \frac{\pi^2}{H^2}. \tag{5.30}$$

Thus, the solution is

$$b(z) = B_1 \sin\left(\frac{\pi}{H}\, z\right). \tag{5.31}$$

The second differential equation on the left hand side

$$\frac{\left(\frac{\partial^2 a(r)}{\partial r^2}\right) r^2 + \left(\frac{\partial a(r)}{\partial r}\right) r - a(r)}{a(r) r^2} = k \tag{5.32}$$

is rearranged to

$$\left(\frac{\partial^2 a(r)}{\partial r^2}\right) r^2 + \left(\frac{\partial a(r)}{\partial r}\right) r - a(r)\left(k\, r^2 + 1\right) = 0. \tag{5.33}$$

The solution of (5.33) is a modified Bessel-function of the first kind. Using the change of variables

$$\tilde{r} = r\frac{\pi}{H} \tag{5.34}$$

and the derivative equals

$$\frac{\partial}{\partial r} = \frac{\pi}{H}\frac{\partial}{\partial \tilde{r}}. \tag{5.35}$$

With this the equation (5.33) can be rewritten into

$$\left(\frac{\partial^2 \tilde{a}(\tilde{r})}{\partial \tilde{r}^2}\right) \tilde{r}^2 + \left(\frac{\partial \tilde{a}(\tilde{r})}{\partial \tilde{r}}\right) \tilde{r} - \tilde{a}(\tilde{r})\left(\tilde{r}^2 + 1\right) = 0. \tag{5.36}$$

The general solution equals

$$a(\tilde{r}) = c_1 I_1(\tilde{r}) + c_4 K_1(\tilde{r}). \tag{5.37}$$

Solution (5.37) consists of the first order modified Bessel function of the first and second kind. The first order modified Bessel function of the second kind K_1 is not part of the solution, as it goes to infinity at the origin [54]. Hence, the solution is

$$a(r) = c_1 I_1\left(r\frac{\pi}{H}\right). \tag{5.38}$$

The tangential velocity function equals

$$u_\phi(r, z, Q) = B(Q) I_1\left(r\frac{\pi}{H}\right)\sin\left(\frac{\pi}{H}z\right). \tag{5.39}$$

The flow rate function $B(Q)$, which contains the unknown parameters c_1 and B_1 is chosen to satisfy the boundary condition (5.18). Additionally, the paddles average the velocity over the area of their cross-section. Therefore, the modified Bessel function I_1 and the sine function are numerically integrated over the diameter of the outermost paddle and divided by the area. This way the average tangential velocity is calculated.
For the integral the coordinates are transformed into polar ones. In this case, ρ_p stands for the radial coordinate in the polar coordinate system and ϕ_p for the angle [55]. The cylindrical radial coordinate is

$$r = R_{pad1} + \rho_p \cos(\phi_p) \tag{5.40}$$

and the cylindrical z-component equals

$$z = H/2 + \rho_p \sin(\phi_p). \tag{5.41}$$

As the velocity for the outermost paddle is determined, R_{pad1} is added in (5.40) and $H/2$ in (5.41). The radius of the paddle (hemispherical-cup) is

$$R_p = 0.011 \text{ m}. \tag{5.42}$$

With the introduction of these polar coordinates [55] the integral is

$$\overline{u_\phi} = \frac{1}{\pi R_p^2}\int_0^{2\pi}\int_0^{R_p} u_\phi(R_{pad1} + \rho_p\cos\phi_p, H/2 + \rho_p \sin\phi_p)\cdot \rho_p \, d\rho_p \, d\phi_p. \tag{5.43}$$

This is the average tangential velocity $\overline{u_\phi}$ and the integral is numerically solved in Matlab. With the boundary condition (5.18) the flow rate function $B(Q)$ can be determined. As the value of the integral is constant with respect to the flow rate, the value of $B(Q)$ for each flow rate can be determined with

$$u_{\phi R_{pad1}}(Q) = B(Q)\,\overline{u_\phi} \rightarrow B(Q) = \frac{u_{\phi R_{pad1}}(Q)}{\overline{u_\phi}}. \tag{5.44}$$

Using this information and the same method as in Chapter 4 a second-order polynomial (without an offset) describing $B(Q)$ is fitted to this data with polyfit in Matlab, see (4.8). Hence, the result is

$$B(Q) = A_3 Q^2 + A_4 Q. \tag{5.45}$$

Table 5.2 contains the numerical values of the coefficients of the flow rate function. Moreover, the measured velocity is approximately proportional to the flow rate Q in L/min, see Figure 5.1. Therefore, the polynomial (5.45) is not linear.
In Figure 5.2 the model is compared with the CFD data and the calibrated measurements at a height of 0.03 m.

Parameter	Value
A_3	$9.35269557536301 \cdot 10^{-7}$
A_4	$9.29114367927910 \cdot 10^{-5}$

Table 5.2: Numerical values of the coefficients of the flow rate function.

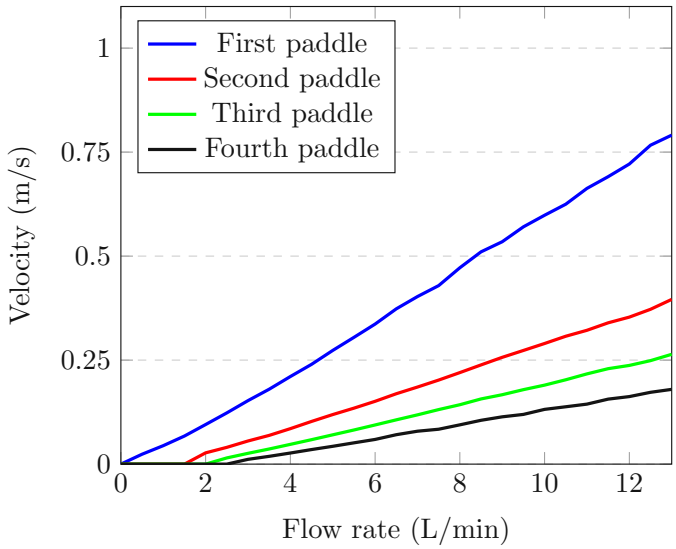

Figure 5.1: Vortex velocities and flow rate from the test stand.

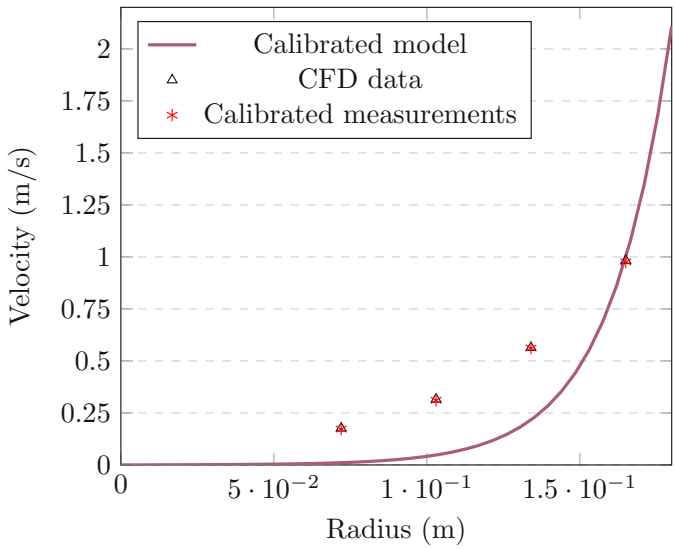

Figure 5.2: Graph of the model, calibrated measurements and CFD data for the tangential velocity at 13 L/min.

Clearly, there is a significant plant-model mismatch in Figure 5.2. One reason is the simplification that the radial velocity u_r is zero. This component exists due to the variation in pressure over the radius.
Additionally, the assumption that the axial velocity u_z is zero further worsens the accuracy of the analytical solution.
Without these it is difficult to exactly model the fluid flow as it turbulent and not laminar. The boundary layer is not modeled with this analytical solution. As the cylinder is only 60 mm high, the boundary layer influences the velocity profile.

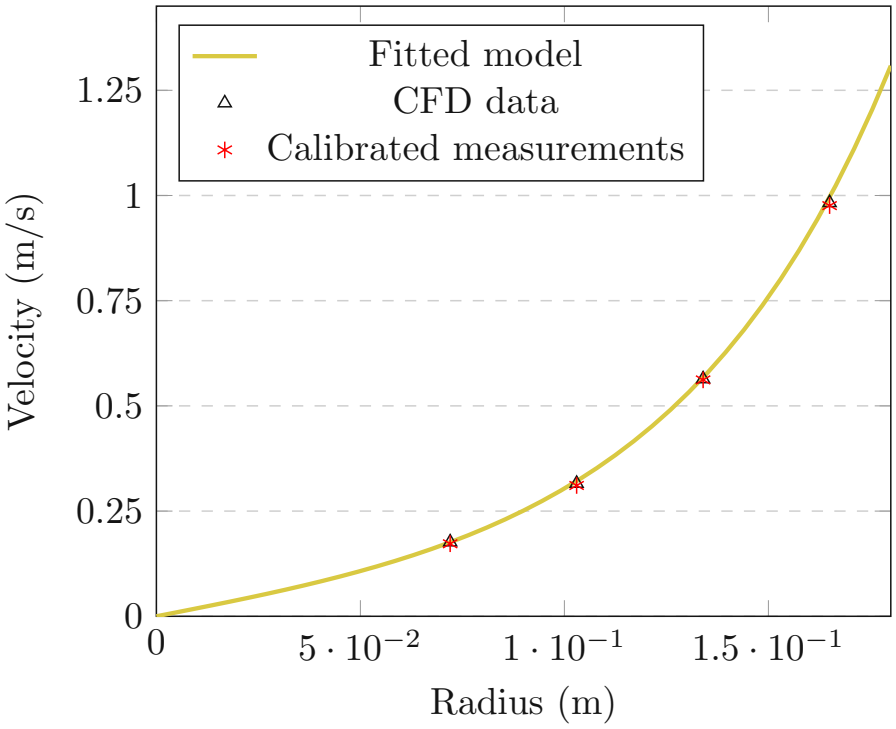

Figure 5.3: Graph of the fitted model, calibrated measurements and CFD data for the tangential velocity at 13 L/min and a height of 0.03 m.

5.5 Fitted Model

The analytical solution (5.39) is not in agreement with the measurements for the three inner paddles, see Figure 5.2. Therefore, the model is fitted to the four measurements of the paddles with a nonlinear least squares approach. This is necessary as the first order modified Bessel function is nonlinear. The fitted tangential velocity function equals

$$u_\phi(r,z,Q) = \alpha_1 B_f(Q) I_1\left(r\frac{\pi}{H}\alpha_2\right)\sin\left(\frac{\pi}{H}z\right). \tag{5.46}$$

The two correction factors are α_1 and α_2. To find these the function

$$F_{fit}(\boldsymbol{\alpha}) = \sum_{i=1}^{4} (u_{\phi,\text{measured}}(r_i) - u_{\phi,\text{model}}(r_i, \boldsymbol{\alpha}))^2 \tag{5.47}$$

is minimized by finding the optimal correction factors for the four points along the radius r_i [56]. In this case, $\boldsymbol{\alpha}$ stands for the vector that contains α_1 and α_2. The function $u_{\phi,\text{measured}}(r_i)$ stands for the measured tangential velocities at the four points along the radius and $u_{\phi,\text{model}}(r_i, \boldsymbol{\alpha})$ is the velocity of the model (5.46) with the correction factors. The first optimal correction factor is

$$\alpha_1 = 0.185177 \tag{5.48}$$

and the second

$$\alpha_2 = 0.384343. \tag{5.49}$$

The flow rate function is

$$B_f(Q) = A_5 Q^2 + A_6 Q \tag{5.50}$$

for the fitted model. Similar to the function (5.45) this is a quadratic polynomial without an offset. This function has very similar coefficients to the boundary condition (5.18), see Table 5.1 and Table 5.3. The coefficients are determined with the same approach as in the previous section, see (5.44).

Parameter	**Value**
A_5	0.000697932664778
A_6	0.0693339435103216

Table 5.3: Numerical values of the coefficients of the flow rate function $B_f(Q)$.

Figure 5.3 shows the graph of the fitted model (5.46), calibrated measurements and CFD data. Clearly, the fitted model at a flow rate of 13 L/min is in good agreement with the calibrated measurements.

5.6 Model Validation

This section compares the fitted analytical model (5.46), based on the data at 13 L/min, to the calibrated measurements at different flow rates.
The measured and modeled velocities for the flow rates ranging from 9 to 12 L/min are compared in Figure 5.4. Figure 5.5 shows the same comparison for the flow rates 5 to 8 L/min. The model-plant mismatch is small for 12 L/min but increases for smaller flow rates.

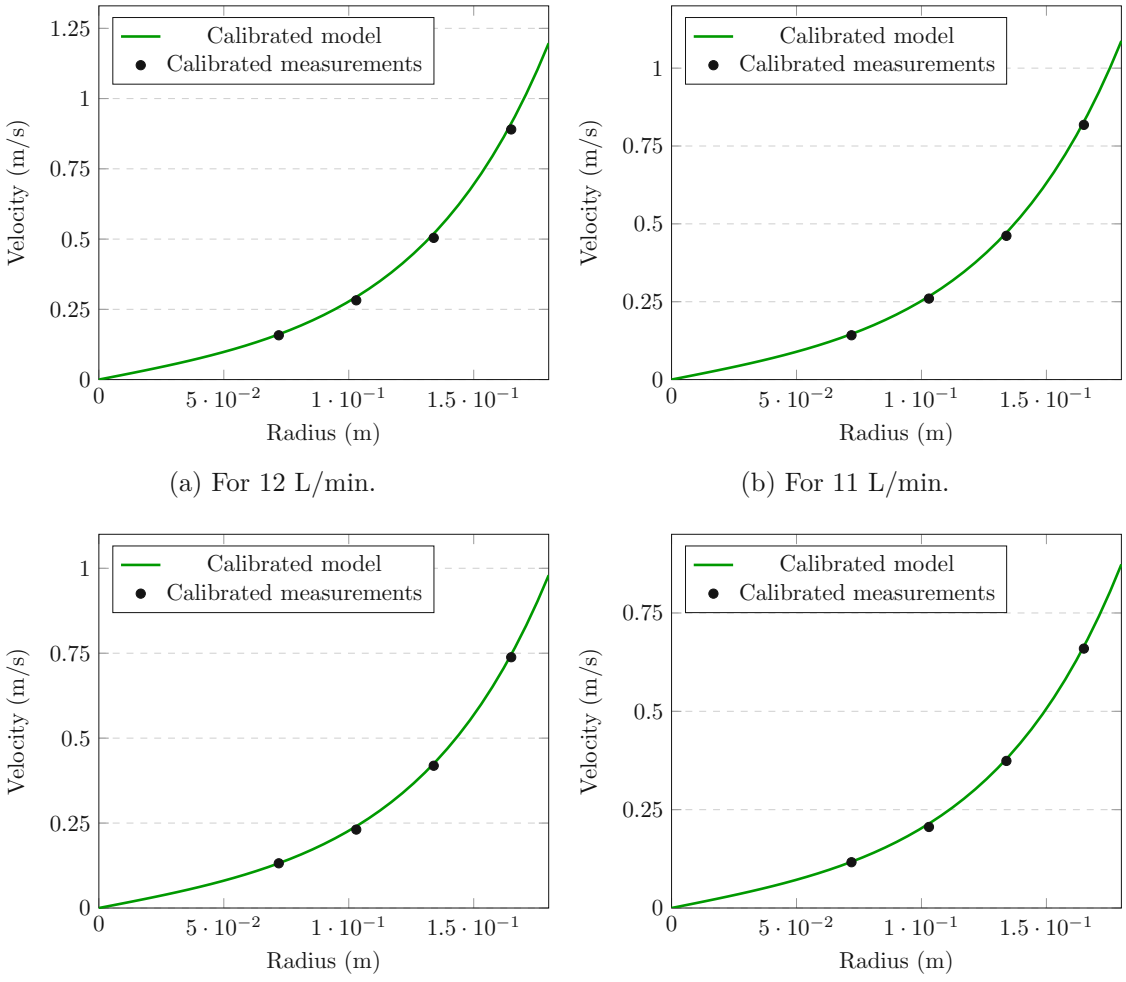

(a) For 12 L/min.

(b) For 11 L/min.

(c) For 10 L/min.

(d) For 9 L/min.

Figure 5.4: Graphs of the fitted model and measurements from 9 to 12 L/min at a height of 0.03 m.

There seems to be a linear relationship between flow rate and flow velocity but the deviation between measurements and model increases at lower flow rates. Generally, the accuracy of the fitted model is acceptable.

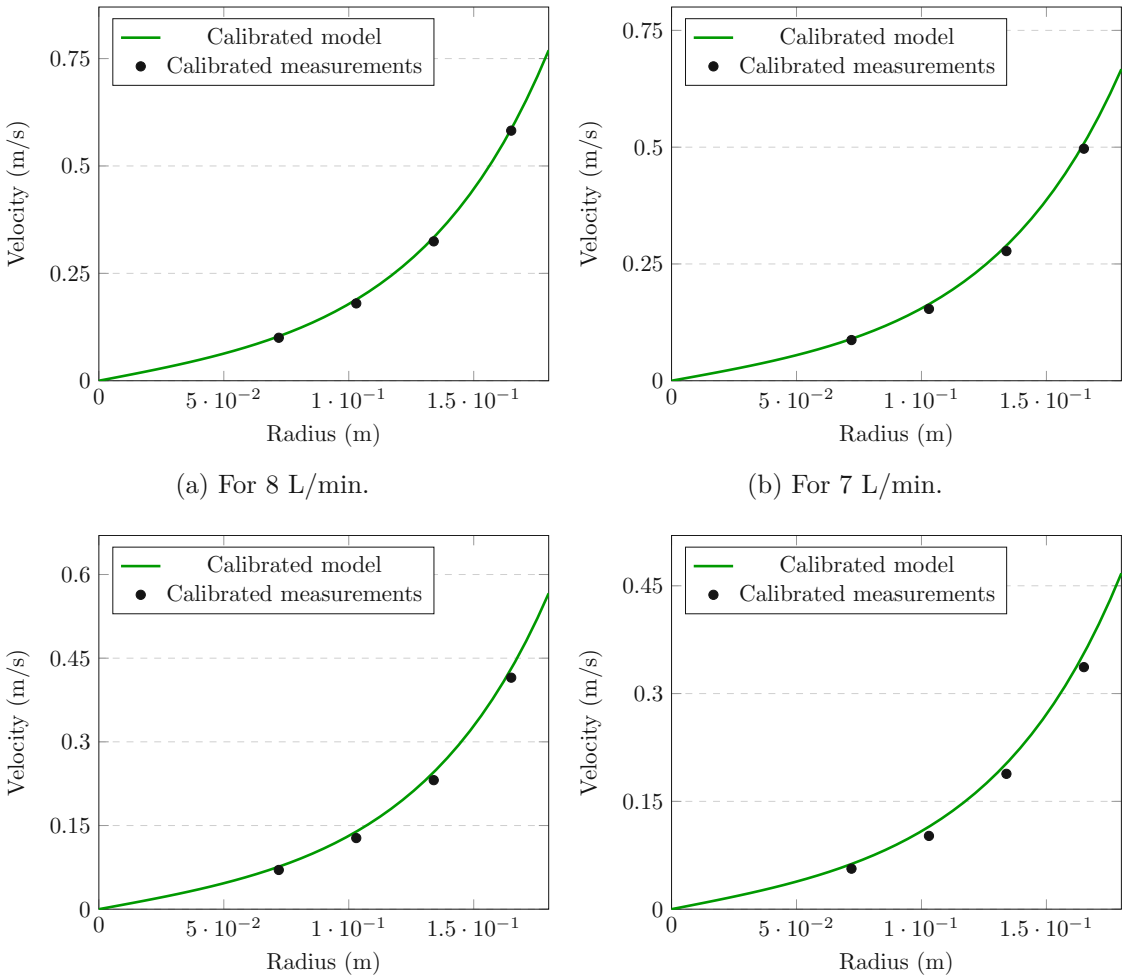

(a) For 8 L/min.

(b) For 7 L/min.

(c) For 6 L/min.

(d) For 5 L/min.

Figure 5.5: Graphs of the fitted model and measurements from 5 to 8 L/min at a height of 0.03 m.

5.7 Pressure Model

A model for the pressure can be derived from the expression (5.11), i.e. the differential equation

$$\frac{\partial p(r,z,Q)}{\partial r} = \frac{\rho\, u_\phi(r,z,Q)^2}{r}. \tag{5.51}$$

The solution $p(r,z,Q)$ describes how the pressure changes with the radius r, the axial coordinate z and flow rate Q. The equation depends on the velocity u_ϕ and this function itself depends on the same variables. Therefore, the solution $u_\phi(r,z,Q)$ has to be substituted into the equation and then the differential equation can be solved for $p(r,z,Q)$. This yields

$$\begin{aligned} p(r,z,Q) = \lambda_2 B_f(Q)^2\Big(\sin^2(\lambda_1 z)\Big) I_0(\lambda_3 r)^2 \\ -\lambda_2 B_f(Q)^2\Big(\sin^2(\lambda_1 z)\Big) I_1(\lambda_3 r)^2 \\ -\lambda_2 B_f(Q)^2\Big(\sin^2(\lambda_1 z)\Big) + p_c. \end{aligned} \tag{5.52}$$

I_0 and I_1 are the modified Bessel functions of the first kind. The pressure constant p_c can be determined with the boundary condition

$$p(R_{pad1}, H/2, Q_{13}) = p_R, \tag{5.53}$$

which is the pressure at the outermost paddle at the height of 0.03 m. This boundary condition is unknown, as no pressure measurements are taken inside the cylinder. All parameters for this boundary condition are defined in Table 5.1. Through the integration of the velocity function, which consists of the first order modified Bessel function of the first kind a zero order modified Bessel function is also added. Table 5.4 contains the numerical values of the three parameters λ_1, λ_2 and λ_3.

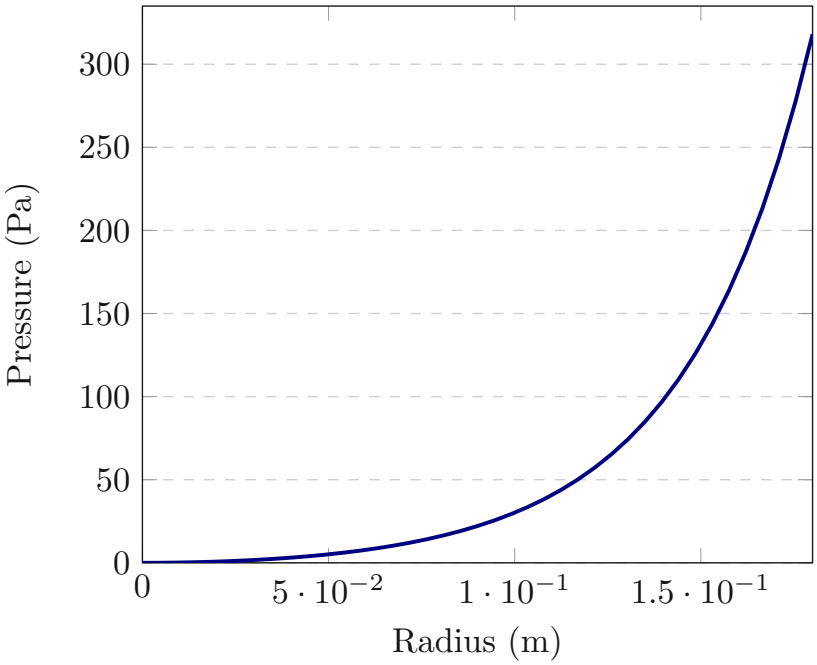

Figure 5.6: Graph of the derived pressure model at a flow rate of 13 L/min at a height of 0.03 m without the pressure constant p_c.

Figure 5.6 shows the graph of the derived pressure model based on the fitted velocity model of the vortex, without the pressure constant. Therefore, this is not a graph showing the absolute pressure, but instead shows how the pressure varies with the radius.
The pressure increases with the radius and therefore, the highest pressure occurs at the cylindrical wall. Furthermore, the flow rate function $B_f(Q)$ appears quadratic in the

pressure function. This implies, that when the flow rate is doubled the pressure increase will be four fold.

Parameter	Value
λ_1	52.35987758
λ_2	17.11607497
λ_3	20.12416381

Table 5.4: Numerical values of the coefficients of the flow rate function.

5.8 Dynamic Model

The dynamic model for the tangential velocity of the vortex is not derived. For this case, the time derivatives in the Navier-Stokes equations also have to be taken into account and solved. This allows to analyze the dynamic behavior of the vortex, such as the spin-up process.

6 Controller for the Vortex

Controlling the vortex and the actuator of the test stand is the focus of this chapter. Cascade control is implemented for this purpose, with the inner loop responsible for the pump and the outer loop for the water vortex. So, first the cascade controller is briefly elaborated. Then the inner loop controller for the pump is described and finally the outer loop controller for the vortex.

6.1 Cascade Control

This section briefly focuses on the cascade control [57] that consists of the vortex and actuator controllers, with the inner loop consisting of the pump and the outer one of the vortex.

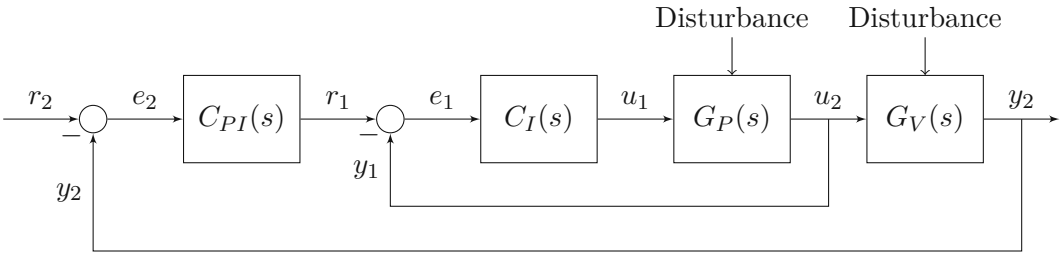

Figure 6.1: Cascade control circuit with the pump and vortex.

Figure 6.1 illustrates the cascade control structure of the entire system. Table 6.1 and Table 6.2 briefly elaborate all relevant symbols of the control circuit.

Symbol	Description
r_1	Pump setpoint for flow rate in L/min
u_1	Pump control input in V
y_1	Measured pump flow rate in L/min
e_1	Pump control error in L/min
r_2	Setpoint for vortex velocity at the outermost paddle in m/s
u_2	Vortex control input in L/min
y_2	Measured vortex velocity at the outermost paddle in m/s
e_2	Vortex control error in m/s

Table 6.1: Control circuit symbols part one for Figure 6.1.

Symbol	Description
$C_{PI}(s)$	PI controller transfer function
$C_I(s)$	Integral controller transfer function
$G_P(s)$	Pump transfer function
$G_V(s)$	Vortex transfer function

Table 6.2: Control circuit symbols part two for Figure 6.1.

The vortex and the pump have different dynamics. Moreover, the pump is considerably faster than the vortex, which is also necessary. The inner control loop should be approximately 5 times faster than the outer loop [58]. This is fulfilled as the pump requires around 3 seconds and the vortex approximately 30 seconds to reach a similar set point, as shown in Figures 6.5 and 6.11. Additionally, the hall sensor measuring the flow rate is quicker than the developed velocity sensor. Therefore, this control structure works, as the inner loop is faster than the outer one.

6.2 Pump Control

This section concentrates on the control strategy and implementation of the pump controller. The controller gets feedback from a flow meter that uses a hall effect sensor.

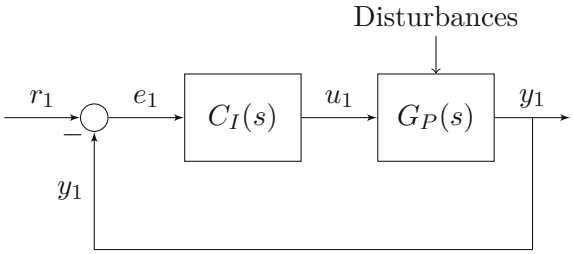

Figure 6.2: Pump control circuit with integral controller.

Figure 6.2 shows the control architecture for the pump. The transfer function of the plant equals

$$G_P(s) = \frac{Q(s)}{U(s)} = \frac{K_1}{1 + T_1 s}. \tag{6.1}$$

with the gain

$$K_1 = 1.5002 \text{ (L/min)/V} \tag{6.2}$$

and the time constant

$$T_1 = 0.0637 \text{ s}. \tag{6.3}$$

The volumetric flow rate $Q(t)$ in L/min is the output and the reference voltage $u(t)$ in V is the input. The transfer function (6.1) can be identified using a measured open-loop step response in Matlab, with the PID Tuner application. The estimated transfer function $G_P(s)$ for the plant is strictly proper, as there are more poles than zeros [59].
In Figure 6.3 the open-loop step response of the pump is shown. An 8 V step is sent to the motor driver, which is amplified and the pump reaches a flow rate of 12 L/min.

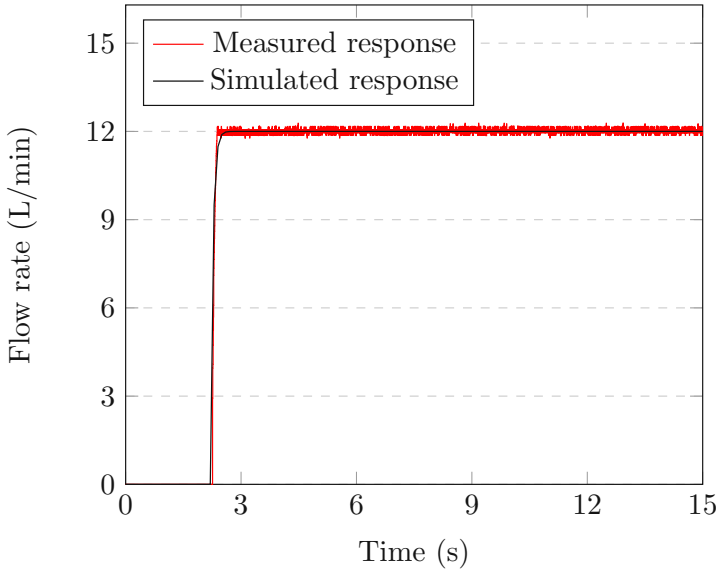

Figure 6.3: Open-loop step response of the pump and estimated transfer function.

Figure 6.3 also shows the comparison between the measured step response and the step response of the estimated transfer function $G_P(s)$. Clearly, the step responses are identical. Also, the plant needs to be Bounded-Input Bounded-Output (BIBO) stable for open-loop operation. This means that all poles of the system have a negative real part [60]. The pole of $G_P(s)$ is at

$$s = -15.6986. \tag{6.4}$$

Therefore, the pump can be operated in an open-loop. The setpoint r_1 of the inner control loop is the flow rate in L/min and y_1 the measured flow rate. The hall sensor signal delivers the actual flow rate of the pump and with this information the control error equals

$$e_1(t) = r_1(t) - y_1(t). \tag{6.5}$$

The controller was manually tuned directly at the physical setup. Additionally, the phase margin should be at least 40 degrees and the gain margin at least 30 dB.
The tuned integral controller calculates the control variable $u_1(t)$, which is the input voltage of the pump. The signal is then forwarded to the motor driver. The controller output in the time domain [57] equals

$$u_1(t) = K_I \int_0^t e_1(\tau)\, d\tau. \tag{6.6}$$

Hence, the transfer function of the controller is

$$C_I(s) = \frac{K_I}{s} \tag{6.7}$$

with the integral gain

$$K_I = 1 \text{ V}/(\text{L}/\text{min} \cdot \text{s}). \tag{6.8}$$

Anti-windup measure are implemented by limiting the output of the controller to 9 V, which corresponds to the maximum voltage of 24 V for the pump.

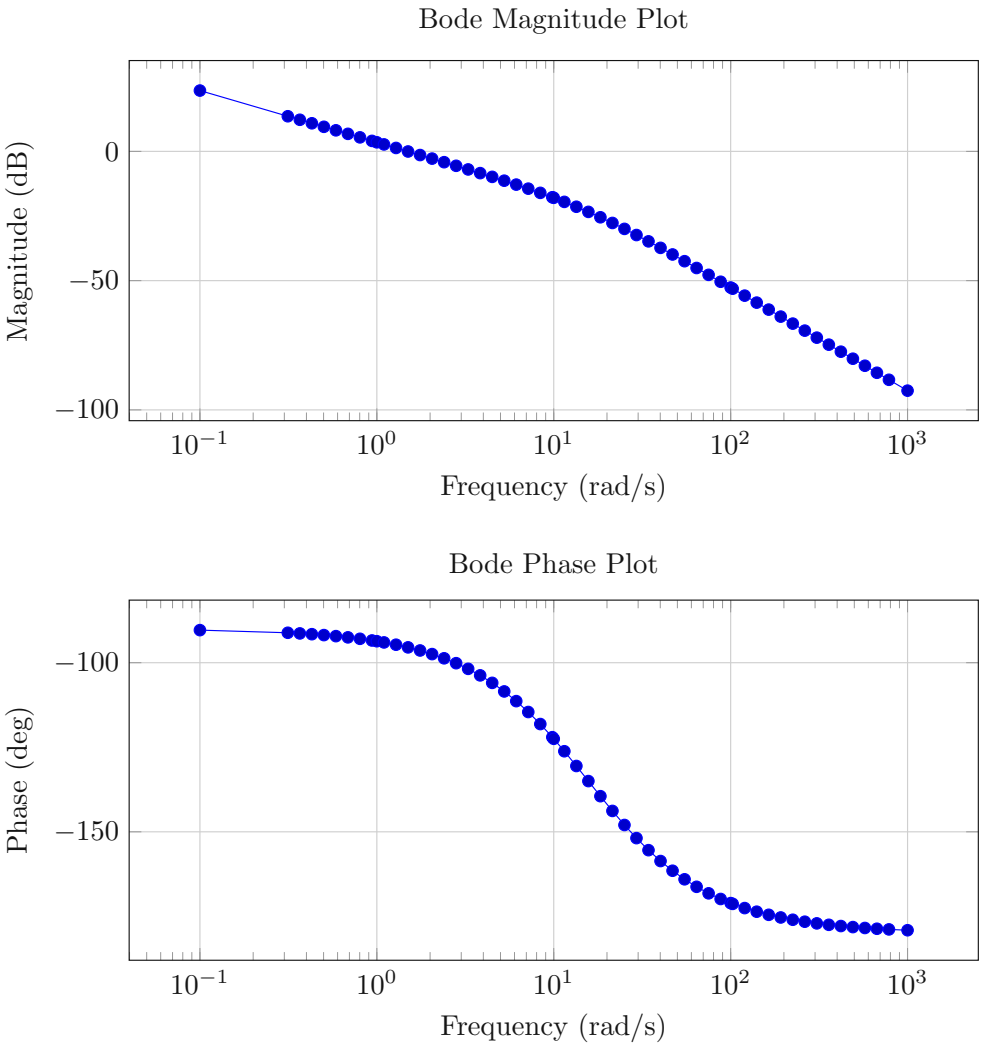

Figure 6.4: Bode plot of the open-loop transfer function $C_I(s)\, G_P(s)$ of the pump.

The gain margin is infinite because the phase response never reaches -180°, see Bode plot for the open-loop transfer function $C_I(s)\,G_P(s)$ in Figure 6.4 [37]. The phase margin is 84.6 degrees at 1.49 rad/s. Therefore, the requirements regarding the phase and gain margin are fulfilled.
With this controller tuning, the pump swiftly reaches the desired flow rate and does not overshoot with this simple controller. The closed-loop transfer function is

$$T_{r_1,y_1}(s) = \frac{C_I(s)\,G_P(s)}{1 + C_I(s)\,G_P(s)} = \frac{K_1}{T_1 s^2 + s + K_1}. \tag{6.9}$$

The two real negative poles of the closed-loop transfer function are at

$$s = -14.019 \tag{6.10}$$

and

$$s = -1.68. \tag{6.11}$$

Therefore, the closed-loop is BIBO stable. Moreover, stability problems were not observed during normal operation.

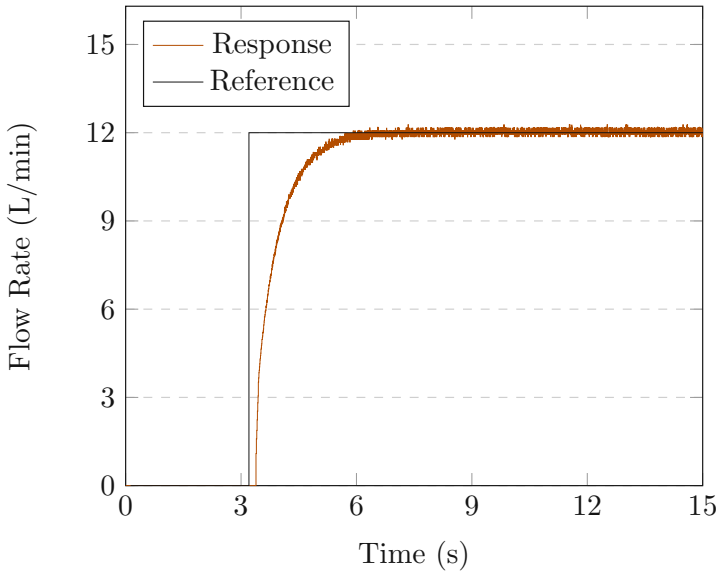

Figure 6.5: Measured closed-loop step response of the pump.

Figure 6.5 shows the measured closed-loop step response of the pump controller. The signal contains some noise from the hall sensor. Generally, the pump reaches the setpoint within a few seconds and then maintains the flow rate.

6.3 Controlling the Vortex

First feedforward control of the vortex is examined and then closed-loop operation. For the vortex a simple PI controller is manually tuned at the physical setup.

6.3.1 Feedforward Controller

The vortex can be operated in an open-loop manner, although the inner loop that controls the pump is closed. Then the setup only requires a sensor for the flow rate of the pump.

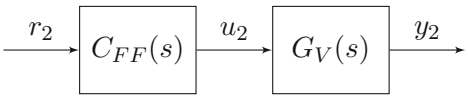

Figure 6.6: Basic feedforward control of the vortex.

Figure 6.6 shows the structure of the feedforward controller for the vortex. So, r_2 is the setpoint in m/s for the outermost paddle, u_2 the control input in L/min and y_2 the measured velocity at the outermost paddle in m/s.
With the PID Tuner application from Matlab, the measured step response in Figure 6.8 can be processed to estimate a transfer function $G_V(s)$ of the vortex. The tangential velocity of the outermost paddle $u_\phi(t)$ in m/s is the output and the reference flow rate $Q(t)$ in L/min is the input. The estimation yields the transfer function

$$G_V(s) = \frac{U_\phi(s)}{Q(s)} = \frac{K_2}{1 + T_2 s} \tag{6.12}$$

with the time constant

$$T_2 = 3.4838 \text{ s} \tag{6.13}$$

and the gain

$$K_2 = 0.061414 \ (\text{ms}^{-1})/(\text{L/min}). \tag{6.14}$$

The estimated transfer function $G_V(s)$ for the vortex is strictly proper, as there are more poles than zeros.

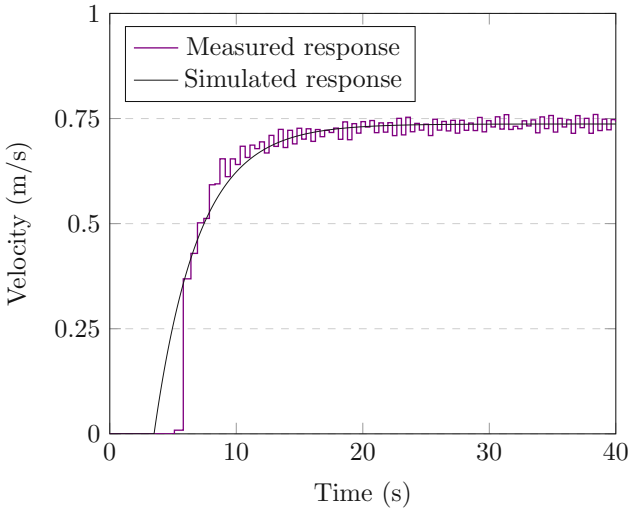

Figure 6.7: Open-loop step response of the vortex and estimated transfer function.

The control structure in Figure 6.6 cannot react to disturbances and requires the plant to be BIBO stable. As the single real negative pole of $G_V(s)$ is at

$$s = -0.2870 \tag{6.15}$$

the criterion is fulfilled. This is a very simple setup and did not become unstable during testing.
Figure 6.7 shows the measured step response of the vortex and the step response of the estimated vortex transfer function $G_V(s)$. As expected, the transfer function responds similarly to the same step input. The control input for $G_V(s)$ is

$$u_2 = C_{FF}(s)\, r_2. \tag{6.16}$$

The transfer function for the feedforward controller is

$$C_{FF}(s) = K_{stat} = \frac{13\,\mathrm{L/min}}{0.7908\,\mathrm{m/s}} = 16.439\ \frac{\mathrm{L/min}}{\mathrm{m/s}}. \tag{6.17}$$

This is a static gain, which equals the flow rate 13 L/min divided by the measured velocity at this flow rate, see Figure 5.1. So for this 12 L/min step response the setpoint is

$$r_2 = \frac{u_2}{K_{stat}} = 0.73\ \mathrm{m/s}. \tag{6.18}$$

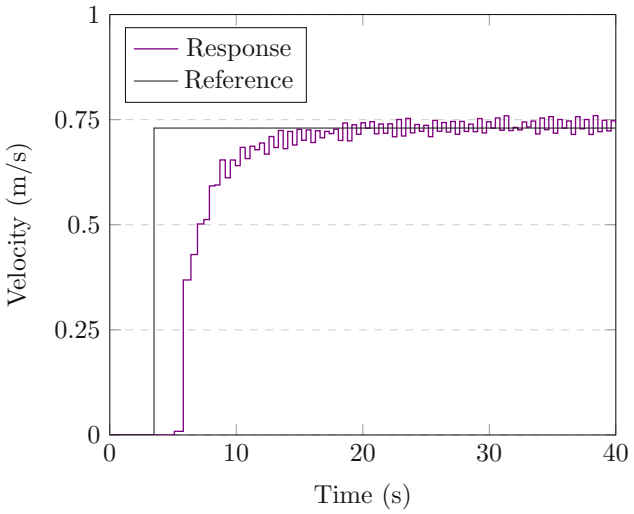

Figure 6.8: Measured open-loop step response of the vortex.

Figure 6.8 shows the open-loop step response of the feedforward control structure for a 0.73 m/s reference step. At the pump this requires a 12 L/min step. In Figure 6.8 there is a small steady-state error due to the lack of feedback and the model-plant mismatch. In addition, the estimated transfer function $G_V(s)$ of the vortex is a dynamic model for analyzing the control structure. On the other hand, the model in Chapter 5 is a steady-state model of the vortex.

6.3.2 Closed-Loop Control

In this subsection the inner loop with the pump is closed and also the outer loop with the vortex. This is cascade control as shown in Figure 6.1.
With the designed velocity sensor closed-loop control can be realized. Setpoint for this loop is the desired velocity of the vortex at the outermost paddle r_2, as only one measurement is required for feedback.

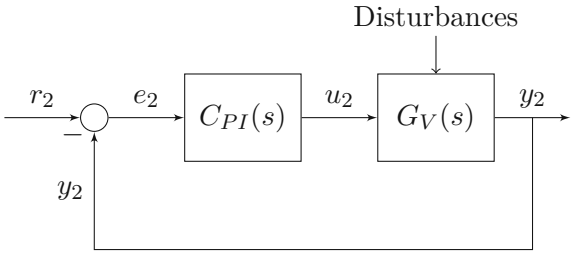

Figure 6.9: Basic vortex control circuit.

Based on the reference vortex velocity r_2, the control error is

$$e_2(t) = r_2(t) - y_2(t). \tag{6.19}$$

A PI controller [57] is implemented, which has the time-domain control law

$$u_2(t) = K_P\ e_2(t) + K_I \int_0^t e_2(\tau)\ d\tau. \tag{6.20}$$

Its transfer function is

$$C_{PI}(s) = K_P + \frac{K_I}{s}. \tag{6.21}$$

The PI controller for the vortex was tuned manually directly at the physical setup. Additionally, the phase margin should be at least 40 degrees and the gain margin at least 30 dB. Additionally, the controller should avoid overshooting.
In order to asses the stability, the transfer function of the plant (6.12), which is estimated in the previous subsection is required. Differential gain is not necessary and not robust regarding high-frequency measurement noise.
The proportional gain is

$$K_P = 0.37\ \text{(L/min)/(ms}^{-1}\text{)} \tag{6.22}$$

and

$$K_I = 1.30\ \text{(L/min)/m}. \tag{6.23}$$

To counteract the windup effect clamping is implemented for the integral gain and the output limited to 13 L/min. With this controller the gain margin is infinite because the phase response never reaches -180°, see Bode plot in Figure 6.10. On the other hand, the

phase margin is 76.2 degrees at 0.0771 rad/s in Figure 6.10, as calculated by Matlab with the vortex open-loop transfer function $C_{PI}(s)\,G_V(s)$.

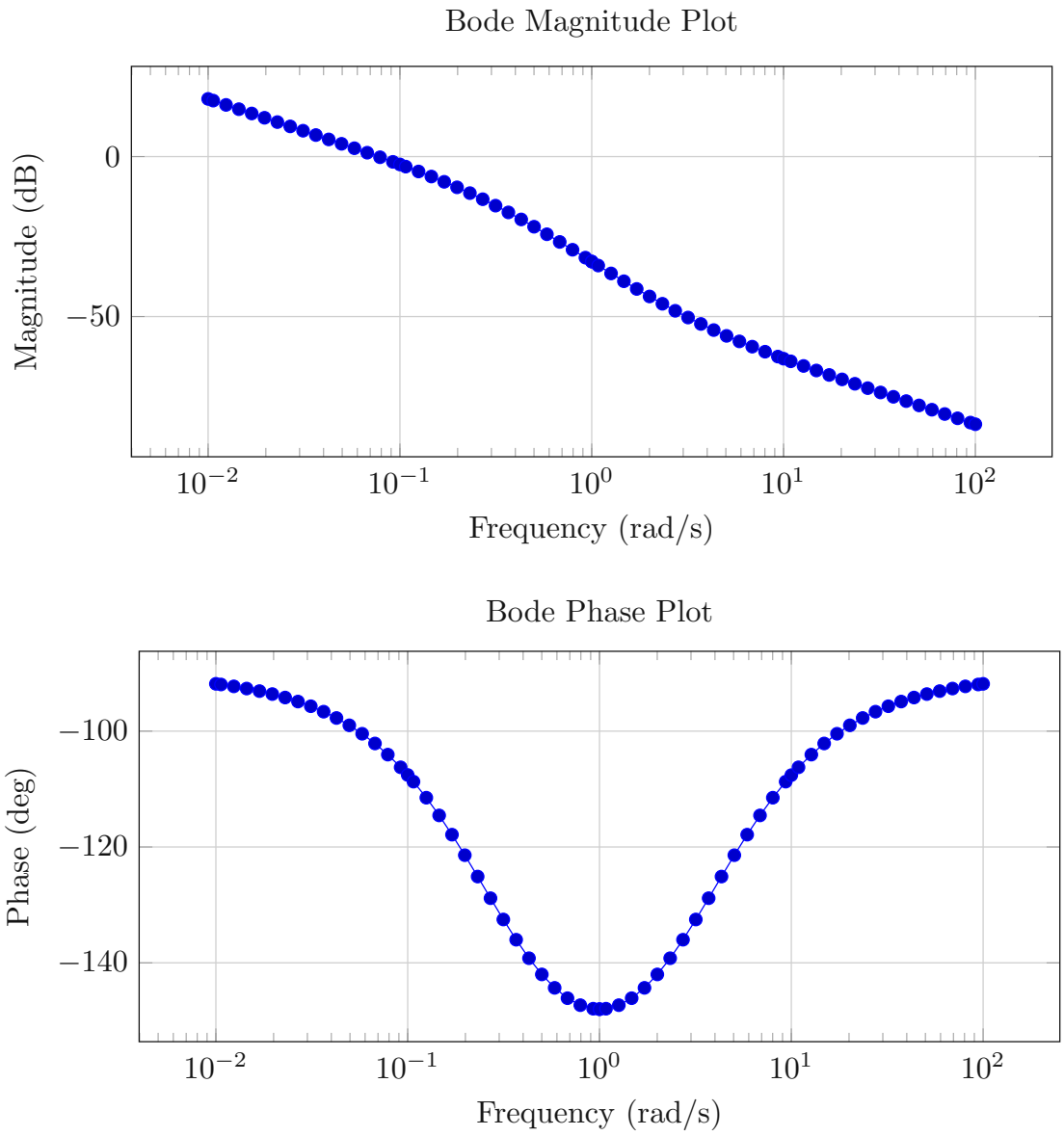

Figure 6.10: Bode plot of the open-loop transfer function $C_{PI}(s)\,G_V(s)$ of the vortex.

The step response of the closed-loop system is shown in Figure 6.11. It takes more than 30 seconds for the vortex to reach the desired velocity. Additionally, there is no overshoot. Besides, the velocity sensor has a bandwidth that increases with the velocity of the vortex. Hence, the sample time of the sensor depends on the velocity. So, with very high controller gains there is overshoot and the system oscillates, as the velocity estimation is highly delayed.

Compared to the open-loop response in Figure 6.8, the vortex requires more time to reach a certain velocity. With closed-loop control the steady-state control error is smaller than with the open-loop approach.

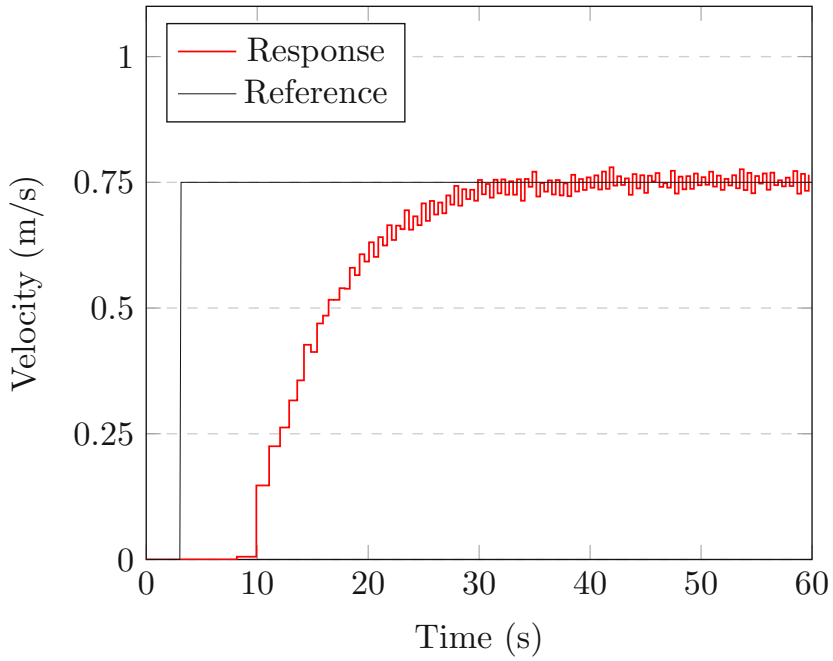

Figure 6.11: Measured closed-loop step response of the vortex for the velocity at the outermost paddle.

Additionally, the stability of the closed-loop is analyzed. The transfer function of the closed-loop is

$$T_{r_2,y_2}(s) = \frac{C_{PI}(s)\,G_V(s)}{1 + C_{PI}(s)\,G_V(s)} = \frac{0.02286s + 0.07981}{3.484s^2 + 1.023s + 0.07981}. \tag{6.24}$$

One pole is at

$$s = -0.1468 + 0.0369\mathrm{I} \tag{6.25}$$

and the second at

$$s = -0.1468 - 0.0369\mathrm{I}. \tag{6.26}$$

All poles have negative real parts and therefore, are in the left-half of the s-plane. This means the closed-loop is also BIBO stable. Testing verifies that the closed-loop is stable during normal operation.

7 Summary and Outlook

This chapter concludes the thesis and discusses the results as well as some limitations. It finishes with an outlook section on further possibilities based on the existing setup.

7.1 Summary

A watertight test stand was designed and built that can create a water vortex in a closed cylinder. The outlet and inlet are both tangential to the cylindrical wall so that the radial velocity component is minimized. Hence the vortex is mainly characterized by a tangential component.
Most parts were printed with conventional 3D printers and the remaining items were purchased.
With a specifically designed and manufactured velocity sensor, the vortex velocity can be measured. In total, four light barriers that make up this sensor measure the velocity of the vortex at four different points. This is achieved with four rotating paddles that cause intensity drops when passing through the light barriers. Despite static friction in the bearings and the large number of arms carrying the paddles the measurement is sufficiently reliable.
CFD simulation results were used to calibrate the measured velocities at the four points along the radius.
Additionally, a model for the tangential velocity of the vortex was derived based on the Navier-Stokes equations at 13 L/min. Additionally, a boundary condition was defined for the velocity with respect to the flow rate at position of the outermost paddle. As this simplified derived model was not in agreement with the measurements, correction factors were introduced to fit the model to the measurements. Validation was carried out with the remaining data, which show that the fitted model is sufficiently accurate for describing the velocity of the vortex.
Likewise, a model for the pressure as a function of the radius, vertical position in the z-direction and flow rate was also derived. The local pressure depends on the velocity of the vortex. Moreover, the models and the data show that the velocity and pressure increase nonlinearly with the radius.
Furthermore, cascade control was implemented for the entire system. The inner feedback loop uses the pump and a hall sensor for measuring its flow rate. This controller only consists of an integral gain. The outer loop consists of the vortex and a velocity sensor, which is responsible for feedback. The controller consists of a proportional and integral gain.
The measured data also reveals that the velocity of the vortex is approximately proportional to the flow rate of the pump. This is true for all four measurement points.

The first main objective mentioned in Section 1.3 was achieved with a working test stand. A cascade controller for the vortex was successfully implemented. The derived mathematical model was additionally fitted to the calibrated measurements and accurately describes the tangential velocity of the vortex.

7.2 Outlook

The fact that PLA is suitable for such setups shows the potential of FDM even for such applications. This implies that more sophisticated test stands of this type can be mastered with this manufacturing technique. Even standard printers can be used for this.
The paddles could be printed with a less dense material than PLA. This would further improve the design and sensitivity. Also, the transimpedance amplifier circuit could be optimized to prevent the operational amplifier from saturating. Additionally, the sensor could be modified or the paddles optically tracked by a camera to significantly increase the sensor bandwidth.
With a faster sensor, the controller could be designed with a higher bandwidth. Besides, the designed controller could be combined with feedforward control, which takes into account the derived model.
Likewise, optical methods such as PIV could be implemented to derive a more precise model. PIV could replace the submerged paddles, which interfere with the flow and may be slowed down by friction in the bearings.
Additionally, a dynamic model of the vortex could be derived and used for designing the controller.
Last but not least, the cylinder could be made even taller to reduce the effect of the boundary layer on the vortex.

Bibliography

[1] S. Dhakal *et al.*, "Comparison of cylindrical and conical basins with optimum position of runner: Gravitational water vortex power plant," *Renewable and Sustainable Energy Reviews*, vol. 48, pp. 662–669, 2015.

[2] D. S. Edirisinghe *et al.*, "Numerical and experimental investigation on water vortex power plant to recover the energy from industrial wastewater," *Renewable Energy*, vol. 204, pp. 617–634, 2023.

[3] A. A. Ismaeel, H. H. Al-Kayiem, A. T. Baheta, and M. A. Aurybi, "Review and comparative analysis of vortex generation systems for sustainable electric power production," *IET Renewable Power Generation*, vol. 11, no. 13, pp. 1613–1624, 2017.

[4] H. Jing, H. Xiang, and J. Wang, "Modified vortex-induced vibration piezoelectric energy harvester for capturing wind energy from trains moving in tunnels," *Sensors and Actuators A: Physical*, vol. 382, p. 116 136, 2025.

[5] J. M. K. P. S. Srinivas A. Singh and A. K. Jana, "A water-model experimental study of vortex characteristics due to nozzle clogging in slab caster mould," *Ironmaking & Steelmaking*, vol. 44, no. 7, pp. 473–485, 2017. eprint: `https://doi.org/10.1080/03019233.2016.1215948`.

[6] I. Mutabazi, N. Abcha, O. Crumeyrolle, and A. Ezersky, "Application of the particle image velocimetry to the Couette-Taylor flow," G. Cavazzini, Ed., 2012. eprint: `https://doi.org/10.5772/45644`.

[7] M. Raffel, C. E. Willert, F. Scarano, C. J. Kähler, S. T. Wereley, and J. Kompenhans, *Particle image velocimetry : a practical guide*, Third edition. Cham: Springer, 2018.

[8] B. Li and F. Tsukihashi, "Vortexing flow patterns in a water model of slab continuous casting mold," *Isij International - ISIJ INT*, vol. 45, pp. 30–36, Jan. 2005.

[9] Q. Liu, B. An, M. Nohmi, M. Obuchi, and K. Taira, "Active flow control of a pump-induced wall-normal vortex with steady blowing," *Journal of Fluids Engineering*, vol. 142, p. 081 202, Apr. 2020. eprint: `https://doi.org/10.1115/1.4046692`.

[10] A. G. Stephenson, M. G. Faram, and R. Y. G. Andoh, "Vortex flow controls: State of the art review and application (from the catchbasin to the dam)," in *Novatech 2010 - 7ème Confèrence internationale sur les techniques et stratègies durables pour la gestion des eaux urbaines par temps de pluie / 7th International Conference on Sustainable Techniques and Strategies for Urban Water Management*, Lyon, 2010, pp. 1–10.

[11] S. Vemulapalli and S. K. Venkata, "Parametric analysis of orifice plates on measurement of flow: A review," *Ain Shams Engineering Journal*, vol. 13, no. 3, p. 101 639, 2022. eprint: `https://doi.org/10.1016/j.asej.2021.11.008`.

[12] R. Korpus and S. Liapis, "Active and passive control of spar vortex-induced motions," *Journal of Offshore Mechanics and Arctic Engineering-transactions of The Asme - J OFFSHORE MECH ARCTIC ENG*, vol. 129, Nov. 2007.

[13] J. Chen, J. Wu, and J. Chen, "Vortex induced vibration control of a cactus-shaped cylinder with porous spines," *Ocean Engineering*, vol. 313, p. 119 401, 2024. eprint: https://doi.org/10.1016/j.oceaneng.2024.119401.

[14] J. Song, J. Du, and X. Gao, "Applying PID control to 2-DOF vortex induced vibration of a cylinder," *Ocean Engineering*, vol. 300, p. 117 295, 2024. eprint: https://doi.org/10.1016/j.oceaneng.2024.117295.

[15] M. Milovanovic and O. Morten Aamo, "Attenuation of vortex shedding by model-based output feedback control," *IEEE Transactions on Control Systems Technology*, vol. 21, no. 3, pp. 617–625, 2013.

[16] M. D. Gunzburger and H. C. Lee, "Feedback control of Karman vortex shedding," *Journal of Applied Mechanics*, vol. 63, no. 3, pp. 828–835, Sep. 1996. eprint: https://doi.org/10.1115/1.2823369.

[17] H. Egitmen, Ä. Diker, and G. M. Ozkan, "A novel approach to the control of vortex shedding downstream of a circular cylinder by control rod," *Ocean Engineering*, vol. 317, p. 120 010, 2025. eprint: https://doi.org/10.1016/j.oceaneng.2024.120010.

[18] Q. u. Ain, R. Mahmood, J. Awrejcewicz, I. Siddique, A. H. Majeed, and W. Pawłowski, "Effectiveness of splitter plate to control fluid forces on a circular obstacle in a transient flow: FEM computations," *Scientific Reports*, vol. 12, no. 1, p. 13 602, 2022. eprint: https://doi.org/10.1038/s41598-022-17947-w.

[19] W. Bohl and W. Elmendorf, *Technische Strömungslehre: Stoffeigenschaften von Flüssigkeiten und Gasen, Hydrostatik, Aerostatik, Inkompressible Strömungen, Kompressible Strömungen, Strömungsmesstechnik* (Kamprath-Reihe), 15th ed. Vogel, 2014.

[20] I. E. Idelchik, *Handbook of hydraulic resistance : Coefficients of local resistance and of friction*. Jerusalem: Israel Program for Scientific Translations, 1966.

[21] R. K. Sampson, "Apparatus for connecting an elastic hose to a system with an anti-hose rotation shaped hollow body," Utility Patent US5076615, 1991.

[22] D. Troy, J. Remington, and P. Beringer, *Remington: the science and practice of pharmacy* (REMINGTON THE SCIENCE AND PRACTICE OF PHARMACY). Lippincott Williams & Wilkins, 2006.

[23] USDOE, "DOE fundamentals handbook: Thermodynamics, heat transfer, and fluid flow, volume 3," USDOE, Washington, DC (United States), Tech. Rep., Jun. 1992.

[24] MARCO S.P.A., *SELF-PRIMING ELECTRIC PUMP FOR TRANSFERRING VARIOUS LIQUIDS: INSTRUCTIONS FOR USE: 164 002 12 - UP3-P 12V 164 002 13 - UP3-P 24V*, Brescia, Italy, 2021.

[25] H. Dubbel and W. Beitz, *Taschenbuch für den Maschinenbau*, 19th ed. Berlin: Springer, 1997.

[26] K.-H. Grote and H. Hefazi, Eds., *Springer handbook of mechanical engineering*, 2nd ed. Cham: Springer, 2021.

[27] Kunststoffplattenonline GmbH, *Technisches Datenblatt: PMMA GS: Acrylglas GS Platte*, Duisburg, 2025.

[28] H. Wittel, D. Muhs, D. Jannasch, and J. Voßiek, *Roloff/Matek Maschinenelemente: Normung, Berechnung, Gestaltung*, 20th ed. Springer, 2011.

[29] H. Schlichting and K. Gersten, *Boundary-layer theory*, 9th ed. 2017. Berlin, Heidelberg: Springer, 2016.

[30] R. Sinnott, *Chemical engineering design: chemical engineering, Volume 6* (Chemical Engineering Series). Butterworth-Heinemann, 2005.

[31] B. Eck, *Technische Strömungslehre : Hydrostatik, Bewegungslehre, Turbulenz, Diffusorproblem, Reibung, Ablösung, Kavitation, Körper in strömenden Medien, Strömung um Schaufeln und Profile, Gasdynamik, Messungen, Versuche*, 7th ed. Berlin: Springer, 1966.

[32] E. Crespo del Arco, E. Serre, P. Bontoux, and B. Launder, "Stability, transition and turbulence in rotating cavities," in *Advances in Fluid Mechanics*, vol. 41, Jan. 2004, pp. 141–195.

[33] K. M. P. van Eeten, J. van der Schaaf, J. C. Schouten, and G. J. F. van Heijst, "Boundary layer development in the flow field between a rotating and a stationary disk," *Physics of fluids (1994)*, vol. 24, no. 3, pp. 033 601–033601-18, 2012.

[34] A. Riedl, *Handbuch Dichtungspraxis*, ger, 4. Auflage. Essen: Vulkan Verlag, 2017.

[35] H. K. Dave and J. P. Davim, *Fused deposition modeling based 3D printing*. Springer, 2021.

[36] B. Rădulescu *et al.*, "Thermal expansion of plastics used for 3d printing," *Polymers*, vol. 14, no. 15, 2022.

[37] R. Schmidt, G. Schitter, A. Rankers, and J. van Eijk, *The design of high performance mechatronics - 2nd revised edition: high-tech functionality by multidisciplinary system integration*. IOS Press, 2014.

[38] Texas Instruments Incorporated, "Analog engineer's circuit: transimpedance amplifier circuit," Texas Instruments Incorporated, Dallas, Tech. Rep., 2023.

[39] OSRAM Opto Semiconductors GmbH, *SFH 203: Radial T1 3/4: Silicon PIN Photodiode*, Regensburg, 2018.

[40] Texas Instruments Incorporated, *TL03x, TL03xA ENHANCED-JFET LOW-POWER LOW-OFFSET OPERATIONAL AMPLIFIERS*, Texas Instruments Incorporated, 2001.

[41] Texas Instruments Incorporated, *TL07xx low-noise JFET-input operational amplifiers*, Dallas, 2024.

[42] P. Horowitz and W. Hill, *The art of electronics*, 3rd ed. New York: Cambridge University Press, 2016.

[43] Maxim Integrated, *MAX1044/ICL7660: switched-capacitor voltage converters*, San Jose, 1994.

[44] Gems Sensors Inc., *FT-110 Series - turboflow economical flow-rate sensors*, Gems Sensors Inc., 2019.

[45] dSPACE GmbH, *Hardware installation and configuration*, dSPACE GmbH, Paderborn, 2021.

[46] Gems Sensors Inc., *Frequency output: .26-6.6 GPM (1-25LPM) FT-110 Flow Range*, Gems Sensors Inc., 2023.

[47] maxon motor ag, *ESCON 50/5:Servo Controller:P/N 409510:Hardware Reference*, maxon motor ag, 2018.

[48] H. Versteeg and W. Malalasekera, *An introduction to computational fluid dynamics: the finite volume method*. Pearson Education Limited, 2007.

[49] S. Pope, *Turbulent flows*. Cambridge University Press, 2000.

[50] B. Launder and D. Spalding, "The numerical computation of turbulent flows," *Computer Methods in Applied Mechanics and Engineering*, vol. 3, no. 2, pp. 269–289, 1974.

[51] S. Murphy, *The art of polynomial interpolation*, 1st ed. The Pennsylvania State University, 2022.

[52] F. White, *Viscous fluid flow* (McGraw-Hill series in mechanical engineering). McGraw-Hill, 1991.

[53] S. J. Farlow, *Partial differential equations for scientists and engineers*. Dover Publications, 1993.

[54] F. W. J. Olver, D. W. Lozier, R. F. Boisvert, and C. W. Clark, Eds., *NIST handbook of mathematical functions*. New York: Cambridge University Press, 2010.

[55] J. Stewart, *Calculus: Early transcendentals*. Belmont: Brooks/Cole, Cengage Learning, 2012.

[56] A. Bjorck, *Numerical methods for least squares problems* (Other Titles in Applied Mathematics). Society for Industrial and Applied Mathematics, 1996.

[57] W. Bolton, "Chapter 13 - control systems," in *Instrumentation and control systems*, W. Bolton, Ed., 3rd ed., Newnes, 2021, pp. 297–328.

[58] S. S. Niu and D. Xiao, *Process control: Engineering analyses and best practices* (Advances in Industrial Control). Cham: Springer, 2022.

[59] A. Ghosh, *Introduction to linear and digital control systems*. PHI Learning, 2007.

[60] W. Siebert, *Circuits, signals, and systems*. McGraw-Hill, 1986.

Eidesstattliche Erklärung

Hiermit erkläre ich, dass die vorliegende Arbeit gemäß dem Code of Conduct – Regeln zur Sicherung guter wissenschaftlicher Praxis (in der aktuellen Fassung des jeweiligen Mitteilungsblattes der TU Wien), insbesondere ohne unzulässige Hilfe Dritter und ohne Benutzung anderer als der angegebenen Hilfsmittel, angefertigt wurde. Die aus anderen Quellen direkt oder indirekt übernommenen Daten und Konzepte sind unter Angabe der Quelle gekennzeichnet. Die Arbeit wurde bisher weder im In– noch im Ausland in gleicher oder in ähnlicher Form in anderen Prüfungsverfahren vorgelegt.

Wien, Juni 2025

Ivan Wuketich